Universitat Autònoma de Barcelona

Chemomagnetooptically controlled nanomotors for (bio)contaminant removal in water

Kuan Zhang

ADVERTIMENT. L'accés als continguts d'aquesta tesi doctoral i la seva utilització ha de respectar els drets de la persona autora. Pot ser utilitzada per a consulta o estudi personal, així com en activitats o materials d'investigació i docència en els termes establerts a l'art. 32 del Text Refós de la Llei de Propietat Intel·lectual (RDL 1/1996). Per altres utilitzacions es requereix l'autorització prèvia i expressa de la persona autora. En qualsevol cas, en la utilització dels seus continguts caldrà indicar de forma clara el nom i cognoms de la persona autora i el títol de la tesi doctoral. No s'autoritza la seva reproducció o altres formes d'explotació efectuades amb finalitats de lucre ni la seva comunicació pública des d'un lloc aliè al servei TDX. Tampoc s'autoritza la presentació del seu contingut en una finestra o marc aliè a TDX (framing). Aquesta reserva de drets afecta tant als continguts de la tesi com als seus resums i índexs.

ADVERTENCIA. El acceso a los contenidos de esta tesis doctoral y su utilización debe respetar los derechos de la persona autora. Puede ser utilizada para consulta o estudio personal, así como en actividades o materiales de investigación y docencia en los términos establecidos en el art. 32 del Texto Refundido de la Ley de Propiedad Intelectual (RDL 1/1996). Para otros usos se requiere la autorización previa y expresa de la persona autora. En cualquier caso, en la utilización de sus contenidos se deberá indicar de forma clara el nombre y apellidos de la persona autora y el título de la tesis doctoral. No se autoriza su reproducción u otras formas de explotación efectuadas con fines lucrativos ni su comunicación pública desde un sitio ajeno al servicio TDR. Tampoco se autoriza la presentación de su contenido en una ventana o marco ajeno a TDR (framing). Esta reserva de derechos afecta tanto al contenido de la tesis como a sus resúmenes e índices.

WARNING. The access to the contents of this doctoral thesis and its use must respect the rights of the author. It can be used for reference or private study, as well as research and learning activities or materials in the terms established by the 32nd article of the Spanish Consolidated Copyright Act (RDL 1/1996). Express and previous authorization of the author is required for any other uses. In any case, when using its content, full name of the author and title of the thesis must be clearly indicated. Reproduction or other forms of for profit use or public communication from outside TDX service is not allowed. Presentation of its content in a window or frame external to TDX (framing) is not authorized either. These rights affect both the content of the thesis and its abstracts and indexes.

Universitat Autònoma de Barcelona

Chemomagnetooptically controlled nanomotors for (bio)contaminant removal in water

Kuan Zhang

Doctoral Thesis

Doctoral Program in Materials Science

Directors: Dr. Maria Jose Esplandiu Egido and Dr. Borja Sepúlveda Martínez

Tutor: Iluminada Gallardo García

Department of Chemistry

Faculty of Science

2019

Memòria presentada per aspirar al Grau de Doctor per

Kuan Zhang

Vist i plau:

Co-Director Dr. María José Esplandiu Egido Co-Director Dr. Borja Sepúlveda Martínez

Ttutor Dr. Iluminada Gallardo García

Bellaterra, 18 March 2019

CONTENTS

ACKNOWLEDGEMENTS

For my four years at ICN2, it is my great honor to work with a group of people who are not only extraordinarily talented, but also generous with their support and very enthusiastic about life.

First of all, I would like to express my great gratitude to my thesis supervisors, Dr. Maria Jose Esplandiu Egido and Dr. Borja Sepúlveda Martínez, for their guidance and encouragement throughout the work.

I am deeply grateful to work in Magnetic Nanostructures group and Force probe microscopy and surface nanoengineering group led by Dr. Josep Nogués Sanmiquel and Dr. Jordi Fraxedas Calduch respectively. I would like to thank Dr. Jordi Fraxedas Calduch for helping me with XPS experiments at ICN2 and ALBA synchrotron.

The financial support from Severo Ochoa fellowship is gratefully acknowledged as well as the support of the Spanish Ministry of Economy and Competitiveness MINECO (under Contract No. MAT2015-68307-P and M-ERA-NET Project PCIN-2016-093).

In the end, I am indebted to my parents for their endless support, understanding, and encouragement.

ABSTRACT

The goal of the thesis is to develop photoelectrochemically activated silicon/metal autonomous nanomotors, to explore and understand the mechanisms involved in the propulsion process, and to analyse their potential application in (bio) contaminant removal in water through their in-situ generation of reactive oxygen species. We have basically focused on Si/Pt nanomotors which can self-propel from the photochemical decomposition of H_2O_2 triggered by white light illumination and with also capabilities to be activated by NIR light.

We have developed a facile method to fabricate large scale of silicon nanostructures as core of the nanomotors using colloidal lithography in conjunction with metal-assisted etching. Silicon nanostructures with different dimensions, surface morphologies, and porosities were accomplished.

We have evaluated the photochemical actuation of Si/Pt nanomotors with different roughness factors at the Pt catalyst. Si/Pt nanostructures with low metal roughness factor hardly moved but Si/Pt nanostructures with high metal roughness factor exhibited a substantial directional motion but insensitive to light modulation. Evaluation of the Si/Pt nanomotor performance for degradation of benzene based pollutants in water provided hints of two competing chemical pathways in H_2O_2 decomposition, which finally dictated the dominant propulsion mechanism. Such finding was supported by comparing the nanomotor performance with the one of their immobilized counterparts Si/Pt pumps with different Pt roughness factors. It was demonstrated that there are two competing propulsion mechanisms at the Pt/Si motors under light illumination depending on the H_2O_2 decomposition pathway. One is an electro-osmotic process which stemmed from a separated photoactivation redox reaction mediated by Si as anode and smooth Pt as cathode. The other is a diffusio-osmotic process and not light responsive and is triggered by the redox decomposition of H_2O_2 exclusively at the rough Pt surface. Therefore we could show that the actuation mechanism of the Pt/Si motors can be switched from light-controlled electrokinetics to light-insensitive diffusio-osmosis by only increasing the metal surface roughness. Moreover the increased roughness in Pt greatly decreased the motor generation of reactive oxygen species, which are expected to take place from a photochemical separated redox reaction at anode and cathode, and hence decreasing the motor capability as pollutant degradation agent.

In the final part of the thesis work, we have successfully achieved a photochemical-controlled silicon/Au microdiode with p-n heterojunctions which has aided to settle the criteria to build up optimized light sensitive silicon based micro/nanomotors. The n-p junction helps to maximize separated photoredox reactions between Si and noble metal by the built-in electric field which favours the hole/electron separation. Moreover, it was concluded that the perimeter of the interface should be large enough and the surface of noble metal should exhibit low roughness factors.

Finally we have also found a promising nanomotor based on Si/zero-valent iron (ZVI) for relevant organic degradation performance under visible light illumination through the generation of reactive oxygen species. This nanosystem has provided an important contribution of the photocatalytic effect for the overall generation of ROS apart from the contribution provided by the iron Fenton reaction.

This thesis has accomplished a relevant progress in understanding silicon based photocatalytic micro-/nanomotors and it has shown that these systems hold great potential for future practical applications. However, much work is still needed to continue improving and optimizing the engine, which guarantees the continuation of this line of research.

1 INTRODUCTION

Tool use can be dated back to the Stone Age and it plays an essential role in human being evolution. Motors or machines convert energy into movement, which have been fundamental tools for the development of society. Inspired by the models of nature, considerable efforts have been devoted to developing machines that can imitate the function of these amazing natural systems. One of the early attempts of biomimicry could be the study of birds to enable human flight.[1] In 1959, Richard Feynman delivered a famous talk entitled "There's Plenty of Room at the Bottom" at the American Physical Society, which wielded the foundations that later on would kick off the new era of nanotechnology and the use of the cellular machinery as bionspiration for the development of multitasking nanosystems.[2] The shrinking of motors towards micro/nanoscale has drawn more and more attention of academia in the narrative of nanotechnology, making it possible to fabricate artificial microorganisms for various potential applications. Such tiny machines can help in carrying out tasks like targeted drug delivery in the human body, non-invasive operations in cells, bio sensing and bio imaging, and environmental monitoring and contaminant destruction.[3,4]

1.1 SELF-PROPULSION AT THE MICRO-/NANOSCALE: CHALLENGES

In the same way the impressive molecular machinery operates in living organisms, micro/nanomachines are expected to be able to self-propel and carry out autonomous work “a la carte”. However, several essential challenges should be tackled in the development of micro/nanomachines when it is going from macro to micro and ultimately to nanoscale.

Firstly, as size decreases, the ratio of surface area to volume increases, implying that volume-dependent forces (such as inertia), which dominate at longer length scales, become less relevant as objects are scaled down. Artificial micro/nano-objects have to move in low Reynolds number environments.[5] The Reynolds number (Re) , which is a dimensionless parameter defined as the ratio of inertial to viscous forces, quantifies the relative importance of these two types of forces for given flow conditions and can be also used as a guide to predict laminar or turbulent flows.[6]

$$Re = \frac{\text{inertial force}}{\text{viscous force}} = \frac{\rho v L}{\mu}$$

where ρ is density, v is the particle velocity, L is the characteristic length of the object and μ is the dynamic viscosity of the medium. A swimming person has a Reynolds number of 10^4 whereas bacteria have a Reynolds number of 10^{-4}.[5] For most of the micro-/nanomotors, the Reynolds number is on the same order as that of moving bacteria. The low Reynolds number implies that viscous forces dominate and within this regime only irreversible motion can lead to net propulsion, requiring also breaking the time-reversal symmetry, for example, by introducing an asymmetry in the swimmer design (either in the shape, composition, surface activity etc.)[5,7] Secondly, at low Re, the objects are more subjected to Brownian motion (passive diffusion) which causes the object to rotate and change its orientation randomly.[8] For directed motion under low Re a continuous input of energy is required. The precise navigation of nanoscale objects is extremely challenging because of the combination of Brownian motion and low Reynolds numbers.[9] Finally, the energy harvesting and transfer to drive the motor at nanoscale is more troublesome.[10]

Therefore, design principles used in the macroscale may not be applicable in the nanoscale. Since at small scales the surface effects (rather than the volume ones) are important, one can exploit surface-dependent forces to induce motion. For example, one way to trigger surface body forces is through the own generation of physical-chemical gradients at the motor interface. In this context, nature is a source of inspiration for artificial machines. The conversion of chemical energy into directed motion is a key point behind the highly efficient performance of biomolecular machinery before mentioned.

The chart in figure 1.1 illustrates the main propulsion mechanisms for micro-/nanomotors either in a swimmer configuration (free suspending in the fluid) or immobilized on a surface (pumps). The prefix “self” indicates that the propulsion mechanism emerges from physicochemical gradients generated by the own motor particles.

These mechanisms and corresponding representatives will be discussed in the following section.

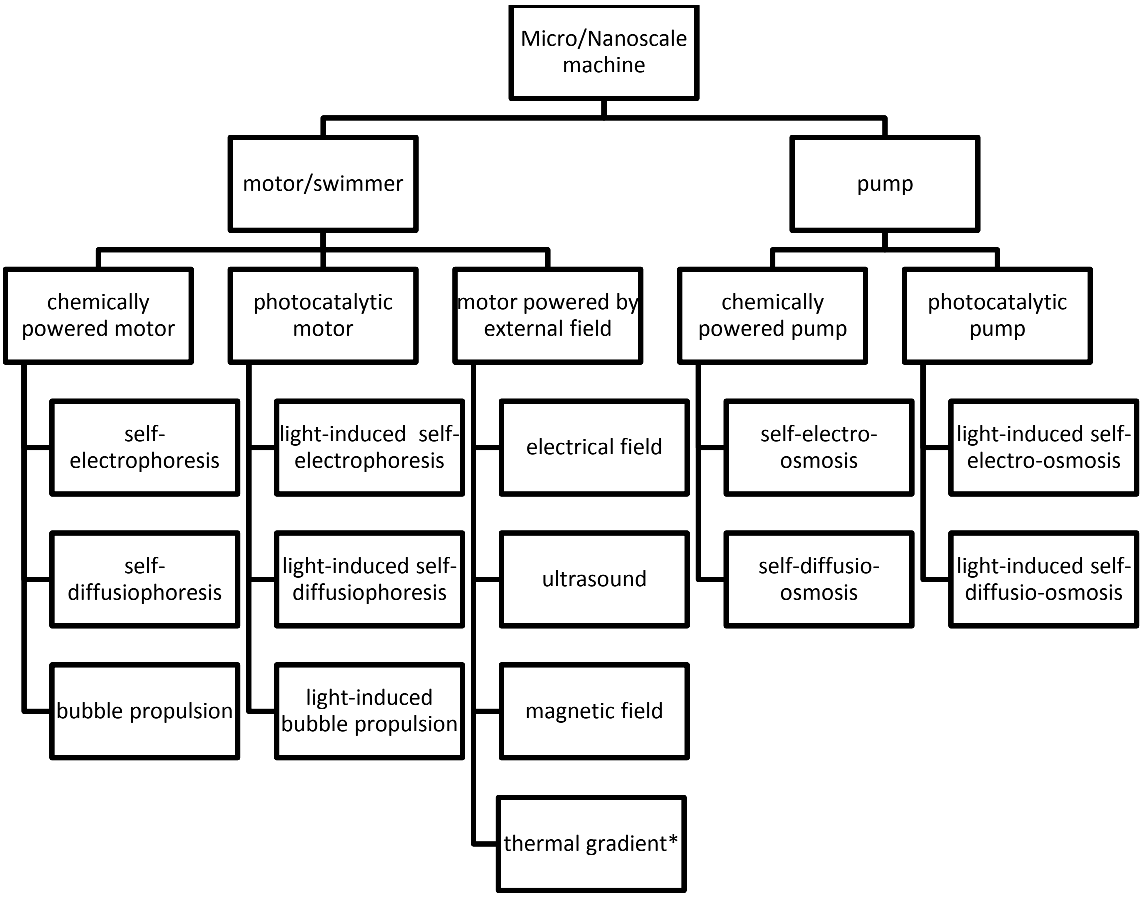

Figure 1.1 the schematic diagram showing main propulsion mechanisms employed to power micro/nanoscale machines (thermal gradient*: the temperature gradient can be externally produced or self-produced. Self-thermophoresis can be produced by motor light illumination or by applying magnetic fields. Similarly pumps also can be activated by thermos-osmosis via light or magnetic field.)

1.2 CHEMICAL FUEL BASED PROPULSION OF MICRO-/NANOMOTORS AND PUMPS

Micro-/nanomotors driven by chemical gradients have been the most widely studied ones during the last decade.[11] An impressive work has been developed since the development of the first self-propelled machines by chemical gradient, which was reported by Paxton et al.[12] and Fournier-Bidoz et al.[13]

As mentioned before these self-propelled machines can be either in a swimmer (free suspended in the fluid) or pump configuration (immobilized on a surface), being pumps very useful platforms for better evaluating and understanding the chemically propulsion mechanisms.

1.2.1 SWIMMERS

There are mainly three self-propulsion mechanisms driven by chemical reactions in the case of the micro/nano-swimmers. They are self-electrophoresis, self-diffusiophoresis (neutral or ionic) and bubble propulsion respectively. Such self-propulsion mechanisms can operate in the machines depending on their composition, shape, size, fuel nature and concentration.

1.2.1.1 SELF-ELECTROPHORESIS

The self-electrophoresis refers to the motors propelled by pure electrophoresis, which is driven by a self-generated ionic current which builds up an electric field. Such ionic current can be produced on bimetallic or metal/semiconductor motors when chemical reactions such as half redox reactions are induced separately at different places of the motor. The production and consumption of ionic species at different motor locations induce an electric field which triggers the fluid flow at the motor interface.

In electrophoresis, charged particles migrate in an electric field (**E**), and their velocity (**U**) can be well described by the Smoluchowski equation for particles with thin double layers.[14,15]

$$\boldsymbol{U} = \frac{\zeta_m \varepsilon}{\mu} \boldsymbol{E}$$

where ζ_m is the zeta potential of the motor surface which is related to the surface charge, ε is the permittivity of the medium (water), and μ is the dynamic viscosity of water.

For instance in the case of the pioneering bimetallic Au/Pt motors immersed in H_2O_2, an electric field is generated from H_2O_2 oxidation and reduction at Pt and Au, respectively.[12] The redox reaction produces protons at the anode that are consumed at the cathode, building up a proton gradient that induces a proton current. The resulting ion flux generates an electric field toward the Au end which drags the fluid in the same direction, thereby moving the rod in the opposite direction. Figure 1.2 illustrates the self-electrophoresis process for Au/Pt motors in H_2O_2 aqueous solution.

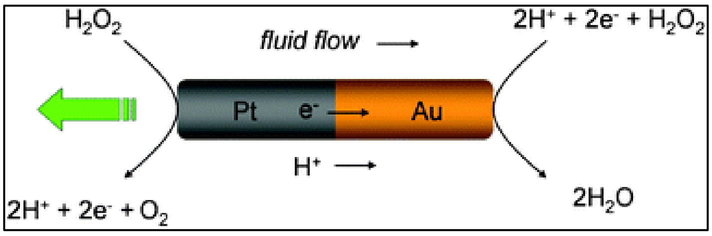

Figure 1.2 Schematic illustrating self-electrophoresis. Hydrogen peroxide is oxidized at the Pt segment to generate protons in solution and electrons in the rod. The protons and electrons are then consumed with the reduction of hydrogen peroxide at the gold end.[16]

Table 1.1 lists typical swimmers based on self-electrophoresis. The propulsion speed is taken at normalized body length per second (bdl/s). It is worth noting that introducing catalysts such as Rh, Ru and Pd can considerably increase the efficiency of the motors. Moreover, when the motor size is scaled down from micrometer to nanometer (e.g. Janus nanosphere), the velocity is increased several orders of magnitude which is in agreement with theoretical predictions (see in Ref. 22). Although the translational velocity can be greatly enhanced in such small scales, it is also true that their dynamics is strongly influenced by fast Brownian rotations. Consequently, very small motors show bursts of linear ballistic motion combined with very fast rotations which impose an upper limit on the ballistic swimming length of the nanomotors.

Table 1.1 summary of swimmers based on self-electrophoresis

Geometry	Material composition	Fuels/solvent	Propulsion speed	Reference
Rod	Pt/Au	2–3% H_2O_2	4 bdl/s	17
Rod	Pt(Carbon nanotube)/Au	5% H_2O_2	20 bdl/s	18
Rod	Pt/Cu	0.2 mM Br_2	10 bdl/s	19
Rod	Rh/Au	5% H_2O_2	12 bdl/s	20
	Pt/Au		10 bdl/s	
	Pd/Au		8 bdl/s	
	Pt/Ru		15 bdl/s	
	Au/Ru		12 bdl/s	
	Rh/Pt		9 bdl/s	
	Rh/Pd		8 bdl/s	
	Pt/Pd		7 bdl/s	
	Ni/Au		2.5 bdl/s	
	Ag/Au		3 bdl/s	

	Au/Co		3.5 bdl/s	
Janus microparticle	fluorescent polystyrene/Au/Pt	1–4 % H_2O_2	8 bdl/s	21
Janus nanosphere	Au/Pt	1-5% H_2O_2	$2x10^4$ bdl/s	22

1.2.1.2 DIFFUSIOPHORESIS

Diffusiophoresis is a phenomenon in which the motion of particles is driven by a concentration gradient of solutes. Chemical reactions taking place at surfaces consume reactants and generate products, resulting in concentration gradients that in turn power the motion of micro-/nanomotors. Generally speaking, there are two types of self-diffusiophoresis, one is non-ionic (neutral) and the other is ionic.

In the case of neutral diffusiophoresis, the spontaneous motion of dispersed particles in a fluid is induced by a diffusion gradient of a non-ionic solute. The motion direction and speed depend on the interaction of the liquid with the motor surface. In the simplest case of excluded volume interactions, a fluid flow directed toward higher solute concentration is induced, leading to motor motion in the opposite direction.

Ionic diffusiophoresis usually refers to the movement of a particle by the electric field and pressure field set up by the differential diffusion of specific cations and anions in the fluid. In this case, the chemomechanical actuation depends on both chemophoretic and electrophoretic contributions. For a concentration gradient ∇c of monovalent salt, the velocity **U** of a charged particle near the charged surface of the motor is governed by the following equation:[23]

$$U = \overbrace{\frac{\nabla c}{c_0}\left[\left(\frac{D^+ - D^-}{D^+ + D^-}\right)\left(\frac{k_B T}{e}\right)\frac{\varepsilon(\zeta_p)}{\eta}\right]}^{\textbf{Electrophoretic term}} + \overbrace{\frac{\nabla c}{c_0}\left[\left(\frac{2\varepsilon k_B^2 T^2}{\eta e^2}\right)\left\{\ln\left(1 - \gamma_p^2\right)\right\}\right]}^{\textbf{Chemophoretic term}}$$

where $D^+$and D^- are the diffusion coefficients of the cation and anion respectively, c_0 is the bulk concentration of ions, e is the charge of an electron, k_B is the Boltzmann constant, T is the absolute temperature, ε is the dielectric permittivity of the solution, η is the viscosity, ζ_p is the zeta potential of the particle, and $\gamma_p = \tanh e\zeta_p/4k_B T$.

The electrophoretic term represents the motion of the particle due to an electric field which arises as a consequence of the different ion diffusion coefficients ($D^+$and D^-). In addition, cations and anions interact with the double layer of the charged particle differently, leading to a pressure unbalance that induces a liquid flow toward the lower concentration. This effect is represented by the chemophoretic term in the equation above. In most cases, chemophoretic effects are negligible and the directions of diffusiophoretic flows are dominated by the electrophoretic effect, unless the diffusivities of the cations and anions are very similar. Figure 1.3 shows a generic scheme of electrolyte diffusiophoresis, where a charged particle is driven by a concentration gradient of ionic species.[24]

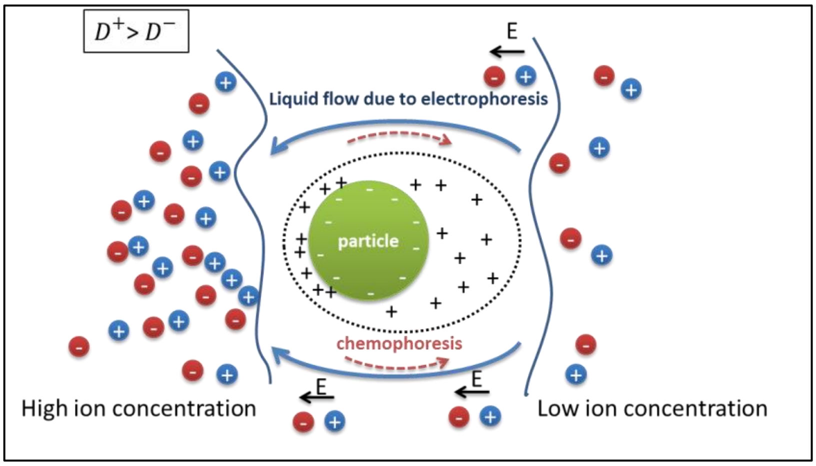

Figure 1.3 Scheme of electrolyte diffusiophoresis of a negatively charged particle immersed in an ionic concentration gradient.[24] In this illustration it was considered that the cation has a higher diffusion coefficient than the anion one inducing an spontaneous electric field in the solution. The double layer of the particle is asymmetric due to the ion gradient. At the higher ion concentration side, the double layer thickness is smaller than at the lower ion concentration side. Such asymmetry generates an ion pressure unbalance inside the double layer triggering a fluid flow toward the lower ion concentration side.

Table 1.2 lists typical swimmers based on diffusiophoresis. Normally the diffusiophoretic mechanisms generate weaker forces than the pure electrophoretic ones under similar motor size conditions. Higher propulsion speeds can be observed due to high concentration of fuel or the use of more reactive fuels such as N_2H_4. Very remarkable is the high diffusiophoretic velocity of Amberlite based motors. Amberlite is an ion exchange polymer and motors based on such material are moved by ionic diffusiophoresis activated by ion exchanges not only at the surface but also in bulk, which results in high speed propulsion in presence of salts.

Table 1.2 summary of swimmers based on diffusiophoresis

Geometry	Material composition	Fuels/solvent	Propulsion	Reference

			speed	
Janus particle	polystyrene/Pt	1–10% H_2O_2	1-3 bdl/s	25
Janus particle	SiO_2/Pt	15-23.7% H_2O_2	9-12 bdl/s	26
Janus particle	carboxylate polystyrene/Ti/Pt	3–15% H_2O_2	0.4-1.8 bdl/s	27
Janus particle	amberlite/PECA/PMMA	1 M NaCl	500 bdl/s	28
Janus particle	SiO_2/Ir	0.001% N_2H_4	20 bdl/s	29
Janus particle	fluorescent polystyrene/Pt	10% H_2O_2	6 bdl/s	30

1.2.1.3 BUBBLE PROPULSION

The third way to drive the motor in nanoscale by chemical reaction is through bubble propulsion. Motors that utilize this type of motion are usually in tubular shape or with large exposing areas of catalyst. The force from the release of the bubbles generated at their catalytic side results in the motion.[31] In this mechanism, oxygen or hydrogen bubbles can be generated through catalytic H_2O_2 decomposition on noble metals/catalase enzyme or through the electrochemical reduction of water mediated by very active materials (e.g. Mg, Al, etc.). When bubbles detach from the motors, the associated recoil force pushes the motors in the opposite direction.[32] Apart from the catalyst nature, other parameters like fuel concentration, surface area, geometrical confinement, etc. also play a role in such mechanism. Tubular motors with the catalyst in their interior have become ideal references for bubble propulsion. The catalyst internally confined facilitates fast nucleation and growth of gas bubbles (even at low chemical fuel concentration). Moreover, the slightly conical tube geometry allows rectifying bubble propulsion in the direction of bigger tube diameter. Table 1.3 lists typical swimmers based on bubble propulsion.

Table 1.3 summary of swimmers based on bubble propulsion

Geometry	Material composition	Fuels/solvent	Propulsion speed	Reference
Tube	Ti/Cr/Pt	5% H_2O_2	200 bdl/s	33
Tube	PANI (polyaniline)/Pt	0.2% H_2O_2	350 bdl/s	34
Tube	Ti/Fe/Au/Pt	3–15% H_2O_2	1.25-50 bdl/s	35
Tube	Ti/Fe/Au/Ag	5% H_2O_2	12 bdl/s	36
Tube	SiO/SiO_2/Au/catalase	2% H_2O_2 /	3 bdl/s	37

		0.05% SDS		
Tube	Fe/Pt	3% H_2O_2 / 1% SDS	2-16 bdl/s	38
Tube	InGaAs/GaAs/(Cr)Pt	20% H_2O_2	18 bdl/s	39
Janus particle	Amberlite/Pd	5% H_2O_2	7 bdl/s	40
Janus particle	Al/Ga/Ti	H_2O	150 bdl/s	41
Janus particle	SiO_2/Ti/Pt	5% H_2O_2	1000 bdl/s	42
Janus particle	Mg/Pt	0.1–1 M $NaHCO_3$	3 bdl/s	43
Janus particle	Al/Ti/Pd	0.1 M HCl 0.1 M NaOH 10% H_2O_2	1.8 bdl/s 1.25 bdl/s 1.75 bdl/s	44

1.2.2 PUMPS

As mentioned above, a pump can be considered as an immobilized motor/swimmer, with the fluid flowing relative to its interface triggered by electric potential or concentration gradients. Therefore, similar mechanisms operate in micropumps, under the name of electro-/diffusio-osmosis instead of electrophoresis/diffusiophoresis. The mechanisms triggered by chemical reactions for swimmers and pumps are summarized in figure 1.4. Pumps turn out very useful platforms for better evaluating and understanding the chemically propulsion mechanisms. In the chemomechanical actuation chemical reactions are coupled to the equations governing mass and charge transport, electric field and fluid flow which make the overall understanding of motion more complex. As the analysis and quantification of a moving object such as a swimming motor makes its study rather challenging, pumps emerge as model systems for better probing the mechanism controlling phoretic motion. Effective experimental methods can be implemented more easily to spatially quantify the key parameters involved in such coupled processes (i.e., chemical rates and gradients, electric fields, fluid flow, zeta potential, etc.). Moreover, catalytic pumps have the advantage of being better defined and controlled from the point of view of component shape, size, surface chemical composition and roughness, which are important aspects affecting the catalytic motion and not so easy to control on freely-suspending nanomotors.

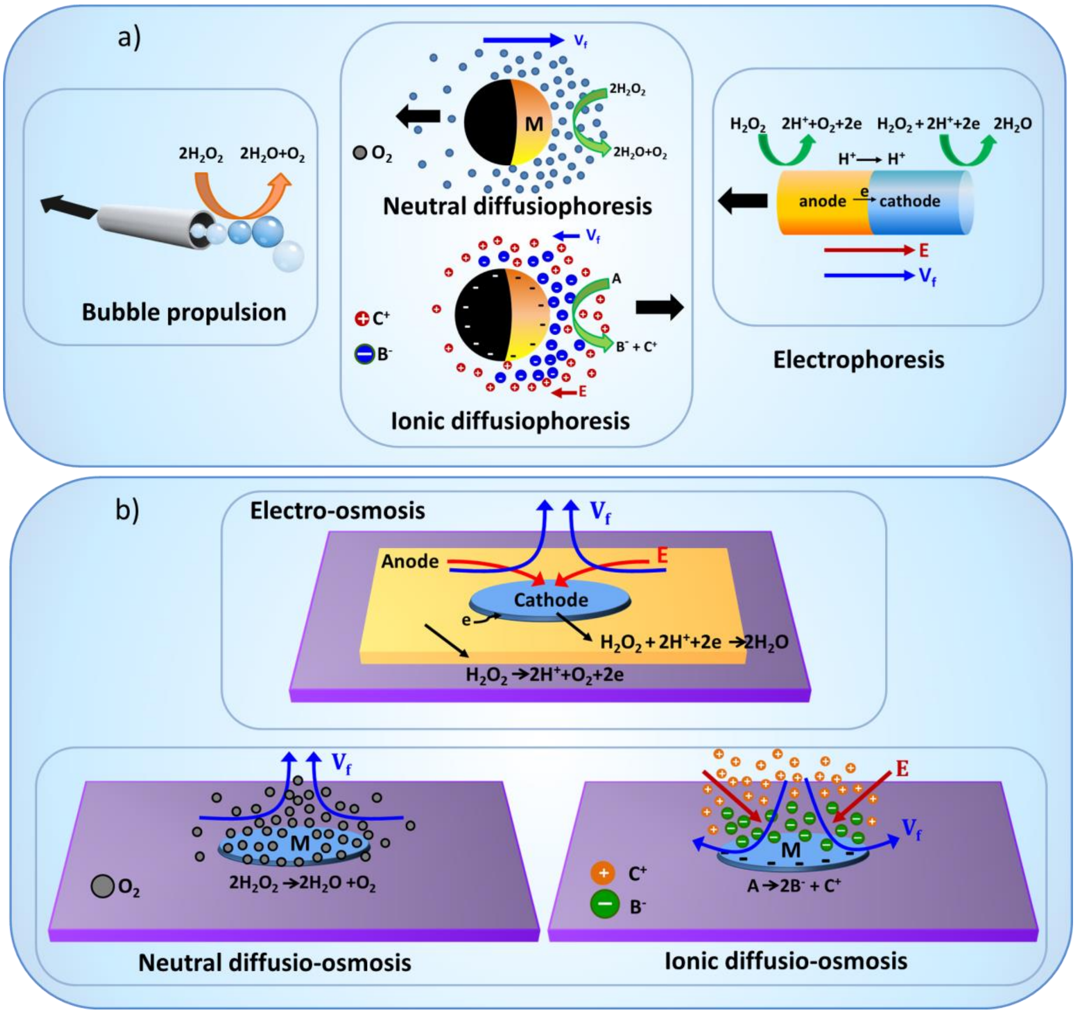

Figure 1.4 Schematic representations of the different propulsion mechanisms in a) swimmers and b) pumps triggered by chemical reactions.[45]

Therefore many efforts were first devoted to characterizing bimetallic Au/Pt micropumps in the presence of H_2O_2, as they represented the counterparts of the pioneering Au/Pt swimmers.[46] Many details were unknown on the mechanism itself, the electrochemical reaction production, electric field generation and surface chemistry effects. A set of experimental techniques together with numerical simulations were applied to provide a better scenario of the chemomechanical actuation and to identify the key parameters affecting the process.[47] For instance in order to probe the mechanism and quantify the relevant electrohydrodynamic parameters (e.g., strength and direction of the self-generated electric field, fluid flow and zeta potential), the pumps were probed with differently charged tracer particles, including positive, negative and quasi-neutral ones and evaluated their motion. For extracting the electrohydrodynamic parameters, it was considered that the radial velocity (V_{rp}) of the tracer particles had two contributions: one coming from their charge (electrophoretic velocity, V_{ef}) and the other arising from the fluid flow (V_{rf}),

$$V_{rp} = V_{ef} + V_{rf} = \frac{\varepsilon \xi_p E_r}{\eta} + V_{rf} \qquad (1)$$

where ε is the fluid permittivity, ξ_p the particle zeta potential, E_r the radial component of the electric field, and η the fluid viscosity. Figure 1.5a summarizes the different types of motion observed with the differently charged particle tracers. Figure 1.5 c, d also shows the quantification of the radial strength of the electric field and fluid flow extracted from the velocities of positive (p^+) and quasi-neutral (p^0) particles (Fig. 1.5b) using equation 1,

$$E_r(r) = \frac{\eta\left(V_r^{p+}(r) - V_r^{po}(r)\right)}{\varepsilon\,(\xi_{p+} - \xi_{po})} \qquad (2)$$

$$V_f(r) = \frac{(\xi_{p+} V_r^{po}(r) - \xi_{po} V_r^{p+}(r))}{(\xi_{p+} - \xi_{po})} \qquad (3)$$

With the calculated values of $E_r(r)$ and $V_f(r)$, the substrate zeta potential (ξ_w) was estimated from the standard expression of the electrosmotic velocity:

$$V_f(r) = -\frac{\varepsilon \xi_w E_{r\,(r)}}{\eta} \qquad (4)$$

That was an important parameter to know since it is key for determining the fluid flow motion when an electric field is generated. In order to probe the electrochemical reaction in such bimetallic pumps, the proton distribution was mapped with fluorescent pH indicators using ratiometric confocal fluorescence microscopy.[46]

Based on these findings, it was concluded that the Au/Pt pump worked by electro-osmosis driven by an electric field generated by H_2O_2 oxidation and reduction at Au and Pt respectively. The redox reaction produced protons at the anode that were consumed at the cathode, building up the proton gradient that induced a current, and hence the electric field which triggered the fluid flow.[46]

In addition to helping to understand the motion mechanism of swimmers, the pumps also enabled highlighting the impact of the physicochemical surface effects on the chemomechanical performance resulting from discrepancies on the redox role of the metals when comparing Au/Pt pumps and swimmers. For instance, it was found that, in the case of swimmers, Pt behaved as anode for H_2O_2 decomposition, with the consequent proton production, whereas Au behaved as cathode, with proton consumption, inducing an electric field in opposite direction, from Pt to Au.[48] The authors attributed the discrepancy between pumps and swimmers to surface chemistry effects, which were well-supported by XPS and electrochemical Tafel measurements.

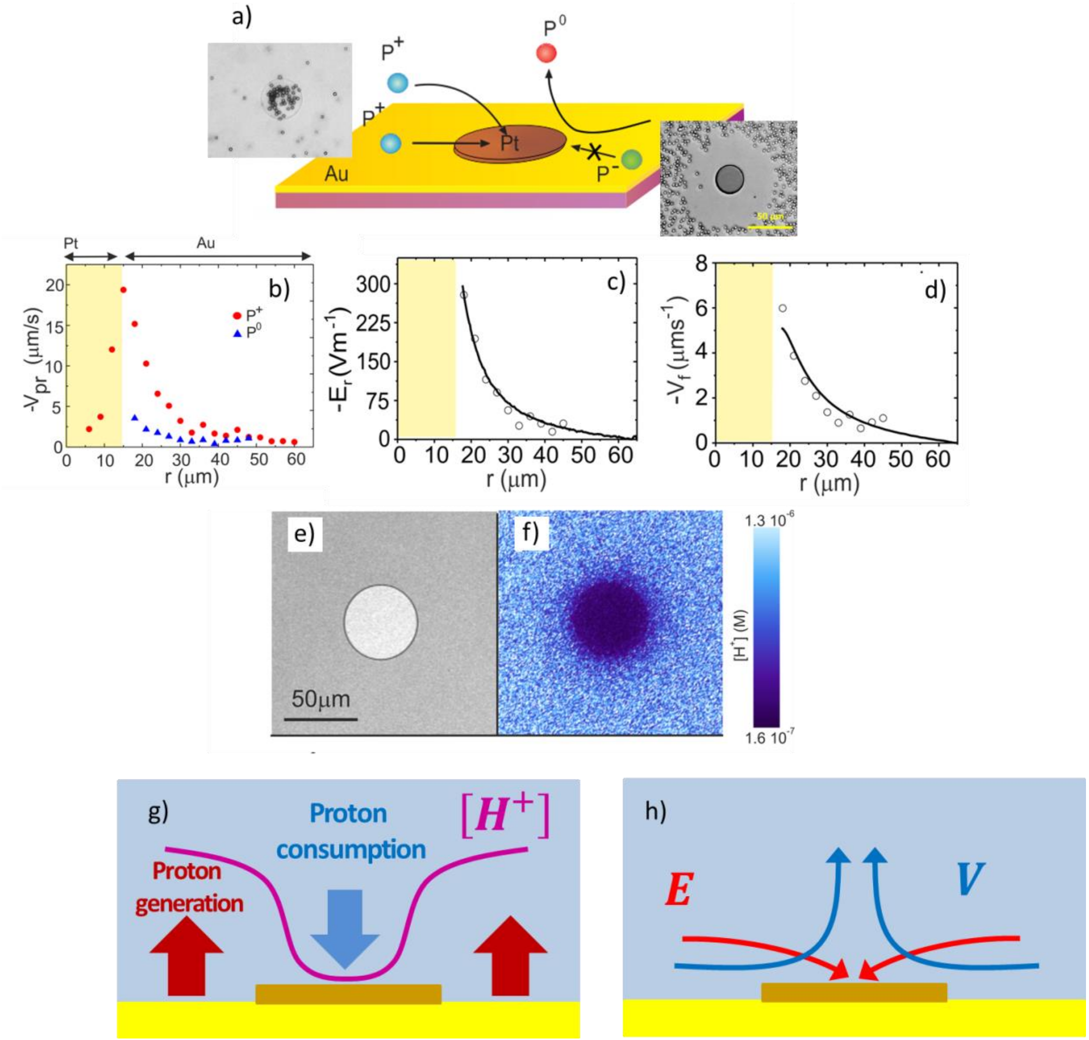

Figure 1.5 a) Scheme depicting the behavior of differently charged tracers together with an optical image of the pumps interacting with positive and negative tracers in 1% H_2O_2. Positive tracers moved toward the Pt disc, whereas negative particles got expelled forming a repulsion area around the Pt edge. Such behavior indicated the presence of an electric field pointing toward the Pt disc. Quasi neutral particles moved toward the disc but then drifted upwards in the direction normal to the disc tracing the liquid flow. b) Radial velocity of positive (p^+) and quasi-neutral (p^0) particles as a function of the radial coordinate. The origin of the plot corresponds to the centre of the Pt disc that spans an area represented by the yellow region. Experimental (circles) and simulation (solid lines) results of the radial electric field (c) and fluid velocity (d) as a function of the radial coordinate. Both the radial fluid velocity and electric field increase as the disc center is approached. Optical image of the Pt/Au pump (e) together with a proton mapping (f). Schematics representing the proton production and consumption (g) and the electric field and fluid flow direction at the pump (h).[45]

The authors harnessed such apparent discrepancy to highlight the crucial role of the surface chemistry on the electrode activity of Au and Pt. It was concluded that the electrocatalytic activity was very sensitive to the surface characteristics of the materials involved which, in turn, was very dependent on the different environments in which these materials were fabricated or exposed. Indeed, both Au and Pt are good materials for catalysing the oxidation or reduction of hydrogen peroxide. However, when they are in contact, one of these metals will preferably act as anode and the other as cathode for hydrogen peroxide decomposition and small changes in their surface chemistry (ion adsorption, oxygen moieties, etc.) can make their roles be exchanged. Since Au/Pt swimmers and the pumps follow different fabrication routes, it was not surprising that the redox role of Au and Pt could be switched and consequently the electric field and fluid flow direction.

1.3 SELF-PROPULSION BY PHOTO-CHEMICAL REACTIONS

1.3.1 SWIMMERS

Light driven synthetic motor is gaining interest, as light becomes a tool to control its motion. Light provides a possible way for the remote control of the motion, which is renewable, easy to control, and very versatile in various potential applications mentioned above. Similar to the self-propulsion mechanisms by chemical reactions discussed in section 1.2.1, the mechanisms of photo-chemically powered swimmers can be classified as light-induced self-diffusiophoretic propulsion, light-induced bubble propulsion, and light-induced self-electrophoretic propulsion. Figure 1.6 illustrates the propulsion mechanisms taking Janus particle as an example. Light-induced self-diffusiophoretic propulsion results from the asymmetrically generated gradients of photocatalytic electrolytes and non-electrolyte products. In contrast, light induced self-electrophoretic propulsion is enabled by the electric field built-up from the asymmetric distribution of ions across the bipolar motor system and consequent ionic current as a result of the light activated redox reactions taking place at different regions of the motor; bubble propulsion is caused by the ejection of a jet of bubbles from swimmers.[49]

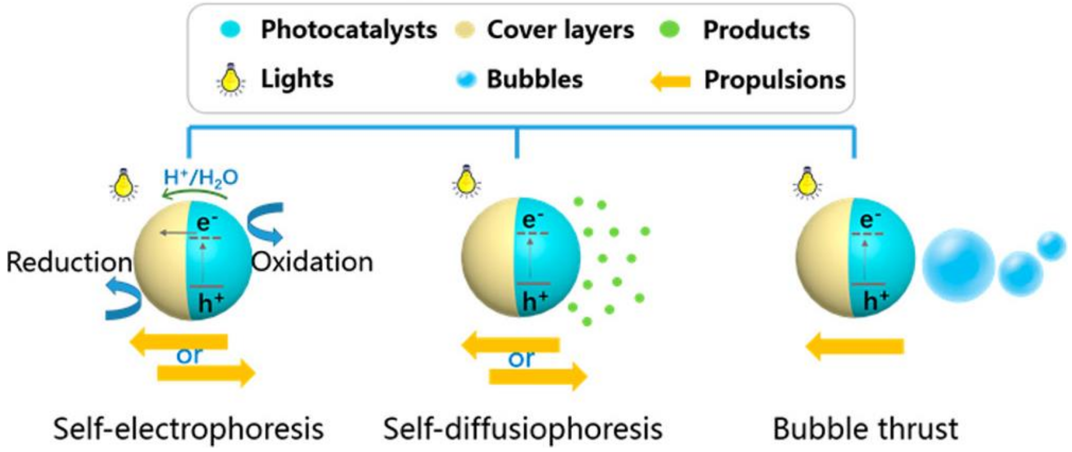

Figure 1.6 propulsion mechanisms of photo-chemically powered swimmers[49]

Most of the reported light-induced bubble propulsion methods of micro-/nanomotors are dependent on the photocatalytic decomposition of H_2O_2 with the help of photocatalysts (e.g. TiO_2 or WO_3).[50,51]

$$2H_2O_2 \overset{hv}{\rightarrow} 2H_2O + O_2$$

As an example, Li et al. reported a UV light-harvesting amorphous TiO_2/Au Janus micromotor with a diameter of about 15 µm. The motor was driven by bubble propulsion which was generated by the photocatalytic decomposition of H_2O_2 at the sensitized amorphous TiO_2 part.[52] In this way, large amount of bubbles were generated from the bare amorphous TiO_2 surface, and ultimately bubbles ejection drived the micromotor forward. The photocatalytic propulsion mechanism of the amorphous TiO_2/Au Janus micromotor in 15wt% H_2O_2 solution is shown in Figure 1.7.

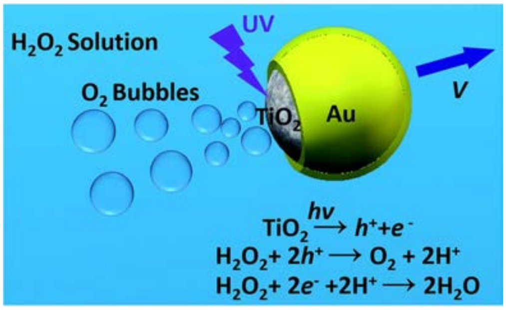

Figure 1.7 Schematic demonstration of the UV-driven motion of the amorphous TiO_2/Au Janus micromotor in 15wt% H_2O_2 solution.[52]

Bubble free light-induced micro-/nanomotors have also been reported. A similar TiO_2/Au UV light-driven Janus micromotor with a diameter of 1 μm was demonstrated in pure water without the presence of H_2O_2.[53] The propulsion of the TiO_2/Au micromotors dominantly originated from the light induced self-electrophoresis. The photoactivity of TiO_2 came from its hole−electron separation triggered by photons of energy equal to or higher than its bandgap. The conduction band of Au lies below that of TiO_2, and as a result, the Au hemisphere acted as a sink for electrons, increasing electron−hole pair lifetime and recombination times, which resulted in enhanced reactivity on the micromotors surfaces.[54] The schematic of such catalytic TiO_2/Au Janus micromotors powered by UV light in water is shown in Figure 1.8.

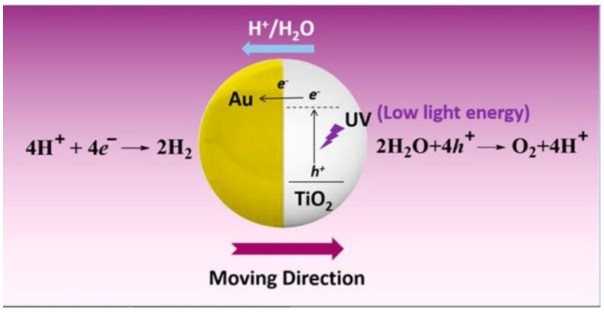

Figure 1.8 Schematic of catalytic TiO_2/Au Janus micromotors powered by UV light in water.[53]

As can be observed, even in the same kind of TiO_2/ Au system, the Janus particle may be driven by bubble propulsion or electrophoresis. The modification of particle size, surface coverage, surface roughness or chemical fuel concentration may make one mechanism dominate over the other.

Table 1.4 summarizes typical photocatalytic swimmers. Many reported systems are activated by UV light, which limits its medical applications, among others. Hence there is a high demand to convert environmentally friendly energy from visible light and low intensity near infrared light to swimmer propulsion.

Table 1.4 Summary of typical photocatalytic swimmers

Geometry	Light source	Propulsion mechanism	Material composition	Fuels/solvent	Propulsion speed	Reference
Janus particle	UV	Bubble propulsion	TiO_2/Au	15% H_2O_2	6 bdl/s	52
Janus	UV	Self-	TiO_2/Au	H_2O	25 bdl/s	53

particle		electrophoresis				
Janus particle	UV	Self-electrophoresis	TiO_2/Pt	H_2O	60 bdl/s	55
Janus particle	Visible	Self-electrophoresis	BiOI/Au	H_2O	0.8 bdl/s	56
Rod	Visible	Self-diffusiophoresis	Fe_2O_3	10% H_2O_2	1.5 bdl/s	57
Tube	UV	Bubble propulsion	ZnO/Pt	10% H_2O_2	30 bdl/s	58
Particle	UV	Self-diffusiophoresis	AgCl	H_2O	100 bdl/s	59
Particle	UV	Bubble propulsion	TiO_2/Au/Mg	H_2O	4 bdl/s	60

1.3.2 PUMPS

The Pt/Si pump system has been demonstrated to be a useful tool to probe photoactivated reactions for triggering fluid motion.[61] Such micropump has the capability of being controlled with visible light provided by the low band-gap silicon. It was shown that the pump could be even fuelled by just water under visible illumination, although an enhancement of the catalytic actuation was achieved when using more reactive species, such as H_2O_2. The authors evaluated the pump photochemical actuation by mapping the proton gradient with fluorescent pH indicators and extracted the electrohydrodynamic parameters using differently charged tracers.

For instance, figure 1.9a showed the proton gradient map generated by the Si/Pt pump in water under visible light illumination. High proton concentration was observed on the silicon side, whereas proton depletion was observed on the metal side. The production of protons at silicon supported the existence anodic reactions mediated by water at the semiconductor interface, whereas the proton decrease on the metal side was compatible with proton consumption due to cathodic reactions at the Pt interface. By contrast, no proton gradient was generated when an insulating layer was placed between the metal and the semiconductor, as depicted in Figure 1.9b. This finding revealed that transfer of electrons between the semiconductor and the metal is important to make this pump operative.

The interaction of the pump with different charged colloidal tracers also supported the redox behaviour of Si as anode and Pt as cathode. In presence of the optical microscope white light, the electrohydrodynamic process was triggered. Positive tracers moved toward the Pt disc and stuck on it, negative particles were repelled from the Pt disc and quasi neutral tracers moved to the disc and then drifted upwards. The proton gradient and the trajectories of charged particles indicated an electro-osmotic mechanism with a self-generated electric field and fluid flow pointing in the same direction from Si to Pt disc.

The most remarkable aspect of these photochemically activated pumps was the tunability of the chemomechanical actuation with light intensity. The light became a powerful tool to selectively control the strength of the electric field and fluid flow and eventually the mass transport to specific locations. Figure 1.9g showed the significant velocity decrease of positive tracers obtained by attenuating light intensity with a filter. Similarly, Fig. 1.8h showed the increase of the exclusion zone of negative tracers on Pt/Si pumps achieved upon increasing light intensity. The authors explained the photoactivation of the chemomechanical actuation under the frame of a photo-catalytic effect enhanced by the presence of the metal: during silicon light absorption, electrons are excited from the valence band to the conduction band, leaving holes behind. The excited electrons are then transferred to the metal. The holes generated at the semiconductor become oxidizing agents for the fluid or for the silicon itself whereas the injection of electrons at the metal counterpart makes it acting as reducing agent. The transfer of excited electrons from the semiconductor to the metal (Au or Pt) in semiconductor/metal contact is a well-known process and has been exploited to minimize electron-hole recombination and hence to increase the efficiency of photo-catalysis in different applications.

The output of Si/metal pumps has become very appealing for the future development of light-activated functional structures. These visible light-driven machines with the additional capability to work using just water hold relevant promise not only as switches for controlled mass transport in fluids but also for photoactivated driven swimmers operating with a more innocuous light source and fuel.

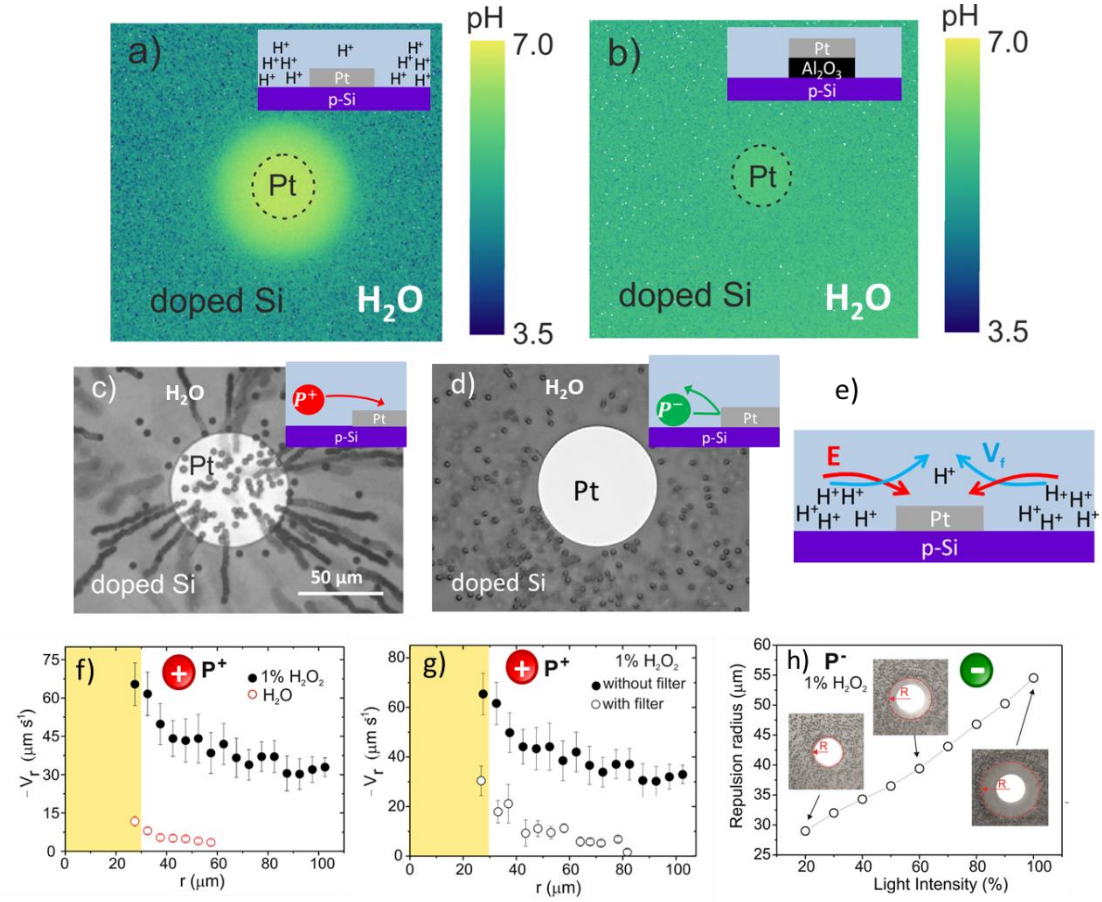

Figure 1.9 Mapping of the proton distribution on Pt/Si pumps (a) and Pt/Al_2O_3/Si in water (b). No proton gradient is generated at the pump when using an insulating layer between Pt and Si. Motion of positive tracers towards Pt disc (c) and repulsion of negative tracers from Pt (d). (e) Schematics depicting direction of fluid flow and electric field. (f) Comparison of the radial velocity of positive tracers in H_2O and H_2O_2. Effect of light on positive (g) and negative (h) tracers. The radial velocity of positive particles decreases when using intensity attenuators and the repulsion of the negative tracers also decreases when lowering light intensity.[61]

1.3.3 COLLECTIVE BEHAVIOUR IN (PHOTO)CHEMICALLY ACTIVATED MOTORS

The close analogy of artificial self-propelled materials to their biological counterparts has deserved them the qualification of active matter. In such repertoire of motor functionalities the study of collective behaviour of self-propelled objects is emerging as a frontier topic in fundamental science, especially in the non-equilibrium statistical physics community.[62,63] Collective behaviour involving cooperative arrangements of individual objects is an ubiquitous phenomenon that exists from the macro to the nanoscale level (e.g. animal herds, flock of birds, army of ants, bacterial colonies, polymeric scaffolding governing transport adhesion movement and division in the living cell, etc.). For instance, swarming of bacteria helps to access new sources of nutrients, to increase the size of the community, and to colonize niches.[64] Taking cells into consideration, there is also increasing evidence that collective cell migration is common during invasion and metastasis of tumours.[65] In biological systems the collective effects emerge as a consequence of object intercommunication through (bio)-chemical signalling or external stimulus. Similarly, artificial self-propelled systems generate local chemical gradients which trigger diffusiophoretic/electrophoretic phenomena and fluid flows which can in turn, move and reorient other swimmers nearby. In this way, the swimmers would be inducing a kind of signalling to the neighbours influencing their interactions with the consequent built-up of microscale assemblies or organized configurations that could never be reached with passive objects in an equilibrium regime.[60-62] This is a very promising topic to harness functional synergy of self-propelled motors for different tasks though there are still many open questions regarding the critical parameters that allow the transition from individual to a collective performance.

Figure 1.10 shows some examples of studies performed with self-propelled colloids which were activated by chemical or photochemical reactions. The objects respond to concentration gradients created by themselves and by their neighbours resulting in different modes of collective behaviours. These examples include the reversible chemically swarming or schooling of motile particles,[66,67] the photochemical dynamical self-assembly of motor colloids,[68] the light-driven explosion of particle swarms (micro-fireworks)[69] and predator-prey behaviour between motile and passive colloids[70]. The main driving forces for the emergence of such collective interactions are rooted in the complex interplay of phoretic, osmotic and hydrodynamic effects. Thus, swimmers which can mimic collective phenomena in nature at the micro/nanoscale can be used not only as model systems for providing insights into living systems but also can be exploited to develop new routes of more efficient cooperative tasks in the different applications.

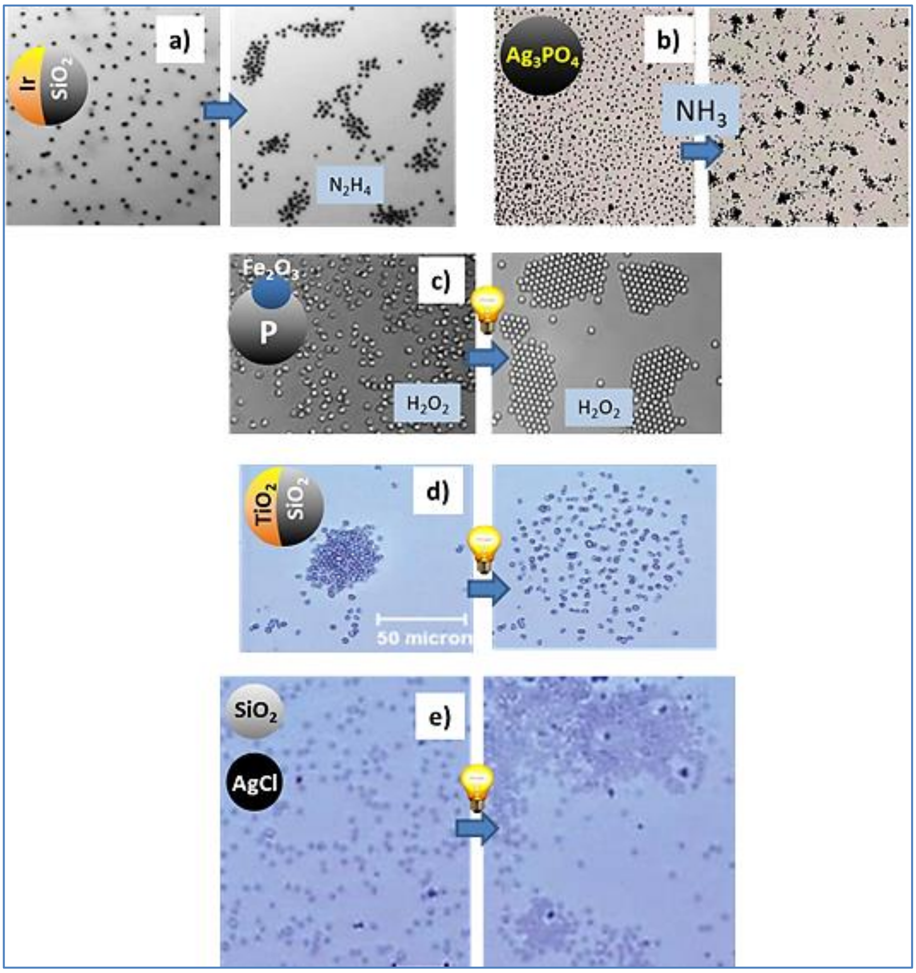

Figure 1.10 a) Swarming behaviour of Janus Ir/SiO_2 micromotors in presence of N_2H_4 due to diffusion-osmotic and diffusiophoretic effects (reproduced from ref. 65). b) Ag_3PO_4 particles showing reversible transition between exclusion and schooling which are triggered by shifting the chemical equilibrium with the addition or removal of ammonia (reproduced from ref. 66). c) Active Janus motors made of magnetite and polymer which self-assemble in presence of H_2O_2 under illumination with blue light due to the photochemical generation of chemical gradients (reproduced from ref. 67. d) Repulsion of aggregated TiO_2-SiO_2 particles under UV illumination (reproduced from ref. 68 e) Predator-prey behaviour in photoactive AgCl colloids (prey, darker objects) and passive silica colloids (predator, lighter objects). Without UV light particles are randomly dispersed, when illuminated with UV light the silica colloids surround their prey and an exclusion zone is seen around the AgCl particles. The effect is triggered by the chemical and electric fields generated by the active AgCl colloids (reproduced from ref. 69).

1.4 OTHER PROPULSION MECHANISMS AND TOOLS TO CONTROL MOTION

So far, all the mechanisms outlined above use a chemical fuel. However, there are other chemical fuel-free propulsion mechanisms, e.g. self-acoustophoresis, self-thermophoresis, as well as mechanisms that follow the gradients generated by external fields. Those external fields can also precisely control the motion of motors and can be even combined with chemical fuels simultaneously. The precise control of the position via external physical fields (including optical, magnetic, electric fields, and acoustic waves) is a critical step in realizing the applications in nanofactories and nanorobots, which could lead to a variety of manipulation approaches for cargo transport, drug delivery, biochemical sensing, and cell trapping.[71,72,73]

1.4.1 ELECTRICALLY DRIVEN MICRO-/NANOMOTORS

Electrically generated motion of micro-/nanoscale objects utilizes direct current (DC) and alternating current (AC) electric fields to precisely manipulate micro-/nanomotors in a liquid solution. Commonly used propulsion mechanisms are usually based on electro-osmotic nature at a low-frequency electric field. Such high-precision manipulation of micro-/nanomotors with the help of electric fields has great potential applications including micromachining, drug delivery and self-assembly of superstructures.[74,75,76] Micro-/nano-objects can be manipulated via the DC and AC electric fields which are generated by pre-patterned microelectrodes. Generally speaking, electrically triggered movement of suspended micro-/nano-objects in a liquid medium is based on the phenomena of their electro-osmotic nature in a low-frequency electric field.[75,77,78] As shown in figure 1.11, semiconductor diodes floating in water could serve as propellers and actuators in an AC field. These diodes rectified the voltage and generated a particle-localized electro-osmotic flow, and drove themselves toward the cathode or anode based on their surface charges. In addition, the propulsion of these devices could respond to light and be controlled by internal logic.[79] The diode velocity (u) as a function of the intensity of the external AC field was estimated in the equation below:

$$u = \beta \frac{\varepsilon \varepsilon_0 \zeta}{2\mu} \left(E_{ext} - E_{d_0} \right)$$

where β is the hydrodynamic-resistance correction coefficient, ε and ε_0 are the dielectric permittivity of the media and vacuum respectively, μ is the viscosity of the liquid phase, ζ is the potential in the plane of hydrodynamic shear, and E_{ext}, E_{d_0} are the external AC field and an additional field respectively.

In a similar approach, Sharma and Velev reported the possibility to control and reverse the direction of motion by tailoring electrostatic torque between the asymmetrically polarized diodes and the ionic charges redistributed in the vessel.[80]

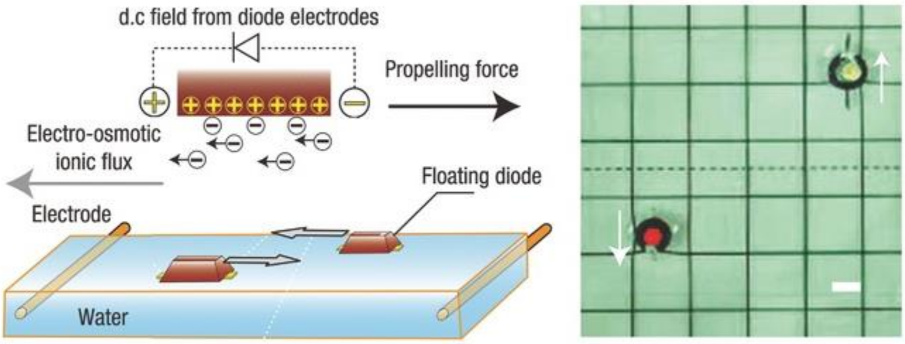

Figure 1.11 Schematic diagram (left) and optical microscopy image (right) of two lit up light-emitting diodes that move toward different directions based on their anode direction.[80]

After years of development, motion driven by the electro-osmotic nature in a low-frequency electric field has been the most useful method to position and align micro-/nanoentities along an electric-field gradient, even though the aforesaid effect leads to a big challenge for the further development of complex nanomachines and biomedical applications because of large motor size.[71]

1.4.2 Acoustic propulsion of Micro-/Nanomotors

Ultrasounds are sound waves with frequencies higher than the upper audible limit of human hearing.[81] Because one of the strong drivers of Micro-/Nanomotors research is their potential utility in biomedicine and diagnostics, there is a need to develop propulsion mechanisms that can operate in biocompatible media, including in vivo.[82,83] Ultrasonic propulsion of micro-/nanoswimmers is one of the promising methods that meets the strict requirements for high speed propulsion in biofluids with high viscosity and high ionic strength.[84]

Low power acoustic waves are proven safe and are used extensively for in vivo imaging.[85] When an external acoustic field is applied, suspended micro/nanoparticles experience acoustic radiation forces and move to the pressure nodes (or antinodes) depending on pressure gradients. When the acoustic excitation meets the criteria to form standing waves, the radiation force is the strongest and can be expressed as:[86]

$$F_{ax} = 4\pi a^3 E_{ac} k \sin(2kz)\,\Phi$$

where F_{ax} is the acoustic radiation force, a is the particle radius, E_{ac} is the acoustic energy density, k is the wavenumber, z is the distance of the particle from the node, and Φ is the acoustic contrast factor which can be expressed as:

$$\Phi = \frac{\rho_P + (2/3)(\rho_P - \rho_0)}{2\rho_P + \rho_0} - (1/3)\frac{\rho_0 c_0^2}{\rho_P c_P^2}$$

where ρ_P and ρ_0 are the density of the particle and medium, respectively, and c_P and c_0 are the speed of sound in the particle and surrounding medium, respectively. Acoustic radiation forces are the basis of ultrasonic particle manipulation techniques. However most of the acoustic studies have been performed with symmetric particles, made typically from soft polymer or biological materials such as polystyrene spheres or cells.

Ultrasound propulsion of synthetic nanowire motors was first reported in 2012 by Mallouk and co-workers.[87] Figure 1.12 demonstrated the random motion behaviour of Au/Ru bimetallic microrods (2 µm in length and 330 nm in diameter) operated in a megahertz-frequency ultrasonic system. The Au/Ru bimetallic microrods were synthesized using a template electrodeposition method, and then these metallic microrods were suspended in water in an acoustic chamber. The microrods were levitated to a plane at the midpoint of the cell where the pressure was minimum with the help of vertical standing waves. In that plane the metal microrods exhibited axial motion at speeds up to 200 µm/s in water. The microrods also formed patterns in the nodal plane as a result of nodes and anti-nodes within the plane. The composition of the microrods was found to significantly affect their movement, with only metal microparticles showing fast axial motion.

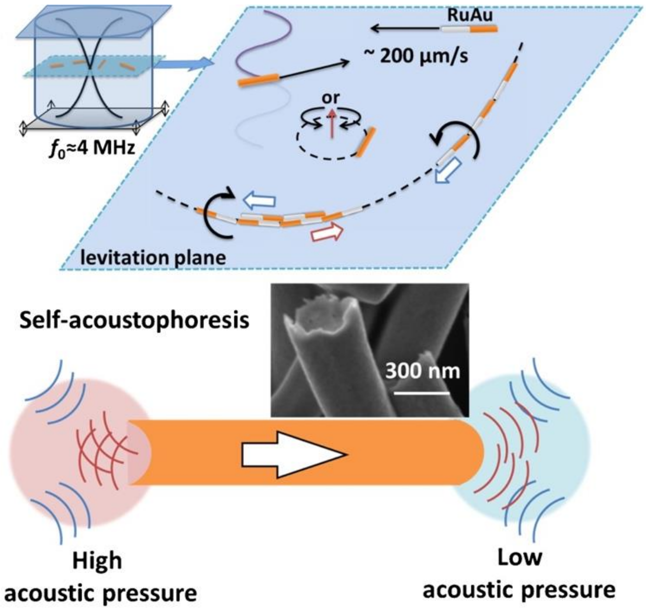

Figure 1.12 Asymmetrically shaped metallic microrods were activated in an ultrasonic standing wave at MHz frequency through a self-acoustophoresis mechanism.[87]

Although the forces responsible for acoustic propulsion of metallic microrods have not been completely understood yet, the leading candidate is a mechanism called self-acoustophoresis. This mechanism was built on the fact that the microrods fabricated always had concave ends. Thus the strong axial propulsion of these metallic microrods has been proposed to originate from the differential scattering of acoustic waves at the ends of the rods. Asymmetric scattering of acoustic waves causes a pressure gradient that is high at the concave end and low at the convex end, with a difference of ca. 1 Pa. It was further determined that the scattered acoustic waves were traveling in the z direction instead of propagating in the xy plane (the plane where the motors travel) through an estimate of the forces within this system.[88]

A number of critical challenges remain to be addressed in the acoustic propulsion of nanowires for biomedical applications. Self-acoustophoretic metal nanorods are similar in size to bacteria, but they have relatively lower power and speed. They also require an acoustic standing wave. It goes without saying that notable research is needed for acoustic micromotor to become a potential candidate for biomedical applications.

1.4.3 MAGNETIC MICRO-/NANOMOTORS

Due to the non-invasiveness, high penetration, and strong controllability, magnetic fields have been widely used as a driving force for the propulsion of micro-/nanomotors.[89,90,91] Ferromagnetic components can be incorporated within the motor systems and respond to the corresponding external magnetic field.

The so-called magnetophoresis, the motion induced by the external magnetic field in a fluid, is a simple way to guide micro-/nanomotors.

Based on propulsion mechanisms and micro-/nanostructures, there are mainly three types of magnetic micro-/nanomotors: surface walkers, flexible swimmers, and helical swimmers.[92]

Magnetic surface walkers depend on a boundary surface to break the spatial symmetry and thus create the propulsion.[93,94] Based on this idea, Tierno et al. reported in 2008 DNA-linked asymmetric doublets consisting of two different diameters of paramagnetic colloidal micro-particles.[95] The propulsion velocity of such particles can be manipulated by the strength and frequency of the actuating magnetic field. Self-assembled colloidal rotors composed of multi-superparamagnetic beads have also been reported. Later in 2009, straightforward manipulation along the surfaces of such surface walkers in a rotating magnetic field was demonstrated which provided a simple and versatile approach for studying fundamental problems in cooperative-driven motion and transporting cargo at nanoscale.[96] Zhang et al. presented magnetically propelled rotating nickel nanowires in 2010.[97] The nanowires exhibited a tumbling motion under a uniform rotating magnetic field. In addition, the nanomotors were able to transport a polystyrene micro-bead over a flat surface or even across an open micro-channel.

Magnetic flexible micro-/nanomotors inspired by swimming microorganisms such as cilia and flagella have been also demonstrated.[98] As shown in figure 1.13, these swimmers were propelled by the asymmetric deformation of elastic flexible filaments.[93] Dreyfus et al. reported a microscopic magnetic swimmer based on a DNA-linked chain of colloidal paramagnetic beads, which played as a flexible artificial flagellum and could be propelled toward the opposite direction of the bending-wave propagation in an external alternating magnetic field (Figure 1.13a). The velocity and direction of the motion could be manipulated by the strength and frequency of the magnetic field.[99] Ozin's group introduced flexible metallic nanorods linked by polyelectrolyte hinges, which displayed considerable flexibility and could be actuated by magnetically induced bending.[100] Gao et al. developed a facile method based on anodic aluminium oxide (AAO) membrane template to fabricate flexible three-segment Au/Ag/Ni nanowire motors. The fabricated Au/Ag/Ni nanowire, which consisted of an Au “head”, a Ni “tail” and a flexible Ag “joint” in between, was propelled by cone-shaped rotation of the Ni segment using a rotating magnetic field.[101] Later on, the similar flexible magnetic Ni/Ag swimmers (5–6 µm in length and 200 nm in diameter, as shown in Figure 1.13b) were able to move in human serum at high speeds.[102]

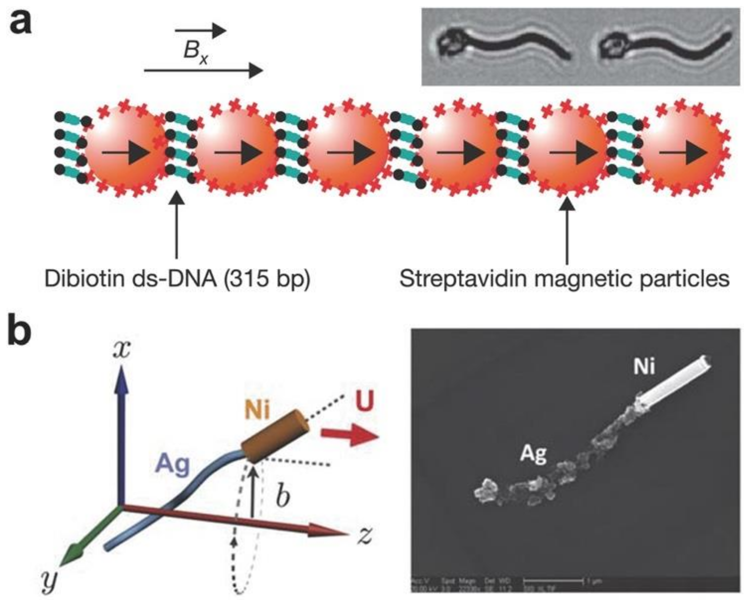

Figure 1.13 Flexible magnetically propelled micro-/nanomotors.
a) Flexible magnetic artificial swimmers based on DNA-linked nanoparticles.[99] b) Magnetically powered Ni-Ag nanowire swimmer.[102]

Magnetic helical micro-/nanomotors, which are inspired by helical bacterial flagella, are propelled by rotating their helical structure similar to a screw in the presence of a reversible magnetic field.[103] These devices have the ability to navigate in various types of biofluids and can be applied in different biomedical applications.[104] Typical magnetic helical micro-/nanomotors consist of a magnetic material and a helical body. The magnetic material enables the helical structure to rotate under an external rotating magnetic field. The optimal helical propulsion is a pure rotation around and a pure translation along its helical axis. There are several factors influencing its motion. One phenomenon is the wobbling of helical swimmers at low frequencies (Figure 1.14a). In addition, the magnetization direction of the swimmer plays a role in the swimmer alignment with respect to the helical axis.[105] The helical swimmer stabilizes at high actuation frequencies as demonstrated in Figure 1.14b.

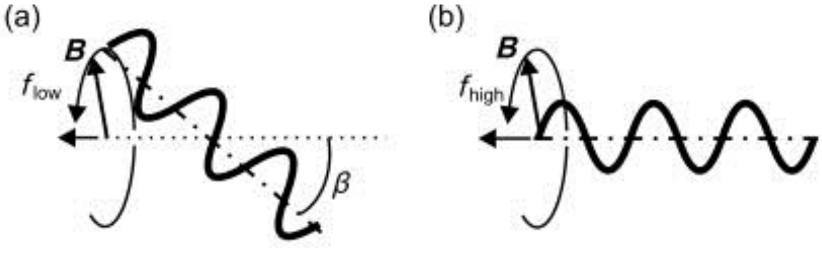

Figure 1.14 Motion of helical swimmers.[106] a) At low frequencies the swimmer wobbles with a wobbling angle β. b) The wobbling decreases at high rotational frequencies.

The velocity (U) of magnetic helical motor is given by the equation below, which is proportional to the characteristic length:[106]

$$U = \frac{(C_n - C_1)\sin\theta\cos\theta}{2(C_n\sin^2\theta + C_1\cos^2\theta)} d\varpi$$

where C_n and C_1 are the drag coefficients perpendicular and parallel to the filament, θ is the helix angle, and d and ϖ are the diameter of the helix and the rotational frequency, respectively.

The magnetic propulsion mechanism is one of most widely used fuel-free methods to power micro-/nanomotors. Much effort has been made to develop the fabrication techniques of magnetic micro-/nanomotors. Many improvements are still needed, however researchers have already started to employ magnetic micro-/nanomotors in preliminary biological and medical applications, such as precisely targeted drug or gene delivery[107,108], cell transportation[109,110], in-vivo operation[111], and invasive surgery[112].

1.4.4 THERMAL PROPULSION

Light can induce thermophoresis in micro/nano-objects that contain metal components such as Janus particles.[113] In principle, such motors are able to generate thermal gradients at their surface by absorbing different amounts of light at the different segments when they are under illumination. Generally platinum or gold segments of the Janus particle, which act as photothermal agents, generates a large amount of heat with near-infrared (NIR) due to the surface plasmon resonance (SPR).[114] Such photothermal effect transforms the absorbed electromagnetic wave into heat and then creates a thermal gradient to drive the motor. The thermophoretic velocity (U) is described by the following equation:[115]

$$U = -DS_T\frac{\Delta T}{3R}$$

where D is the diffusion constant of the particle, S_T is the Soret coefficient, ΔT is the temperature difference between the two sides of Janus particles, and R is the radius of the particle.

For instance, figure 1.15 showed the steady-state temperature distribution for a 50 nm mesoporous silica based Janus particle under 3W/cm^2 NIR irradiation. A sudden temperature increase at the interface between the Janus particle and the water could be observed.[116] The generated self-thermophoresis could drive the nanomotors at a fast speed of up to 950 body lengths/s under an NIR laser power of 70.3 W/cm^2.[116]

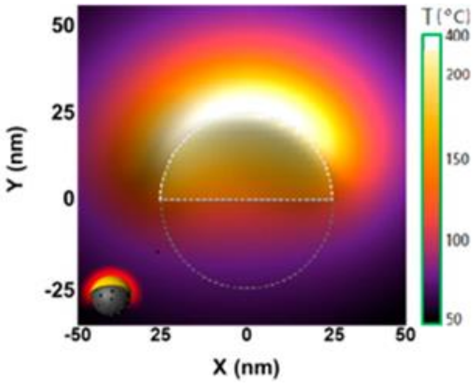

Figure 1.15. The steady-state temperature distribution for a 50 nm mesoporous silica based Janus particle under 3W/cm^2 NIR irradiation.[116]

In addition to light, thermophoresis in Janus micro-/nanoparticles can also be achieved by magnetic field. Typically, an AC magnetic field is applied to induce thermophoretic motion through heating a magnetic cap of the Janus particles, while an additional dc magnetic field is employed to steer their motion over a long time scale.[117] For instance, motion control has been achieved with the help of an ultrathin 100nm thick Permalloy (Py, $Fe_{19}Ni_{81}$ alloy) magnetic film with a topologically stable magnetic vortex state in the cap structure of Janus particles. Figure 1.16 illustrates the experimental setup for magnetic thermophoretic motion.

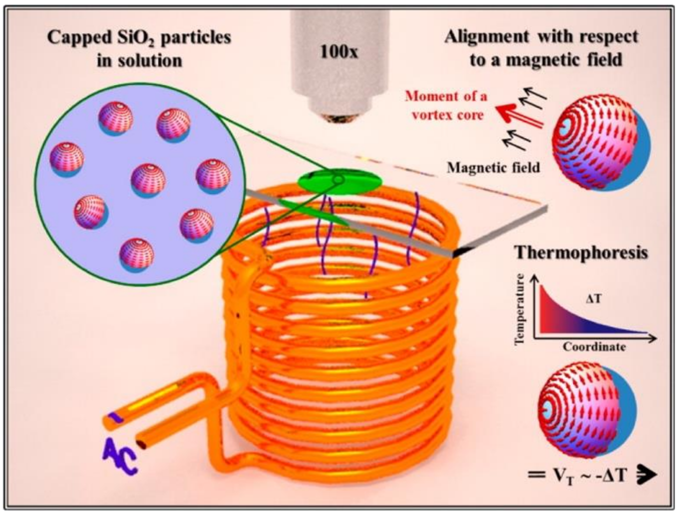

Figure 1.16 Schematics of the magnetic thermophoretic motion experimental setup: The motion is investigated by an optical microscope. A coil is positioned around the sample consisting of magnetically capped SiO_2 particles suspended in water. Local distribution of magnetization in the cap structure is schematically shown with arrows. These Janus particles can be aligned with respect to the external

magnetic field relying on the interaction between the field and magnetic moment of the vortex core. Propulsion of the particles is due to a thermophoretic force from a temperature difference between the two phases of the Janus particle in the ac magnetic field which is generated from the coil underneath.[117]

1.5 PROS AND CONS OF DIFFERENT MICRO-/NANOMOTORS

Like two sides of a coin, the advantages and disadvantages of the self-propulsion mechanisms discussed in previous sections are summarized in the table below.

Table 1.5 Summary of the advantages and disadvantages of the self-propulsion mechanisms

Propulsion mechanism	Advantages	Disadvantages
Chemical reaction	Ease of application Various fuel choices, autonomy, versatility, emergence of collective behaviours (dynamical self-organization)	Limited suitability in bio-systems Short duration of chemical gradients
Photo-chemical reaction	Ease of application Spatiotemporal control, various fuel choices, autonomy, versatility, emergence of collective behaviours (dynamical self-organization)	UV: harmful for bio application Short duration of chemical gradients
External Electrical field	Spatiotemporal control	Low penetration ability Sensitive to the surrounding medium
Ultrasound	High penetration Insensitive to surrounding medium	High energy Cavitation effect
Magnetic field	Non invasiveness High penetration Spatiotemporal control Insensitive to surrounding medium	Complex and usually large facilities
Thermal Propulsion	Ease of application Easy to achieve with light and magnetic fields	Induces environmental changes Damage to biological systems Very low energy

	conversion efficiency

1.6 FABRICATION METHODS OF MICRO-/NANOMOTORS

One goal in micro-/nanomotor fabrication is to find easy and cost-effective approaches for the applications. In the fabrication process, functionalization is an essential step toward successful realization of the applications of micro-/nanomotors. Tailored functionalization methods should be developed according to characteristics of specific types of micro-/nanomotors and relevant designed applications.
The rapid development in the field of nanotechnology has resulted in various strategies and techniques for the fabrication and functionalization of micro-/nanomotors. A range of different factors, such as shape, composition, distribution of materials and functionalization, should be taken into account in the design of such devices. In this section, various approaches to the fabrication of micro-/nanomotors are highlighted.

1.6.1 TEMPLATE ASSISTED DEPOSITION

Membrane template-assisted electrodeposition utilizes the pores of a membrane to built-up wires or rods consisted of different material segments such as polymers, metals, semiconductors, and carbons.[118,119] Because of the uniform diameters and large pore densities in the membrane, same nanostructures can be produced in a large scale. The length of the structure is proportional to the coulometric charge while the diameter is equal to the diameter of the pores. Membranes commonly used in the preparation of micro-/nanomotors are porous alumina membranes and track-etched polycarbonate membranes. The wire structure can be either solid or hollow, which is determined by the size and chemistry of the pore sidewall, the deposition rate and the properties of the material.

Bimetallic nanowire motors are mainly prepared by membrane template-assisted electrodeposition. As an example, anodic aluminium oxide (AAO) membranes with nano-sized pores have been widely used to deposit different metals sequentially into the pores and thus obtain rod-like structures (Figure 1.17). A silver or gold thin film is firstly deposited on one side of the membrane by physical vapour deposition to become the working electrode for the further metal electrodeposition. The membrane is then assembled in a Teflon plating cell with flat aluminium foil placed against the metal layer to serve as a conductive contact for subsequent electrodeposition. A sacrificial layer of silver is usually electrodeposited beforehand, followed by sequential deposition of the different desired metals. The sacrificial layer assures, later on, an easier release of the nanostructures. The silver or gold backing and the sacrificial layer can be removed by mechanical polishing or chemical etching. After dissolving the alumina membrane in NaOH solution, the nanowire motors can be finally released and collected after rinsing and centrifugation.

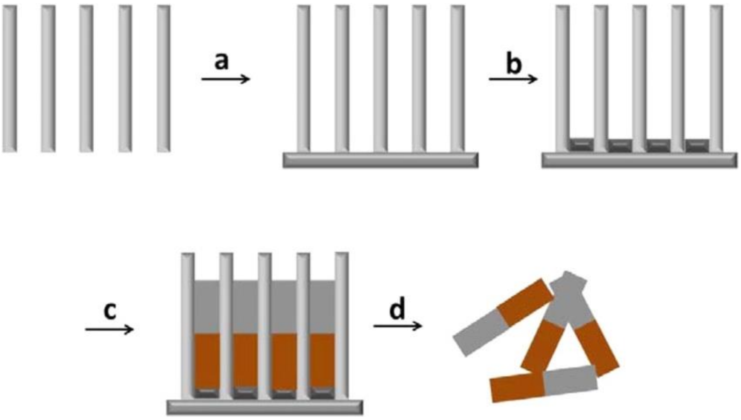

Figure 1.17 Membrane template-assisted electrodeposition of nanowires: (a) deposition of gold or silver backing on the membrane template, (b) electrodeposition of sacrificial layer, (c) sequential electrodeposition of desired components, and (d) removal of the backing and sacrificial layer, dissolution of the membrane.[120]

Apart from bimetallic nanowires, magnetic flexible nanowire motors can be prepared by the membrane template-assisted electrodeposition method with extra steps. Mirkovic et al. reported magnetically propelled flexible nanowire motors in which rigid nickel and platinum segments are connected by flexible polyelectrolyte multilayer segments.[121] Fabrication of the flexible polymer was achieved by encapsulation of Ni/Au/Pt nanowires with polyelectrolytes through layer-by-layer electrostatic self-assembly. Selective etching of the gold part with KI/I_2 solution was applied to expose the soft polymer hinges. Figure 1.18 illustrates preparation procedure of flexible metallic nanowires with polyelectrolyte hinges after membrane template-assisted electrodeposition.

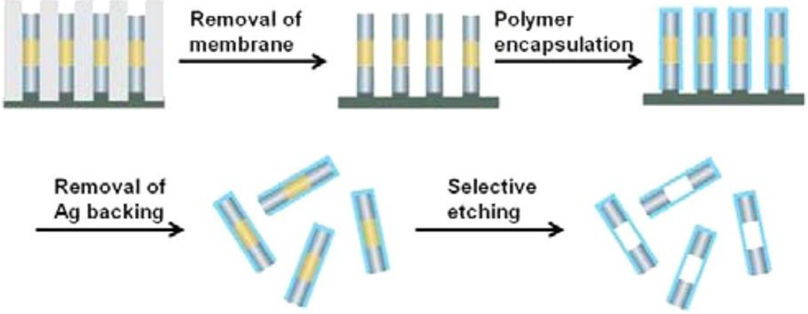

Figure 1.18 Preparation procedures of flexible metallic nanowires with polyelectrolyte hinges after membrane template electrodeposition.[121]

The membrane template-assisted electrodeposition can also be applied to fabricate tubular micro-/nanomotor. Gao et al. developed such a method for bimetallic nanowires for fabricating microtube swimmers.[122] Cyclopore polycarbonate membrane, with a symmetrical double-cone pore structure, provided a useful template for the electrodeposition of cone-like microtubes. Figure 1.19 shows the fabrication of a polymer/metal microtube. In the electrodeposition procedure, aniline monomers were first electropolymerized. A layer of platinum was subsequently deposited to form a bilayer polyaniline (PANI)/Pt microtube. The fabricated microtubes were conical with lengths of several micrometers and diameters depending on the pore size of the membrane template.

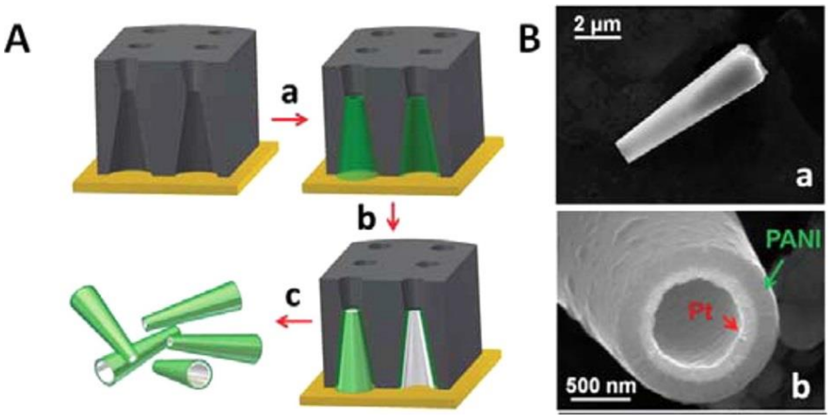

Figure 1.19 Membrane template-assisted electrodeposition of micro/nanotubes.[122] (A) Polycarbonate membrane-assisted preparation and (B) SEM images of conical PANI/Pt microtubes.

Membrane template-assisted electrodeposition is a powerful method to prepare various micro-/nanomotors.[123] Li et al. reported a method to fabricate helical magnetic microswimmers by electrochemical deposition of Pd^{2+} and Cu^{2+} inside the pores of AAO membrane templates. After releasing Pd/Cu nanorods by dissolving AAO membrane, Ni coated Pd helices were obtained through selective dissolution of Cu and e-beam evaporation of Ni thin films.[124] Figure 1.20 illustrates the process of AAO membrane-assisted preparation of helical micromotors.

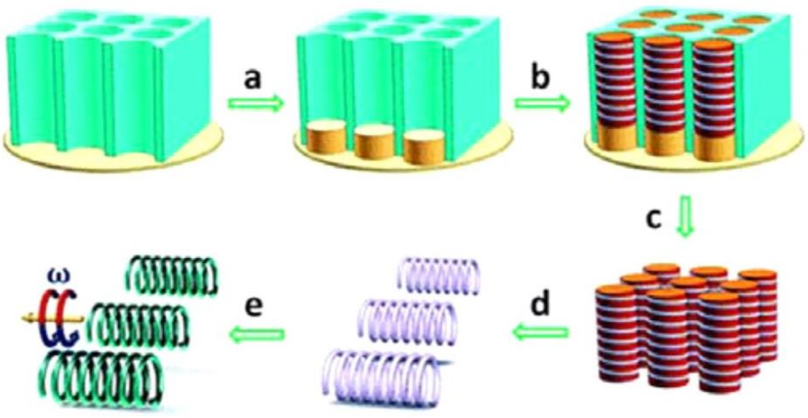

Figure 1.20 AAO membrane-assisted preparation of helical micromotors. (a) Electrodeposition of Au; (b) electrochemical co-deposition of Pd/Cu rods; (c) removal of the membrane template and the Au bottom layer; (d) etching of Cu; (e) Ni coating for magnetic actuation.[124]

1.6.2 PHYSICAL VAPOUR DEPOSITION ON SELF-ASSEMBLED COLLOIDS

Physical vapour deposition is a thin film coating technique. The vaporization of the material from a solid target is assisted by physical methods such as a high-temperature vacuum or gaseous plasma. The vapour is then delivered to substrate surface in high vacuum or ultrahigh vacuum, followed by condensation to form thin film. The two most used types of physical vapour deposition processes are sputtering and electron beam evaporation. The conventional PVD method can be applied to fabricate Janus particles, while its variation, so-called glancing angle deposition, is able to produce complex 3D structures.

In the case of catalytic Janus micro/nano-motors, the typical preparation process is the deposition of catalytic materials by PVD onto one hemisphere of the particle to break symmetry. As illustrated in Figure 1.21, the standard procedure for preparing Janus particles is to form a self-assembled monolayer of particles by colloidal lithography (see details in Appendix). Catalytic material is then deposited on top of the monolayer to form hemispherical cap layers on the surface of the particles. The Janus particles are then detached from the substrate via sonication. The diameters of the catalytic Janus motors normally range from tens of nanometers to some micrometers.

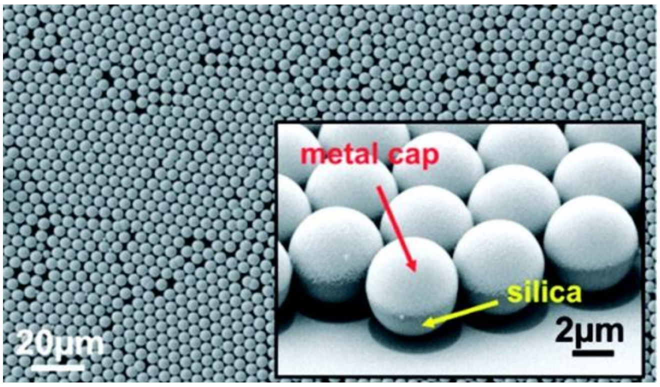

Figure 1.21 SEM image revealing an array of self-assembled spherical particles (5 µm in diameter). The inset shows the coating of the Janus particles with metal film[125]

Glancing angle deposition (GLAD) is a physical vapour deposition technique where the vapour is deposited onto a substrate at grazing incidence. This technology was introduced by Fischer to fabricate magnetic helical nanoswimmers (Figure 1.22).[126] Due to the critical importance of the size, shape, and uniformity of the seeds in fabricating helical structures with good homogeneity at large scale, arrays of ordered seeds must be carefully prepared on the substrate before the GLAD process.[127] A monolayer of the spherical seeds (e.g. silica beads, Au nanoparticles, and polystyrene beads) was assembled on a Si wafer. After that, the growth of silica helices could be achieved by computer-controlled rotation of a tilted substrate stage during deposition. The dimensions of the helices strongly depended on the seed size. Au nanoparticle seeds produced by micelle nanolithography were employed to prepare helical nanomotors with filament diameter of 70 nm and length of 400 nm.[128]

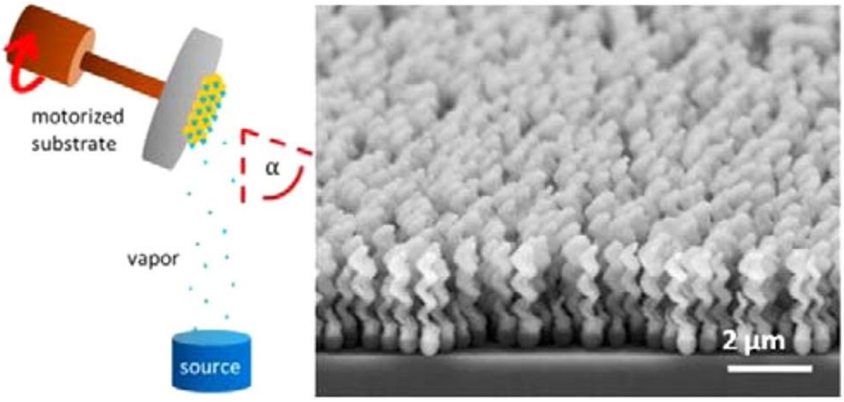

Figure 1.22 Schematic diagram of GLAD technique and SEM image of the helices fabricated using this method.[126]

1.6.3 STRAIN ENGINEERING

Strain engineering provides a powerful tool for transforming nanosheets into three-dimensional micro/nanostructures, such as wrinkles, tubes, and helices. By applying an engineered strain gradient in the deposited thin films, the films can bend into desired structures as long as it is released from the substrate. Various materials can be used for this fabrication method, employing proper deposition techniques and specific etchants to remove the temporal sacrificial layer underneath. Strain engineering has been widely used in the fabrication of tubular and helical micro-/nanomotors.

The so-called rolled-up nanotechnology developed by Schmidt and co-workers is one of the main techniques to fabricate tubular micro-/nanomotors.[129] It utilizes strain engineering to prepare micro-/nanotubes from deposited films.[130] Typically, a pre-stressed metal nanomembrane is deposited on a photoresist sacrificial layer patterned by photolithography, which will be selectively removed by acetone afterwards. Tilted deposition is used to create shadowed window, where the materials are not deposited on the sacrificial layer. This shadowed window will then allow the selective etching of the sacrificial layer from one side of the pattern. Precise control of substrate temperature and deposition rate creates the strain gradient which is needed for the subsequent rolling process. As shown in Figure 1.23, the deposited nanomembrane bends and rolls into a microtube as long as it is released from the substrate by removing the sacrificial layer. The fabricated microtubes are dried by critical point dryer to avoid collapse of the rolled-up devices. The lengths of such microtubes can be in the range of several micrometers, which is determined by photolithography. Microtubes with various diameters ranging from 1 to 60 µm can be fabricated by changing the thickness and the internal strain of the nanomembranes.[131] The rolling orientation of the membrane is determined by the crystal structure of the sacrificial layer as well as the different etching rates along the crystal axis.[132]

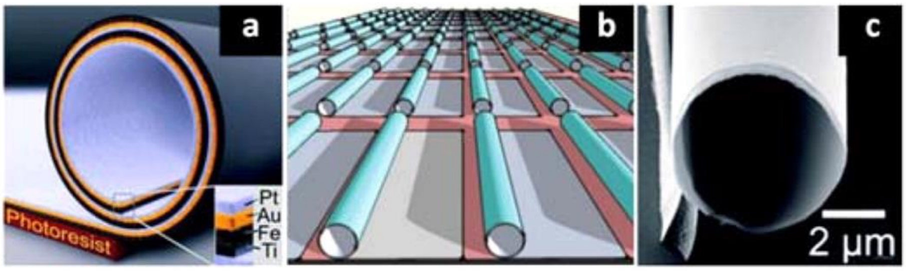

Figure 1.23 Rolling-up of nanomembranes patterned with photoresist: (a, b) schematic diagram of a rolled-up microtube consisting of Pt/Au/Fe/Ti multilayers on a photoresist sacrificial layer and an array of rolled-up microtubes, (c) SEM image of a rolled-up microtube.[133]

Taking the advantage of the strain in thin layers, a ribbon can scroll into a helix. Self-scrolling technology depends on the strain in thin films similar to rolled-up nanotechnology. The straight ribbon can scroll into a helix structure, which provides the desired magnetic propulsion as discussed in section 1.4.3. (see Figure 1.24). Nelson and co-workers applied this technology to fabricate a magnetically powered artificial bacterial flagellum (ABF), which consisted of two parts: a helical tail and a soft-magnetic metal head.[89] The helical tail is fabricated based on thin-film deposition. The soft-magnetic head is simply prepared by e-beam evaporation of Cr/Ni/Au thin films and a lift-off process. Finally, 2D patterned films self-organize to form an ABF by selectively etching the AlGaAs sacrificial layer underneath.[134]

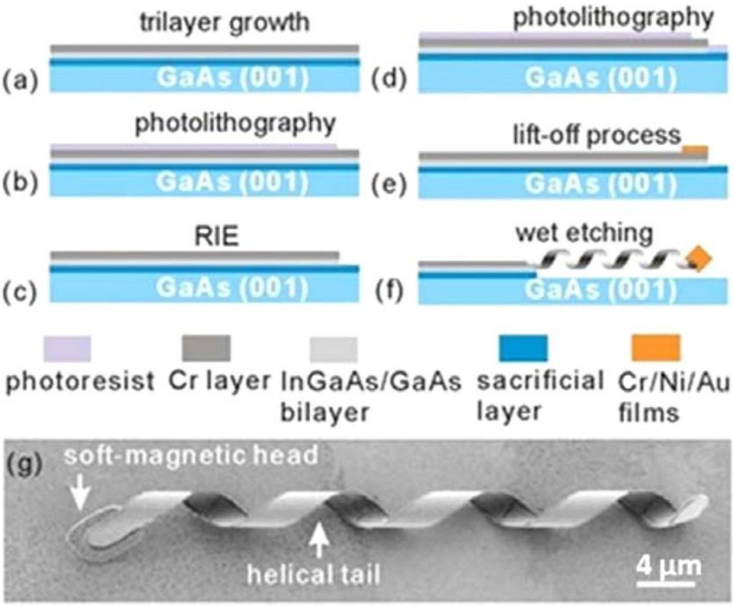

Figure 1.24 (a-f) Fabrication procedures of helical micromotors using self-scrolling technique. (g) SEM image of a self-scrolled helical structure.[134]

1.6.4 THREE-DIMENSIONAL DIRECT LASER WRITING

The recent significant progress in three-dimensional direct laser writing (3D DLW) has made it an adaptable and standard tool for precise fabrication of arbitrary 3D structures in micro- and nanoscale with high resolution. In this method, a photoresist is deposited on a substrate that can be moved with a piezoelectric stage in 3D following a pre-programmed path to partially expose the photoresist to the focal point of the laser.[135]

This technology has been used to fabricate magnetic helical micromotors by Tottori et al., as illustrated in Figure 1.25.[136] The fabrication process included three steps: i) the patterned structure was written by focused beams via two-photon polymerization; ii) helical polymer structures were obtained after removal of the unpolymerized photoresist; iii) magnetic thin layers such as Ni or Co and Ti layers were deposited by e-beam evaporation over the helical structure.

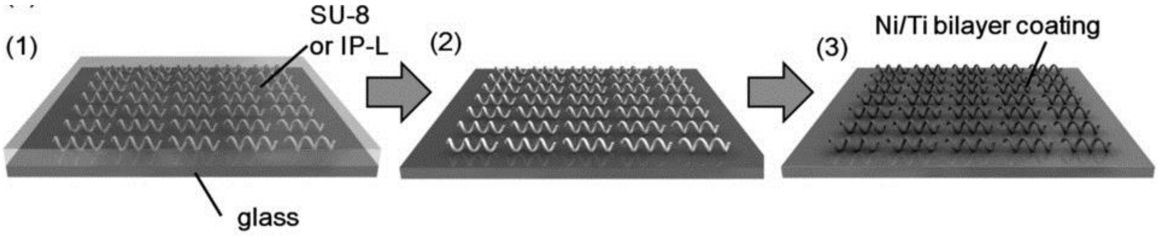

Figure 1.25 Fabrication procedure of helical swimming micromachines.[136]

Apart from helical structures, the precious control of direct laser writing over the geometry of the samples makes it possible to fabricate various complex micro-/nanomotors. Nelson and co-workers demonstrated the preparation of a three-dimensional microscale porous scaffold as a carrier for multiple cells (Figure 1.26).[137]

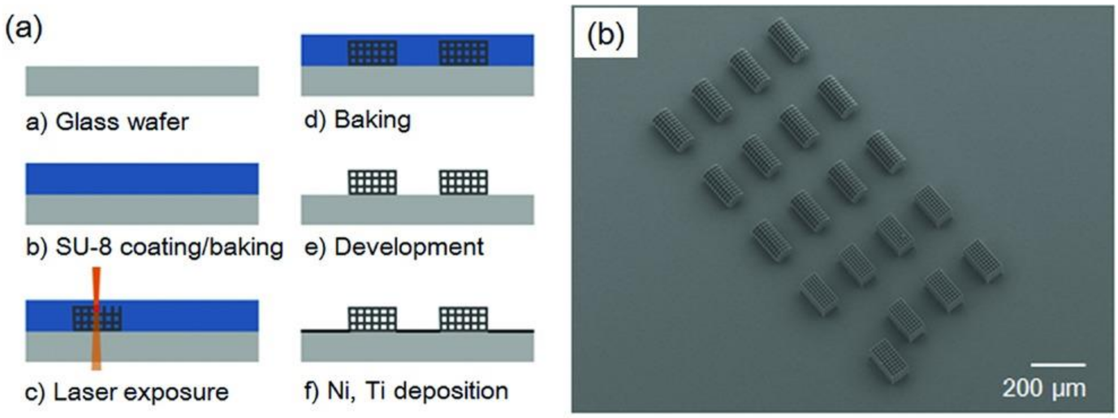

Figure 1.26 (a) Overview of the micro robot fabrication process. (b) SEM image of the fabricated microrobots.[137]

1.7 APPLICATIONS OF MICRO-/NANOMOTORS

The wide range of potential applications of micro-/nanomotors covering different fields needs specific functionalization strategies for different applications. In this section, two main types of applications for micro-/nanomotors are presented: environmental remediation and biomedical applications.

1.7.1 MICRO-/NANOMOTORS FOR CONTAMINANT REMOVAL

One of the main goals within this work is to apply the self-propelled micro-/nanomotors for cleaning contaminated waters. The removal and destruction of pollutants in water is a major concern of environmental sustainability.[138] Nano-remediation related strategies imply the application of reactive nanomaterials for transformation and detoxification of pollutants toward purifying the water resources.[139] Synthetic micro-/nanomotors, which are designed to convert energy from different sources into motion, offer distinct advantages for potential applications to reduce the clean-up time and overall clean-up costs. These novel self-propelling motors can provide efficient self-mixing of a contaminated solution that significantly speeds up clean-up process to remove pollutants such as oil droplets, heavy metals, and other organic compounds in water. Two major mechanisms are reported to purify polluted water with the help of micro-/nanomotors: pollutant adsorption and/or pollutant degradation.[140]

Persistent organic pollutants (POPs) are organic compounds that are rather resistant to environmental degradation.[141] They tend to bioaccumulate in the living tissues of species high up in the food chain, posing a risk to human health and wildlife.[142] For POPs removal, as mentioned above, there are two main methods: adsorption and/or degradation. In the case of pollutant adsorption, Orozco et al. reported Janus micromotors with reduced graphene oxide (rGO) for the efficient removal of POPs, using 5-chloro-2-(2,4-dichlorophenoxy) phenol (triclosan) and polybrominated diphenyl ethers (PBDEs) as examples.[143] These Janus micromotors consisted of a SiO_2-rGO core shell half covered by a catalytic Pt layer. The adsorption of organic contaminants effectively took place at the rGO surface rapidly, at the same time the Pt side efficiently self-propeled the micromotors in a polluted solution with the help of the H_2O_2 fuel. The synergistic effect of the micromotor motion, enhanced adsorbate/adsorbent interactions, and higher adsorbent properties of the rGO, led to the improved ~90% removal efficiency for POPs in only 10 min.[143] S.Sanchez et al. also used a graphene oxide micromotor for heavy metal removal consisting of nanosized multilayers of graphene oxide, Ni and Pt. The motors were able to remove Pb to below 50 ppb in less than 60 minutes.[144]

In addition to the adsorption mechanism, researchers also developed micro-/nanommotors that employ the degradation mechanism to remove organic pollutants in water. Several strategies have been reported, which include H_2O_2-assisted and photocatalysis

1.7.1.1 H_2O_2 FUEL-ASSISTED

The decomposition of hydrogen peroxide into water and oxygen can be utilized to power a motor. It should also be noted that H_2O_2 itself is a strong oxidizing agent which has been already used to degrade organic compounds.[145] Based on these facts, Wang's group developed a polymer-based microtubular motor in the presence of low concentrated H_2O_2 acting as oxidant and motor fuel. This motor degraded organophosphate pesticides such as methyl ethyl paraoxon, paraoxon, and bis(4-nitrophenyl) phosphate through the in situ generation of OOH^- nucleophiles in presence of a peroxide activator (NaHCO3) .[146]

Another efficient option for the degradation of organic pollutants is the Fenton method, one of the most popular advanced oxidation processes (AOPs).[147] Generally the Fenton reactions make use of a powerful oxidant the hydroxyl radical ($^{\cdot}OH$) as their main oxidizing agent. The generation of $^{\cdot}OH$ in the Fenton method occurs by reaction of H_2O_2 in the presence of Fe(II).[148]

$$Fe^{2+} + H_2O_2 \rightarrow Fe^{3+} + OH^- + \ {}^{\cdot}OH$$
$$Fe^{3+} + H_2O_2 \rightarrow Fe^{2+} + HOO^{\cdot} + H^+$$

Taking the advantage of the Fenton process, Sanchez's group reported a catalytically Fe/Pt-based roll-up micromotor to remove organic pollutants, employing Rhodamine 6G as a model pollutant.[149] On one hand, the outer Fe layer for the in-situ production of Fe^{2+} ions during Fenton oxidation process boosted the decontamination process. On the other hand, the inner Pt layer drove the motor. The improved mixing and release of iron ions facilitated by these self-propelling motors resulted in the removal of Rhodamine 6G with an efficiency 12 times higher than when the Fenton reaction was carried out with non-propelling Fe rolled-up tubes. They also found that Fe/Pt microswimmers showed long term reusability. Even longer-term storage for several weeks was possible without sacrificing much of the activity.[150] The same group also fabricated cost-effective and template free micromotors based on cobalt ferrite particles which acted as the catalyst for propulsion and for Fenton-like reactions. These motors were used to degrade quite efficiently antibiotics from wastewater.[151]

1.7.1.2 PHOTOCATALYTIC

Heterogeneous photocatalysis, another type of AOP similar to the Fenton process, takes place when light is absorbed by a semiconductor such as TiO_2 generating electron-hole pairs. The photo-induced electron–hole pairs then either recombine and release heat or interact with other molecules as describe below: [152]

$$e^- + O_2 \rightarrow {}^{\cdot}O_2^-$$
$${}^{\cdot}O_2^- + 2H^+ + 2e^- \rightarrow H_2O_2$$
$$h^+ + H_2O_{abs} \rightarrow {}^{\cdot}\mathrm{OH} + H^+$$
$$h^+ + OH_{abs}^- \rightarrow {}^{\cdot}\mathrm{OH}$$

The generated $^{\cdot}$OH radicals are powerful oxidizing agents to degrade organic compounds. Taking advantage of photocatalysis, Zhang et al. reported a plasmonic photocatalytic micromotor based on the bubble propulsion mechanism for the photocatalytic degradation of organic pollutants.[153] The photocatalytic micromotor had an asymmetrically functionalized, double sided TiO_2 semi-shell. The outer surface of the hemispherical shell was coated with Au nanoparticles to form the plasmonic metal/semiconductor heterostructure, while the inner surface was speckled with Pt nanoparticles. Such micromotor could be propelled by O_2 bubbles to improve mass transfer using H_2O_2 as fuel. It could degrade various organic pollutants, such as Methylene Blue, Rhodamine B, and Methyl Orange, and even a mixture of 11 organic pollutants. A photocatalytic micromotor activated with UV light was also developed by Li et al. based on TiO_2/Mg which was used to degrade organophosphate nerve agents.[154] Mushtaq et al. designed Bi_2O_3/BiOCl-based hybrid micromotors activated by UV-visible radiation and controlled by an external magnetic field instead of chemical self-propulsion for the efficient removal of Rhodamine B.[155] Moreover, Sanchez and co-workers fabricated a bubble propelled γ-$Fe_2O_3/SiO_2/MnO_x$ motor to remove both organic and heavy metal pollutants. MnO_X acted as catalyst for the decomposition of H_2O_2 to generate O_2 bubbles for the propulsion. The degradation of organic pollutants was accomplished by Fenton-like and photocatalytic reactions catalysed by iron oxide, though MnOx could also contribute to the contaminant degradation via Fenton like reactions.[156]

1.7.2 BIOMEDICAL APPLICATIONS

Micro-/nanomotors are able to provide considerable promise for biomedical applications. Figure 1.27 illustrates important advances of micro-/nanomotors in the biomedical field.

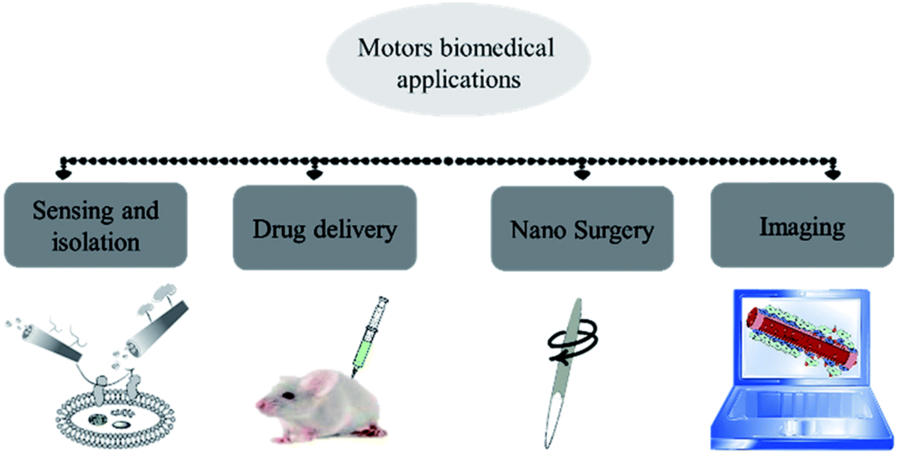

Figure 1.27 Micro/nano-motors for biomedical applications.[157]

Micro-/nanomotors show the potential to sense, capture, transport, penetrate tissues and deliver biomolecules as well as to isolate and separate bioanalytes from complex biological samples. Based on ligand/receptor interactions, micro-/nanomotors capable of capturing “on the fly” and transporting different loads (proteins, nucleic acids, cancer cells, bacteria, etc.), have been reported by several groups.[158] For instance Lectin bioreceptors such as ConA functionalised onto microengines containing gold/nickel/polyaniline/platinum as catalysts were shown to be very efficient in recognizing and isolating E. coli bacteria, known to express polysaccharides on the cell surface.[159] This represented a very promising nanomotor strategy for isolating pathogenic bacteria with impact not only in the clinical applications but also in environmental, food safety and biodefense applications. Different nanomotors have been investigated for their capabilities to transport cargoes, including drug carriers such as liposomes or microspheres and drugs themselves.[160] Catalytic nanomotors employing alloys of Ni/(Au_{50}/Ag_{50})/Ni/Pt were used to transport doxorubicin-loaded magnetic PLA microspheres and magnetic liposomes via ferromagnetic interaction between nickel segment of the nanowire motor and iron oxide entrapped inside the microparticle.[161] At the same time, Sen et al. described the transport of positively charged polystyrene microspheres linked to Pt–Au nanomotors through electrostatic interactions.[162]

Different mechanisms have been studied to release cargo at specific locations by drag forces, pH, diffusion, ultrasound or light. The cargo release by drag forces was possible by a fast reversal of the nanomotors' motion direction with an external magnet whereby the drag force imposed on the cargo overcame the magnetic attraction between the cargo and the motor.[163,164] An example of cargo release by pH changes is represented in calcium carbonate based motors loaded with coagulation factors which were conceived to serve as effective hemostatic agents to regulate blood coagulation.[165] Cargo release by diffusion has been shown in urease-powered nanomotors using mesoporous silica particles. Anticancer drugs have been loaded into the mesoporous template and then released in HeLa cells by diffusion.[166] Fast cell penetration and selective delivery of siRNA was also demonstrated by using an acoustically propelled nanowire motor for gene therapy.[167] An example of cargo release by light was reported with hollow Janus particles containing Au nanoparticles and catalase for the catalytic propulsion. The system was loaded with anticancer drug which was released via near infrared (NIR) light activation, inducing breakage of the polymeric shell upon local heating of the embedded Au nanoparticles through the photothermal effect.[168] The potential of these machines to transport and deliver therapeutical payloads directly to disease sites holds promise for improving the therapeutics efficacy and reducing systemic side effects of highly toxic drugs.

The multiple tasks performed by autonomously moving functionalized micromotors holds considerable promise for lab-on-a-chip (LOC) applications, including separation, purification, enrichment and/or sorting. The integration of micro/nanomotors and microfluidics can bring about powerful on-chip microsystems powered by autonomous transport.[169] Under this context it has already reported a fast micromotor based LOC immunoassay in which the targets were isolated from raw complex media by capturing and transporting them to a clean environment reservoir of a LOC and thus avoiding laborious sample preparation steps typical in standard immunoassays.[170]

For the application toward minimally invasive surgery, particular attention was given to magnetic microdrillers and rolled-up nanojets that were able to enter into biomaterials in the presence of an external magnetic field or fuel.[171] The Schmidt group reported that InGaAs/GaAs/(Cr)Pt microjets with sharp tips demonstrated a corkscrew-like movement in the presence of hydrogen peroxide, allowing them to drill into fixed HeLa cells. However, the fuel used to propel the microjet is toxic in biological systems, thereby limiting its in-vivo application. The same group further developed Ti/Cr/Fe microtubes controlled by external magnetic field to explore the possibility of performing drilling operations.[172] Ultrasound actuation has been also used to create powerful bullet-like microrobots with remarkable tissue deep penetration and also capabilities to induce tissue ablation and destruction.[173]

Micro-/nanomotors are becoming a new class of promising agents for medical imaging to probe physiological or pathological conditions. Tissues can be differentiated and imaged based on the unique sensitivity of micro- and nanomotor to pathological factors such as hydrogen peroxide, temperature and water content. [174] Mattrey et al. reported the application of catalase-coated silica nanosphere converters (NSCs) for micro-bubble based ultrasound imaging. NSC particles produced a detectable increased signal when injected in the vicinity of a bacterial abscess since they were able to break down inflammation associated with H_2O_2 to O_2 micro-bubbles.[175]

Tremendous progress has been achieved in demonstrating the in-vitro capabilities of micro-/nanomotors for theranostics and imaging, but huge efforts are still needed to translate the proof-of –concept research to in-vivo applications. Motor navigation in blood is very challenging due to its complex and viscous character which implies the use of powerful motors which capabilities to move against fluid flows and in high ionic media. Several additional hurdles remain before practical in vivo applications of motors become a reality. The finding of novel types of biocompatible chemical fuels (e.g. molecules present in the body fluids such as glucose), the synergetic combination of differently propulsion mechanisms in the same motor (e.g. chemo-acoustic hybrid nanomotors) and the use of biocompatible (e.g. enzyme as catalysts) and biodegradable materials could minimize the concerns in in-vivo biomedical applications. Moreover, stringent examination of its toxicity should be assessed before clinical translation. Despite all the obstacles to overcome, it seems that the first steps towards the realization of real in vivo applications are being taken. For instance, J. Wang and co-workers have recently presented the first in-vivo therapeutic micromotor application for active drug delivery to treat gastric bacterial infection using a mouse model. The propulsion of antibiotic-loaded magnesium micromotors in gastric media enabled effective antibiotic delivery, leading to significant bacteria decrease in the mouse stomach compared with passive drug carriers, with no apparent toxicity.[176] This work opens the door for in-vivo therapeutics applications of body-fluid propelled micromotors towards the treatment of a variety of diseases and disorders.

1.8 THESIS MOTIVATION AND OBJECTIVES

As described in the previous section of silicon/metal micropumps, the Si/metal pump can be controlled by visible light through a light-activated catalytic reaction process. It has been demonstrated that the pumping speed of fluid can be fine-tuned with visible light intensity. On the other hand, most of the proposed photoactive micro/nanosystems are actuated with UV light, which is a hurdle for specific applications such as biomedicine. Therefore, it is very desirable to find motors that can be operative with cost-effective and more innocuous light sources such as the ones in the visible range and, even more attractive, in the near IR one, being the latter very promising for biomedical application due to large tissue penetration depth.

Under this context, the goal of this thesis is to develop bubble-free silicon/metal autonomous nanomotors, driven by catalytic reactions activated by visible light and with the capability that the direction of the motion can be steered by an external magnetic field through the incorporation of an extra ferromagnetic segment into the system. The actuation mechanism of these nanomotors will further assessed through their performance as photocatalytic agents for pollutant removal in water, paying special attention on their capabilities for generation of reactive oxygen species.

1.9 THESIS OUTLINE

In chapter 2, we present the experimental results of Si/Pt nanomotors, which are fabricated by two metal deposition methods. Their propulsion behaviours in the presence of hydrogen peroxide are reported together with their contaminant removal performance as an additional way to give insights on the propulsion mechanism. In chapter 3, we discuss different behaviours of Si/Pt pumps fabricated with both smooth and rough Pt to better understand the propulsion mechanisms of Si/Pt nanomotor counterparts. Two different chemo-mechanical pumping mechanisms behind the Si/Pt pump systems are proposed, which are mainly governed by surface roughness of metal layer. Chapter 4 summarizes all the experimental results from X-ray photoelectron spectroscopy used to probe the Si/Pt interface under ultra-high vacuum and near ambient pressure in order to study the chemical pathways that can be generated at the Si/Pt interface in contact with water, for a better understanding of the (photo)chemomechanical mechanisms in Si/Pt system. Chapter 5 illustrates a silicon based motor that can be successfully controlled by visible light, which has helped us to establish the guidelines to develop optimized photoactivated motors in future. The improvement of the efficiency for contaminant removal is also demonstrated by introducing zero-valent iron element. In Chapter 6 we list the main conclusions and perspectives for autonomous micro-/nanomotor systems. As an appendix, chapter 7 provides in detail the relevant materials as well as the methods for device fabrication and characterization.

2 SI/PT NANOMOTORS: PROPULSION ANALYSIS AND CONTAMINANT REMOVAL.

2.1 INTRODUCTION

In the previous work of our group on silicon based micropumps[177], it was reported that a highly efficient pump consisting of noble metal and doped silicon could be controlled with visible light. The actuation was based on electro-osmosis with the electric field generated by the chemical reactions at the metal and silicon surfaces, whereas the contribution of diffusio-osmosis to the actuation was negligible. The electro-hydrodynamic process was just triggered with only water but it was greatly amplified with the addition of reactive species, such as hydrogen peroxide, which generated higher electric fields. Another remarkable finding was the tunability of silicon-based pumps. Thus, it was possible to control the speed of the fluid with light intensity.

Based on these findings, this thesis project initially proposed a silicon based nanomotor (Figure 2.1), which consisted of a silicon nanowire and a noble metal cap layer. In such a scenario, the silicon based nanomotor, similar to the micropump, could be self-propelled by electro-phoresis with the electric field generated by photoacativated chemical reactions at the metal and silicon surface. Under light illumination, electrons would be excited from the valence band to the conduction band of silicon and then transferred to the metal. The holes generated at the semiconductor would become oxidizing agents for the fluid or for the silicon itself whereas the injection of electrons at the metal counterpart would make it act as reducing agent. Thus, in this proposed model, the control of the propulsion speed of the nanomotor could be managed by varying the intensity of visible light and the motor direction could be steered by external magnetic field with ferromagnetic material incorporated into the Si/Pt motor. In addition, it was intended to assess the capabilities of the proposed motor to produce reactive oxygen species through the photocatalytic process to promote an enhanced removal of organic pollutants in water, a very relevant issue from the fundamental point of view and for the applications.

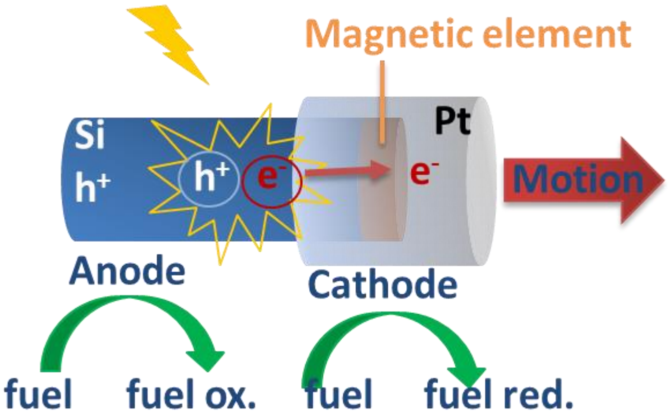

Figure 2.1 schematic of proposed Si/Pt nanomotor.

The photoactivated chemical pathways at Si/Pt systems can be very complex. Proton production at Si and proton consumption at Pt was observed on Si/Pt micropumps. Such finding is compatible with the following chemical pathways:

$$Anode\ (Si): H_2O_2 \rightarrow 2H^+ + O_2 + 2e^-$$
$$Cathode\ (Pt): H_2O_2 + 2H^+ + 2e^- \rightarrow 2H_2O$$

$$Anode\ (Si): Si + H_2O_2 \rightarrow 2H^+ + SiO_2 + 2e^-$$
$$Cathode\ (Pt): H_2O_2 + 2H^+ + 2e^- \rightarrow 2H_2O$$

However, additional chemical pathways yielding to the production of reactive oxygen species ($^\bullet OH$, $^\bullet O^-_2$, $^1O_2$) could also take place which could be harnessed to promote an enhanced removal of organic pollutants in water. For instance, $^\bullet OH$ can be easily produced by the hydrogen peroxide reduction at the cathode. Accordingly, in this chapter, the Si/Pt nanomotor in the presence of hydrogen peroxide solution is investigated to understand the propulsion behaviour and the corresponding driving mechanism, and to grasp clues of the plausible chemical pathways.

The results of the experiments on two different types of silicon nanomotors with electron beam evaporated or sputtered Pt cap layers in various conditions are presented. In addition, the contaminant removal test is carried out to further examine the reaction pathways and the potential application of Si/Pt nanomotors to decompose organic contaminants in water.

2.2 FABRICATION AND GEOMETRICAL CHARACTERIZATION OF SI/PT NANOMOTORS

The proposed novel motor consisted of silicon nanowire and platinum cap layer. The silicon nanowire (Si NW) was fabricated using colloidal lithography followed by metal-assisted chemical etching (MACE). The detailed process of the fabrication was described in materials and methods section of the Appendix.. This facile and low cost chemical method enabled us fabricating arrays of silicon nanowires in the 4-inch wafer scale.

The platinum cap layer was later deposited by two different methods, e-beam evaporation and sputtering in grazing angle, to achieve different coverage areas of platinum layer to evaluate their impact on the nanomotor propulsion. In the case of electron beam evaporation, the deposition was carried out with the sample strictly perpendicular to platinum source and, therefore, only the top of silicon nanowire array was covered by Pt due to the directional flux of Pt. In contrast, the sample is positioned in grazing angle for sputtering, thereby yielding a partial coverage of the side walls as well as the top of the nanowire due to the less directional sputtered Pt flux.

The Si/Pt nanomotors were 1µm in length and 200nm in diameter and the thickness of deposited platinum cap layer was 40nm in both cases. It can be seen that the e-beam evaporated Pt layer is more condensed on the top of the nanowire with respect to the sputtered one from the SEM images in figure 2.2. This was due to the different configurations of the two deposition systems.

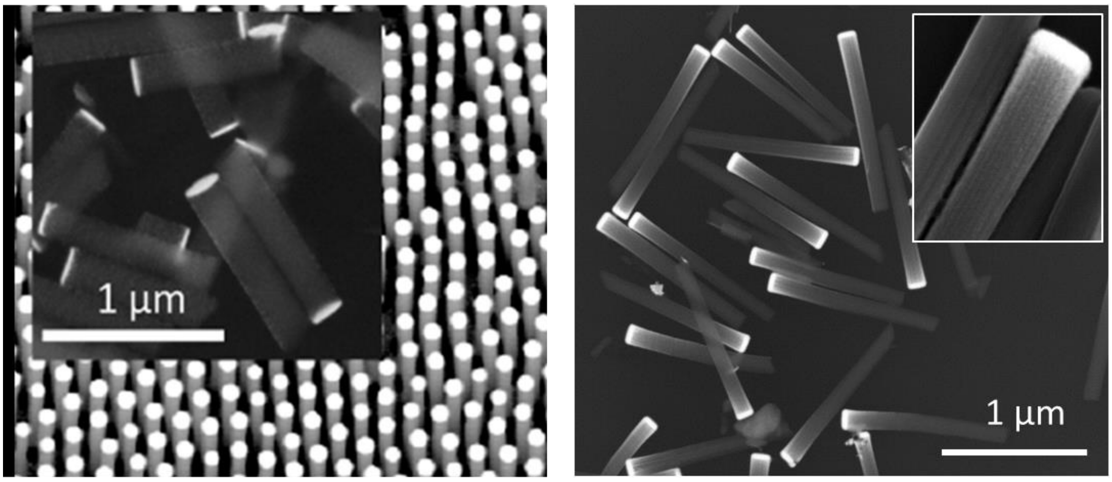

Figure 2.2 SEM images of the e-beam evaporated and sputtered Si/Pt nanomotors. Left: evaporated platinum sample array with inset of suspended silicon nanomotors. Right: sputtered platinum silicon nanomotors after suspension with inset of the zoom-in view of top platinum layer.

2.3 OPTICAL PROPERTIES

Silicon is a high refractive index material. Therefore, silicon nanostructures can exhibit multipolar Mie optical resonances in the visible and near infra-red (NIR) parts of the spectrum, which lead to strong field enhancement inside the nanostructures.[178] These optical resonances can be tuned with the size and shape of the nanostructures.[179] This enhanced light/silicon interaction can make Si nanowires good candidates for efficient visible/NIR light activated micro-/nanomotor.

Figure 2.3 compares UV–Vis absorption spectra ranging from 400nm to 900nm of suspended silicon NWs with and without sputtered Pt cap layer (10^{-9}/L) in water. A significant absorption peak can be observed at 425nm in both spectra and a very broad absorbance in the visible and NIR. Due to the random orientation of SiNWs in water, the recorded spectrum corresponds to the convolution of the resonances at the different orientations of the nanowires. The larger absorbance in the Pt coated nanowires is due to the increase absorption of the nanostructured Pt layer.

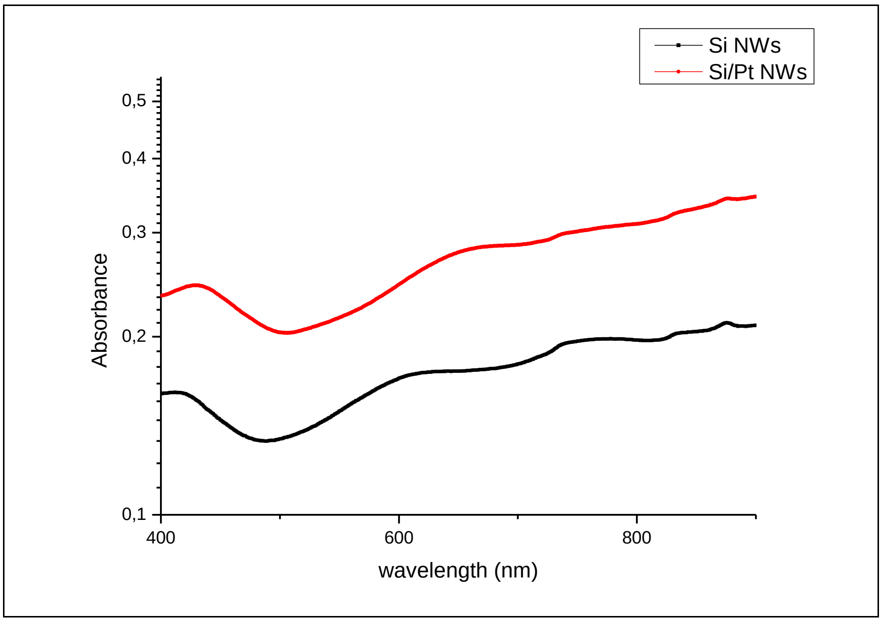

Figure 2.3 UV–vis absorption spectra of the silicon NWs and SiNWs with sputtered Pt cap layer at room temperature.

2.4 PROPULSION ANALYSIS

The propulsion behaviour of these two types of Si/Pt nanomotor were investigated in a 1%wt H_2O_2 solution at different wavelengths and intensities (see details in Appendix) and monochromatic laser sources in scanning mode. The detailed results are presented below. The motion of such motors was tracked with the help of software Imaris.

The sputtered Si/Pt nanomotor showed significant directional motion reaching maximum speeds of 31 µm/s, while scarce motion was captured for the e-beam evaporated samples. Figure 2.4 shows the tracking trajectories of the Si/Pt nanomotors under red scanning laser at wavelength of 633nm in the presence of 1%wt H_2O_2.

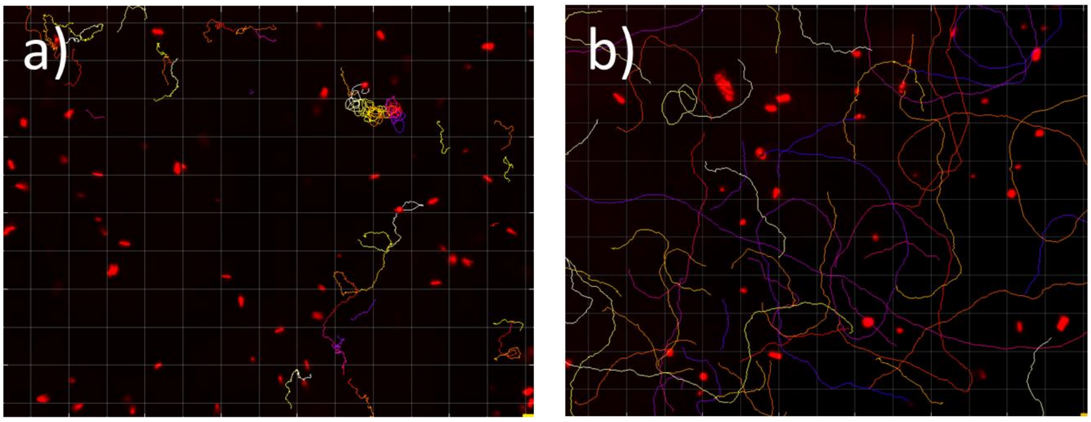

Figure 2.4 tracking trajectories of Si/Pt nanomotors under scannning red laser at wavelength of 633nm in the presence of 1%wt H_2O_2. a) evaporated Si/Pt nanomotor. b) sputtered Si/Pt nanomotor.

Given the poor movement recorded in the case of the Si/Pt motors evaporated with electron beam, we focused on the propulsion mechanism of the swimmers with sputtered Pt especially addressing the light effects. We first analysed the spectral dependence of the propulsion speed of sputtered Si/Pt nanomotor. The mean velocity of sputtered Si/Pt nanomotor, extracted from the trajectory measurements, as a function of different light wavelengths is shown in figure 2.5. The variation of the mean velocity with wavelength increasing from 488nm to 633nm was not very significant, which suggested that the light wavelength did not play an essential role in the propulsion of the sputtered Si/Pt nanomotor.

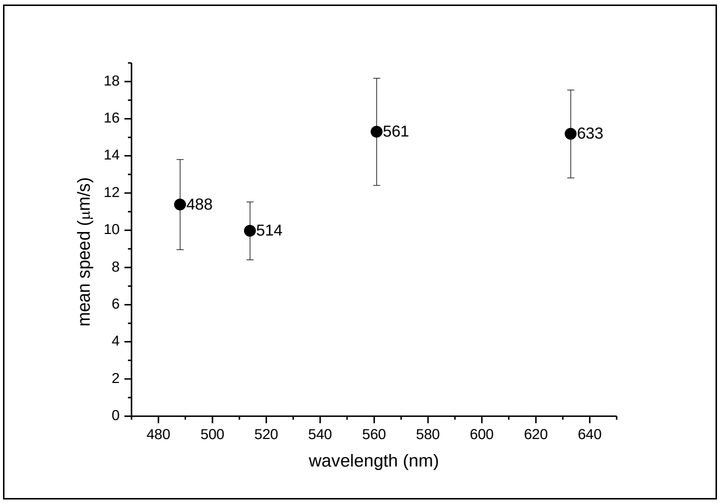

Figure 2.5 the mean velocity of sputtered Si/Pt nanomotor as a function of light wavelengths (nm) at 100% light intensity.

Another experiment was designed to check both the effects of light intensity and the contribution of electron generation at the Si part and subsequent electron transfer to the Pt part on the overall propulsion. A Si/SiO_2/Pt nanomotor was developed as comparison, which was obtained by thermally oxidizing the silicon nanowire and by sputtering the Pt cap layer as shown in the inset of figure 2.6. The thermal oxide thickness was about 100 nm, which is sufficient to block the electron transfer route between Si core and Pt cap.

When the light intensity was increased from 0% to 100%, there was an insignificant difference of average speed in both Si/Pt and Si/SiO_2/Pt cases. In addition, The Si/Pt nanomotor exhibited roughly 30% higher mean velocity than the corresponding Si/SiO_2/Pt motor at the wavelength of 633nm in the presence of 1%wt H_2O_2 as shown in figure 2.6. Such small drop in velocity when blocking electron transfer could indicate another chemical pathway in the propulsion process and hence another mechanism competing with the electrophoresis. It could mean that there was an important contribution of diffusiophoresis engaging the motor propulsion. The lack of light intensity sensitivity on the motor velocities would also suggest that the photogenerated electron hole pairs and the subsequent separately redox reactions at Si and Pt parts do not make major contribution to the propulsion process, unlike the previously observed effects in Si/Pt pumps.

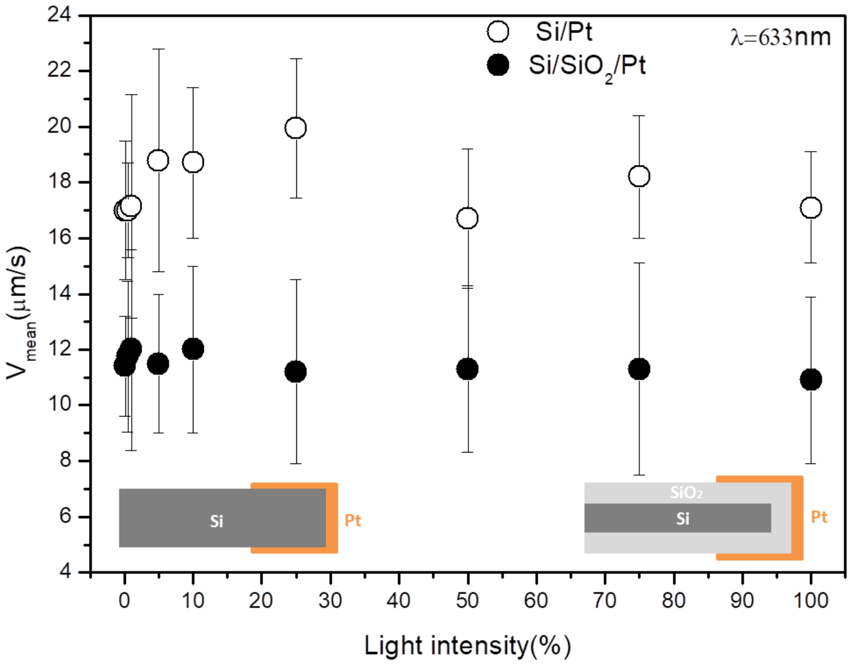

Figure 2.6 mean velocity of Si/Pt nanomotor and Si/SiO_2/Pt nanomotor with increasing light intensities for 0 to 100% under red pulsed laser at wavelength of 633nm in the presence of 1%wt H_2O_2.

In order to further investigate the possible mechanisms behind the propulsion, we also studied the effect of adding salt to the hydrogen peroxide solution. We found a remarkable decrease of the directional motion in the case of sputtered Si/Pt nanomotor when adding 0.5M KCl to 1% H_2O_2. An electric field screening effect is expected for a self-electrophoresis mechanism. However, a reduction of the propulsion speed has been also reported in motors which are expected to be driven by neutral diffusiophoresis in which no electric fields are built-up (e.g., Janus particles with half segment made of an insulating material and the other one made of a metal catalyst immersed in H_2O_2 solutions). The origin of salt effect in such diffusiophoretic systems is not well understood and is under debate. Some studies with such systems suggested the presence of ionic effects that could be affected by salts and were attributed to different sources. It was proposed that asymmetries in the metal catalyst, such as different metal thicknesses, could yield to reactions involving charged intermediates. Other studies suggested the potential dissociation of H_2O_2 and water in ions at the metal surface and in the bulk solution as additional sources for ionic effects. Moreover, it is also known some salts, especially the ones based on chloride, a specific adsorption of chloride anion on the metal surface can take place decreasing the chemical reaction rates at the catalyst and hence decreasing the chemomechanical actuation.

2.5 CONTAMINANT REMOVAL TEST TO ASSESS REACTION PATHWAYS

We carried out contaminant removal tests to probe the possible chemical pathways of the sputtered Si/Pt nanomotor propulsion. In the case of photocatalytic micromotor, the H_2O_2 redox reactions can enhance organic waste degradation process by introducing reactive oxygen species (ROS) under light illumination. As the sputtered Si/Pt nanomotor exhibits significant directional motion in the presence of hydrogen peroxide, the experiment was implemented to check whether it could enhance organic waste degradation process by ROS generation. Within this work, a mixture of benzene, toluene, and xylene (BTX, 5ppm in each) was used as reference system to evaluate the performance of silicon based motors for organic waste degradation in water. The residual BTX was measured by gas chromatography with flame ionization detector (GC-FID) technique after adding Si/Pt nanowires overnight.

Due to the high volatility and poor aqueous solubility of BTX, the mixed solutions were prepared by a two-step procedure starting with a much diluted mother solution of BTX. Firstly a 9 ppm BTX+1.76% H_2O_2 was prepared in a 2 litre volumetric flask in an ice bath. Then the solution was diluted into 5 ppm of BTX and 1% H_2O_2 in an 8 ml tube glass bottle together with the Si/Pt rods without having gas phase space. The exposure time to the air was minimised as short as possible to avoid the volatilization of BTX and the bottles were always open under refrigeration.

The results from GC-FID measurement of BTX samples after different treatments for 17 hours overnight were shown in figure 2.7 below. Sample 1 and 2 were reference BTX solutions with 1%wt H2O2 without nanomotors which were stored in fridge overnight without and with stirring. Sample 3 contained 1% H2O2, BTX and the nanomotors under stirring but without being exposed to light. Sample 4 contained the nanomotors plus H2O2 and BTX under light irradiation and represents the important sample to assess any ROS generation that could lead to an enhanced BTX degradation.

The residual amount of BTX in sample 3 and 4 with sputtered Si/Pt nanomotors was much higher than the BTX amount in reference sample 1 and 2. As H_2O_2 is an oxidizing agent for organic compounds degradation[180], it is not surprising that hydrogen peroxide itself can decompose BTX. However, degradation in sample 4 under light illumination was expected to be higher than in samples 1 and 2. The high amount of BTX in sample 4 is indicates that the Si/Pt wires clearly decompose H2O2 but not mainly through a photochemical pathway leading to ROS production. Even so, a slight decrease in BTX amount can be captured in sample 4 when comparing with sample 3 which could be ascribed to a very small ROS generation under light illumination. Therefore, the Si/Pt wires seem to promote more the immediate hydrogen peroxide decomposition to water and oxygen at platinum surface as soon as it is added to the solution. Thus, H_2O_2 is exhausted by the preferential reaction with the platinum surface before it reacts with BTX. These findings indicate that the chemical reaction pathway preferentially takes place at the platinum surface of the motor (direct H_2O_2 decomposition on Pt) without the major participation of the light activated silicon and, therefore, minimizing any ROS production through a photocatalytic effect.

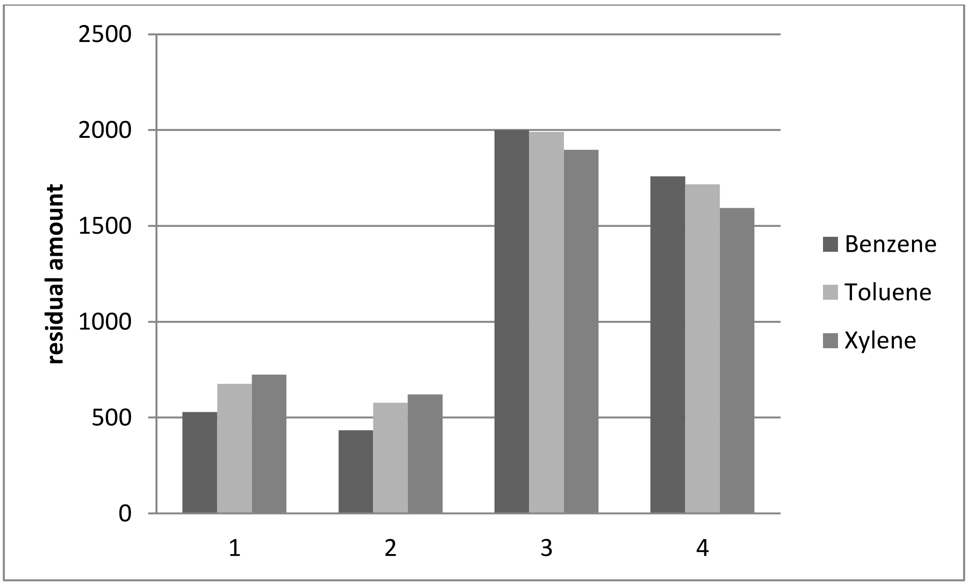

Figure 2.7 The residual amounts of benzene, toluene, and xylene after different treatments overnight.

1. BTX solution with 1%wt H_2O_2 stored in fridge.

2. BTX solution with 1%wt H_2O_2 under stirring with a magnetic bar.

3. BTX solution with 1%wt H_2O_2 and sputtered Si/Pt nanomotors under stirring with a magnetic bar.

4. BTX solution with 1%wt H_2O_2 and sputtered Si/Pt nanomotors under light illumination.

2.6 CONCLUSION

In summary, important directional motion could only be observed from the sputtered Pt nanomotors. However, no significant light effect was observed as a function of light intensity with such motors and only a small decrease in their velocities was recorded when a thick silicon oxide was included between Si and Pt to block the electron transfer between them. These findings pointed out that H_2O_2 decomposition was taken place preferentially at the Pt cap without the mediation of Si. That was also supported by the experiments of BTX degradation, which were carried out to probe the performance of Si/Pt nanomotors as potential promotors of ROS thorough photocatalytic effects mediated by Si and Pt . These experiments also suggested that the main chemical pathway was the direct decomposition of H2O2 mainly at Pt to produce water and oxygen, being the photocatalytic decomposition of H2O2 for ROS generation negligible. The different chemical pathways would dictate the dominant self-propulsion mechanism which seems to be more diffusiophoretic than electrophoretic in this case. Further characterization is needed to identify the key parameters which favour/supress one chemical pathway and mechanism over others. Figure 2.8 demonstrates the dominant decomposition process, which was highlighted in red dot-square.

Given the striking lack of sensitivity of the motion of sputtered Pt/Si swimmers with light, we decided to study the propulsion mechanism of this system in a pump configuration and comparatively with the e-beam evaporated Pt/Si micropump as reported in next chapter.

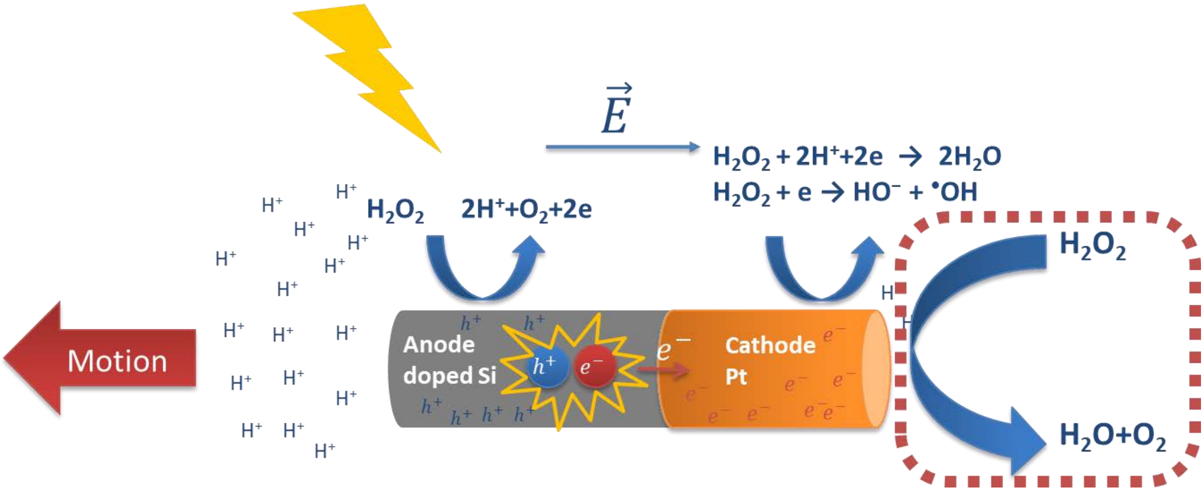

Figure 2.8 schematic of the dominant decomposition process in Si/Pt nanomotor

3 SMOOTH VS. ROUGH PUMPS BEHAVIOUR (UNDERSTANDING OF SI/PT NANOMOTORS)

3.1 INTRODUCTION

In the previous chapter, the evaporated and sputtered Si/Pt nanomotors demonstrated different self-propulsion behaviours in the presence of hydrogen peroxide. More significant directional motions could be observed from the sputtered nanomotors compared to the evaporated ones. However, no significant light effect was observed in both cases.

As proposed in the previous chapter, two possible competitive chemical pathways in fuel decomposition could take place. One pathway is the direct decomposition taking place only at the Pt part, which seems to dominate in the sputtered Pt/Si swimmers. The other possible route is the separated redox reactions at the Si and Pt interfaces respectively, which involves the oxidation of H_2O_2 at the silicon side and the H_2O_2 reduction at the metal side.

To further investigate the propulsion mechanism, we analyze Si/Pt micropumps as the immobilized counterparts of the Si/Pt swimmers. As mentioned before, micropumps constitute ideal platforms for better probing experimental strategies and for acquiring more reliable clues of their actuation mechanisms. In such configuration the fluid moves with respect to the motor surface. Previous studies in our group have already addressed the chemomecanical actuation of Silicon based pumps that could be controlled by visible light.[181] In that case the pump was made from silicon and a metal (Pt, Au) which was deposited by e-beam evaporation. It was argued that light creates electron/hole pairs at the silicon with the subsequent electron transfer to the metal. Such light activated processes induced two separated redox reactions at the motor surface: [181]

i) H_2O_2 mediated oxidation at the semiconductor part,

ii) Reduction at the metal catalyst. The separated reactions gave rise to a proton current from the semiconductor to the metal, thereby building up an electric field, which triggered a fluid flow by electro-osmosis.

In this chapter, we will study Si/Pt pumps with Pt deposited by sputtering and compared with the Si/Pt pumps with Pt deposited by electron-beam evaporation. The different evaporation techniques provide different roughness factors, which will affect the chemical reactions and self-propulsion mechanisms. We will show that it is possible to enhance/suppress the photoactivated and separated H_2O_2 redox reactions and convert them into light insensitive direct electrochemical decomposition of H_2O_2 on Pt. We also demonstrate that the increase of metal roughness triggers a striking change in the flow and generated electric fields, due to the switching of the actuation mechanism from a dominant light-controlled electrokinetic process to a light-insensitive diffusio-osmotic one.

3.2 RESULTS AND DISCUSSIONS

Micropumps were fabricated by patterning Pt discs on p-doped silicon surfaces by using electron beam lithography and platinum evaporation either by sputtering or by electron beam to tune surface roughness. The devices were then subjected to a mild oxygen plasma treatment to clean the surface. Fig. 3.1 illustrates the layouts of the micropumps under study. The figure shows atomic force microscopy images of the Pt part prepared with the different deposition techniques. Devices with sputtered Pt (Fig. 3.1b) exhibit a roughness factor 14 times higher than that obtained through e-beam deposition (Fig. 3.1a).

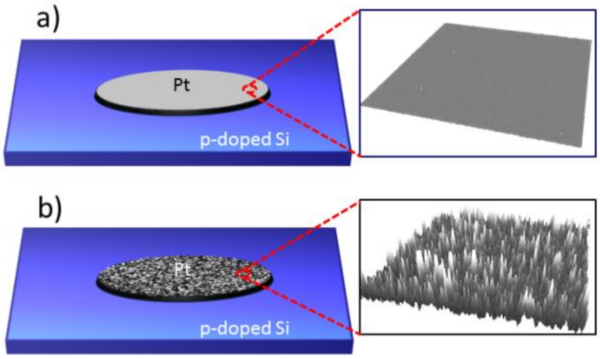

Figure 3.1 Different pump layouts, with (a) smoother e-beam evaporated Pt and with (b) rougher sputtered Pt. AFM images are depicted for both cases taken at the same z scale. Sputtered Pt exhibits a root mean square roughness (Rq) of 5.5±0.3 nm whereas Rq for electron beam deposited Pt is 0.40±0.05 nm

SEM characterization also indicated a higher surface roughness on the sputtered Pt films as can be observed in the SEM images of Fig. 3.2. From now on, we will refer to the micropumps as r-Pt/Si for the rougher sputtered ones, and s-Pt/Si for the smoother e-beam evaporated ones.

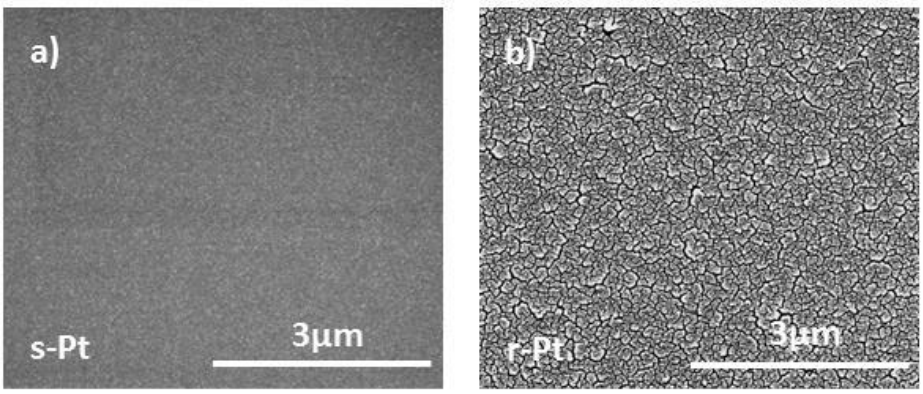

Figure 3.2 SEM images corresponding to the smooth Pt films evaporated by e-beam deposition (a) and to the rough Pt films deposited by sputtering (b). Both images were taken at the same magnification.

The s-Pt/Si devices represent the typical behaviour shown in a previous study performed by the group[181], which pointed out to a photoactivated electrochemical actuation through an electro-osmotic process. According to previous results, the pumping mechanism for s-Pt/Si is illustrated in Fig. 3.3 a and b. The light absorbed in the Si part generates electron-hole pairs. In the vicinity of the Pt disc, the holes oxidize the H_2O_2 at the silicon/fluid interface, and the resulting electrons are transferred to the metal where the reduction of H_2O_2 takes place. During the oxidation reaction, protons are produced at the silicon part, which are consumed at the metal side (b). During this process a proton current is produced that generates an electric field pointing towards the Pt side, thereby dragging the fluid in the same direction. Such fluid motion pointing in the same direction as the electric field is expected for surfaces with negative zeta potentials, as it is in the Si/Pt case.[181]

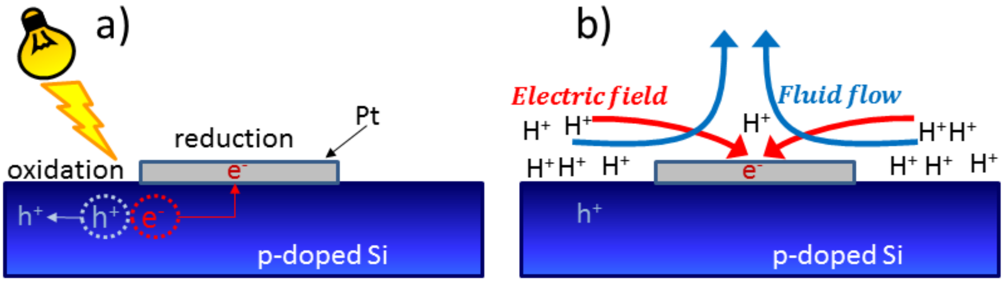

Figure 3.3 a) Schematics illustrating the photochemical activated process with oxidation and reduction taking place at the Si and Pt sides, respectively. b) Schematics depicting the proton generation and proton consumption as a consequence of the light activated redox process together with electric field and fluid flow direction.

The impact of the Pt surface roughness is elucidated by comparing the results of smooth e-beam evaporated and rough sputtered Pt pumps by using 1% H_2O_2 as chemical fuel and at high white light intensity. The fluid motion is followed by tracking the motion of tracer particles of opposite surface charge (zeta potentials of ξ-= -83 mV and ξ+=46 mV for negative and positive colloids, respectively).

Despite of their similar size and Pt thickness, the interaction of positive and negative tracers with the r-Pt/Si and s-Pt/Si devices is strikingly different. In the case of r-Pt/Si, positive tracers exhibit maximum radial component velocities of about -8 µm/s. These particles move towards the Pt part, and after crossing the Pt-Si edge, their trajectory bends upwards in the direction perpendicular to the Pt disc, (see Fig. 3.4a and Movie 3.1). Such a behaviour is totally different to the one previously encountered by using the same positive tracers on smoother s-Pt/Si devices (Fig.3.4 b). In that case the positive tracers move towards the Pt disc at much higher speed (maximum values of -65 µm/s) and stick to it (Movie 3.2). Even stronger differences between rough and smooth systems can be observed for negative tracers. Fig. 3.4c shows the interaction of negative particles with the r-Pt/Si device. Negative tracers move towards the rough Pt disc and they either cross the Pt edges and stick on the Pt surface or they just stick at the rims of the Pt disc (Movie 3.3). This behaviour is surprisingly different to that found for s-Pt/Si motors, in which a repulsion band is generated at the Pt disc, thereby leaving the Pt surface and surrounding Si completely free of negative tracers (Fig. 3.4d, Movie 3.4).

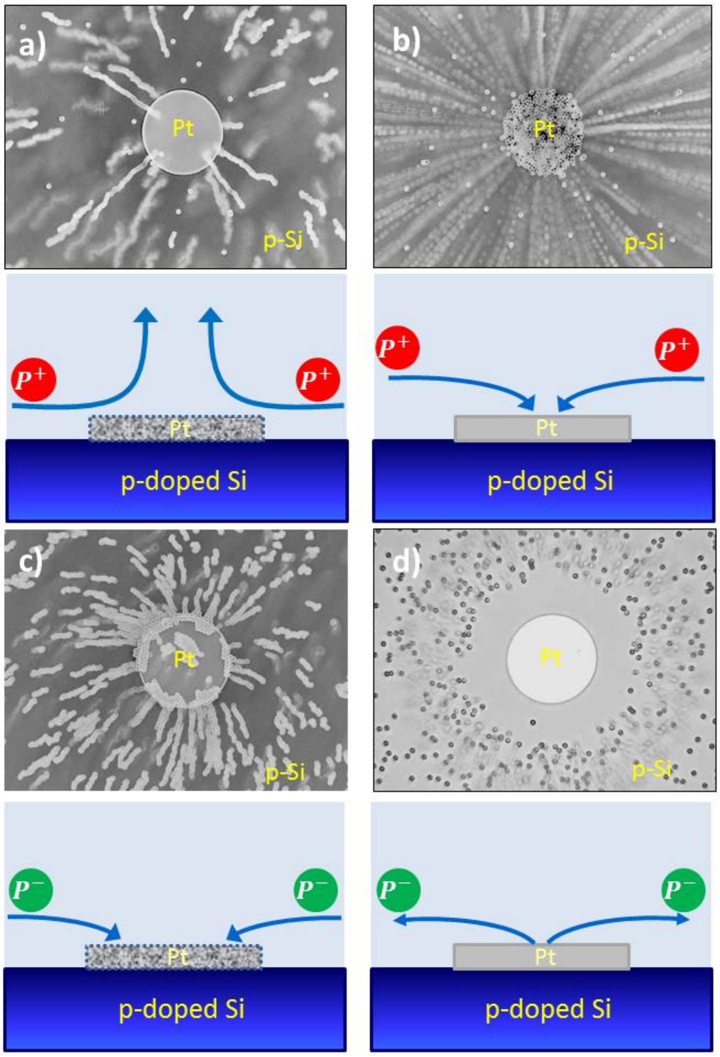

Figure 3.4 Interaction of positive tracers with r-Pt/Si (a) and s-Pt/Si (b) pumps. Interaction of negative tracers with r-Pt/Si (c) and s-Pt/Si (d) pumps. Schemes of the particle trajectory are also included for each pump system.

We also checked by XPS the chemical characteristics of the deposited Pt films prepared with both deposition techniques to rule out possible contaminations of the pump system. The XPS spectra for Pt deposited by sputtering or by electron beam depicted similar profiles (Fig. 3.5). The samples were measured as-received and without previous exposure to oxygen plasma. The experiments were performed with a PHOIBOS150 hemispherical analyser hosted in a UHV system with a base pressure of 5×10^{-10} mbar and using monochromatic Al Kα radiation (1486.6 eV). The spectra reveal carbon contamination (C1s line at 285 eV) arising from the unavoidable exposure to the atmosphere and a weak nitrogen signal at about 400 eV, again due to exposure to air during transport from the deposition equipment to the XPS system. Both samples were exposed less than 30 minutes to the atmosphere. No other contaminants can be detected in spite of the high surface sensitivity of the XPS technique. The effect of potential impurities on the different performance in the catalytic actuation can be ruled out.

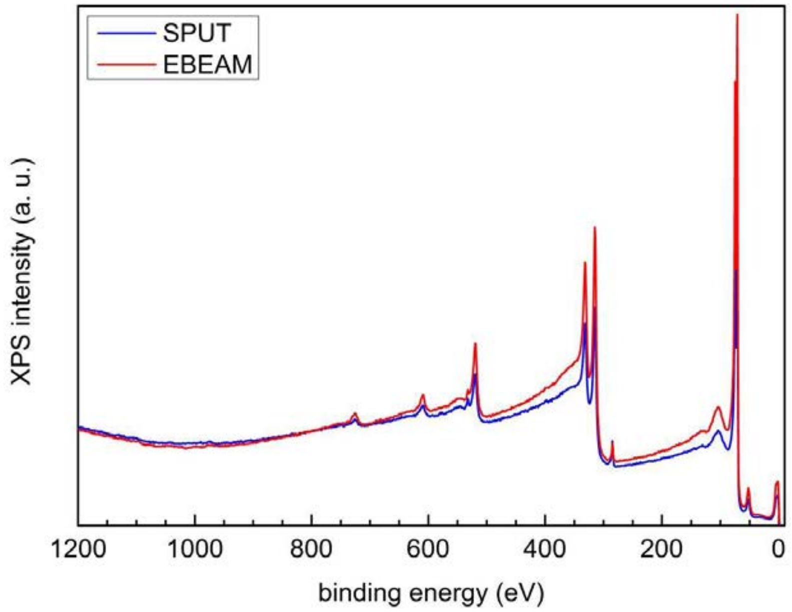

Figure 3.5 Survey XPS spectra of platinum films deposited on silicon substrates by sputtering (blue line) and e-beam evaporation (red line), respectively.

We also evaluated the influence of photoactivation on r-Pt/Si and s-Pt/Si devices by varying the light intensity. Figure 3.6 compares the tracer velocities at three different light intensities (100%, 40%, and below 10% with a neutral light attenuation filter). In the case of s-Pt/Si motors the radial component of the velocity of positive tracers significantly drops as the light intensity is attenuated. In contrast, the motion of positive tracers at the r-Pt/Si system only exhibits a very weak reduction with light attenuation and the negative tracers did not follow any clear trend with light intensity.

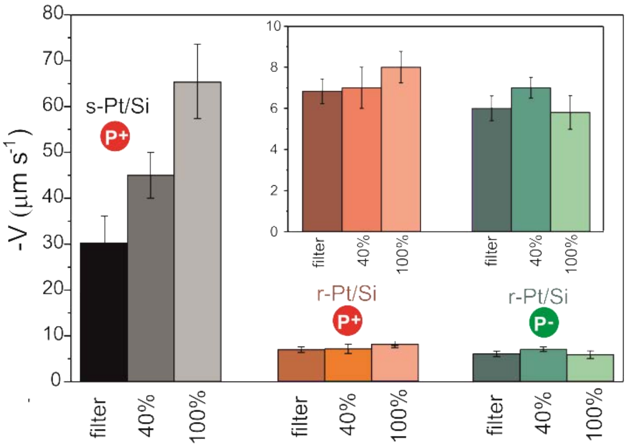

Figure 3.6 Influence of the photoactivation on the s-Pt/Si and r-Pt/Si pumps represented by the variation of the radial component of the tracer velocity as a function of light intensity. The s-Pt/Si devices exhibit strong light responsiveness, whereas the r-Pt/Si ones are almost insensitive to light intensity variation. The figure includes a zoom of the r-Pt/Si pump as inset, for more accurate comparison.

All these findings suggest that the actuation in the semiconductor/metal pumps is a combined effect of two different mechanisms. In the case of the s-Pt/Si pumps the catalytic actuation is dominated by electro-osmosis. The generation of an electric field, which is drastically amplified by light and points towards the Pt disc, is very clear in this case. Such electric field triggers the fluid flow in the same direction and, in addition, induces strong electric attraction of positive tracers towards the Pt, and strong repulsion of the negative tracers (Fig. 3.4). In contrast, the increase of Pt roughness might favour the direct H_2O_2 decomposition at the entire Pt surface area, whose process is light insensitive. In this case, the liquid motion could be driven by the solute concentration gradient created by such reaction localized at the Pt surface. The actuation mechanism could be more in line with a diffusion-osmotic process that totally changes the interaction of charged tracers with the pump.

The fluid flow and electric field values for s-Pt/Si and r-Pt/Si can be extracted by considering that the radial component of the particle speed V_{rp} is driven by two contributions: i) an electrophoretic term (V_{ef}) due to the particle electric charge and ii) the fluid flow velocity (V_f):

$$V_{rp} = V_{ef} + V_f = \frac{\varepsilon \xi_p E_r}{\eta} + V_f \qquad (1)$$

where ε is the fluid permittivity, ξ_p the zeta potential of the particle, E_r the radial component of the electric field, and η the fluid viscosity. The fluid flow velocity and radial component of the electric field are obtained by evaluating the velocities of two differently charged particles (eq. 1). Table 1 collects such parameters. It can be observed the pronounced decrease of the radial component of the electric field and fluid flow for the rougher devices as compared to the s-Pt/Si.

Table 3.1. Maximum values of the fluid velocity (V_{rfmax}) and Electric field (E_{rfmax}) for the different micropumps. Negative sign denotes radial inward direction of the electric field and fluid flow.

System	V_{rfmax} (µm s^{-1})	E_{rfmax} (Vm^{-1})
s-Pt/Si	-(43±1)	-(680±1)
r-Pt/Si	-(7.2±1)	-(24±1)
r-Pt/SiO2	-(5.4±0.8)	31.7±0.8

To gain more insight on these competing mechanisms, we suppressed the possibility of the photoactivated reaction, and hence its associated electric field contribution, by fabricating rough and smooth Pt disks on insulating SiO_2. The Pt discs were patterned on a silicon wafer covered with a thick silicon oxide of 1 µm. On the s-Pt/SiO_2 pump we could not capture any tangible directional motion of the differently charged tracers in the presence of 1% H_2O_2. However, the situation changes dramatically when using rough Pt discs. Figure 3.7 shows the motion of positive and negative particles on r-Pt/SiO_2. Positive particles move towards the Pt disc at maximum velocities of –(4.4±0.6) µm/s. After crossing the Pt edges they drift upwards from the surface (Movie 3.5). Similar behavior is also observed with quasi-neutral particles (ξo= -12 mV) which approach the Pt disc at maximum velocities of –(5.7±0.5) µm/s. Finally, negative particles move towards the Pt disc with maximum velocities of –(6.9±0.5) µm/s and once they are on the Pt disc they stick to its surface (Movie 3.6). These different responses suggest the generation of an electric field in the Pt disc pointing outwards. However, this electric field seems to be not strong enough to repel the positive particles from the Pt surface, also due to their lower charge as compared to that of the negative tracers. As a result the tracer movement is less sensitive to the electric field and positive particles tend to follow the fluid flow.

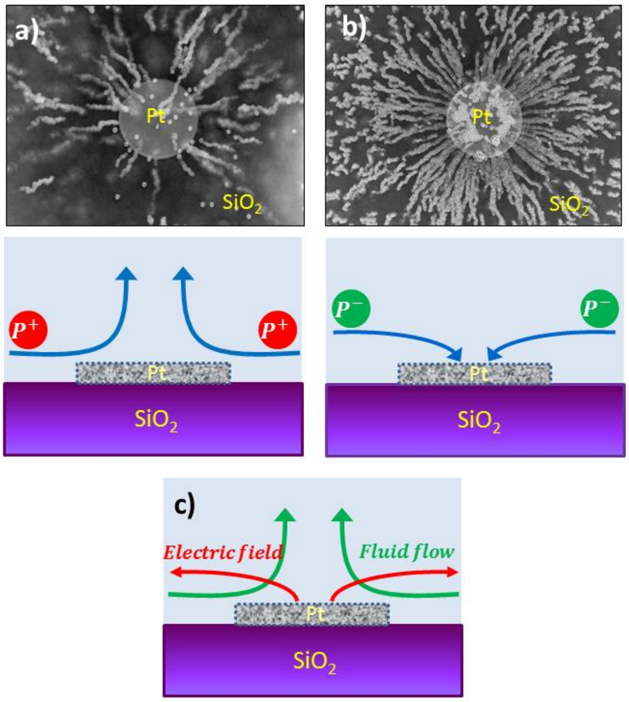

Figure 3.7 Interaction of positive (a) and negative (b) tracers with the r-Pt/Si system. Schemes of the positive and negative tracer trajectories at the rough Pt/Si pump are also included. c) Schematics depicting the fluid flow and electric field direction.

Equation 1 was used to quantify the fluid flow and electric field at the rough Pt/SiO_2 pump. By analyzing the velocity values for positive and negative particles, the maximum values of the radial fluid flow speed (Vp) and electric field E were found to be -5.4 $\mu m \cdot s^{-1}$ and 31.7 Vm^{-1}, respectively (Table 3.1). The analysis of the differently charged particle velocities demonstrates the existence of an electric field pointing outwards, from Pt towards SiO_2. Such direction of the electric field is opposite to the field direction expected from an electro-osmotic process in a pump with components with negative zeta potentials as it is in the case of silicon and platinum. In pumps with negative zeta potentials, the electric field should drive the fluid flow in the same direction according to the equation,

$$V_f = -\frac{\varepsilon \xi_s E_r}{\eta} \qquad (2)$$

where ξ_s is the zeta potential of the surface (<-40mV in our case due to the strong contribution of the negative surface potential of silicon).[182] Therefore, such weak electric field is not responsible of triggering the fluid flow that moves in opposite direction. The catalytic actuation for the r-Pt/SiO_2 is more in line with a diffusio-osmosis process favoured by the direct decomposition of H_2O_2 on the rough Pt surface. The fluid moves towards the region where the reaction takes place, i.e. the region with higher solute concentration (and higher osmotic pressure).

The existence of a weak electric field in the metal/insulator pump is in line with previous findings in metal/insulator Janus particles. In such Janus particles, electric field generation due to charged reactions and ionic effects was found.[183,184,185] As also mentioned in the previous chapter, the origin of such ionic effects has been attributed to different sources. It was proposed that metal catalyst asymmetries, such as different metal thickness, could yield to a reaction scheme involving charged intermediates.[184] That could be a plausible explanation for rod and sphere like structures capped with catalyst since a gradient of thickness is expected after metal evaporation, with more catalyst at the pole regions than at the equator sides. However, this kind of thickness asymmetries is expected to be negligible on the flat configuration of a pump. Other studies suggested dissociation of H_2O_2 and water in ions at the surface and bulk as additional sources for a self-generated electric field.[185] However, the electric field at the r-Pt/SiO_2 is not the driving force of the fluid flow since in fact it should generate electrokinetic fluid flow in the opposite direction to what it is observed. Therefore, the electrokinetic or electro-osmotic process is discarded in the metal/insulator pump. The chemical origin of the electric field is not well known at this moment but future studies including photoemission spectroscopy, scanning electric force microscopy in water/H_2O_2 and scanning electrochemical microscopy are pursued to better understand the Si/Pt interface and the precise chemical reaction schemes that could yield to an electric field in such conditions.

3.3 CONCLUSION

In view of the findings with insulating SiO_2/Pt, we demonstrate that at least two chemo-mechanical mechanisms are behind the liquid pumping of Si/Pt pumps. One is rooted in a photoactivated reaction taken place in two separated redox reactions: the oxidation of H_2O_2 at the Si side and the reduction of H_2O_2 at the Pt side. Such reaction scheme drives a fluid flow triggered by an electro-osmotic process. A proton current from Si towards Pt generates an electric field towards Pt that drags the fluid towards the metal structure. As mentioned above, this mechanism is highly sensitive to light. The second mechanism features diffusion-osmotic characteristics, with H_2O_2 decomposition taking place mainly at the Pt region. In this decomposition process the fluid flow is dragged towards the Pt structure to compensate the higher solute concentration and higher osmotic pressure. This latter mechanism is not light responsive. The dominance of one chemomechanical mechanism over the other depends on the fabrication characteristics of the pumps, in particular to the roughness of the catalyst. In smoother Pt/Si pumps the photoactivated electro-osmotic mechanism prevails, whereas the diffusion-osmotic and light insensitive one dominates in rough Si/Pt. A schematic of the comparison between these two competing mechanisms is shown in Fig. 2.8. These findings of rough Pt/Si pumps are consistent with what we observed from the sputtered Si/Pt nanomotor described in Chapter 2. In the case of rough sputtered Si/Pt nanomotors, light insensitive diffusiophoresis mechanism dominates the propulsion process. On the other hand, we were not able to observe similar results in evaporated Si/Pt nanomotors with respect to the photoactivated electro-osmosis in smooth Pt/Si pumps

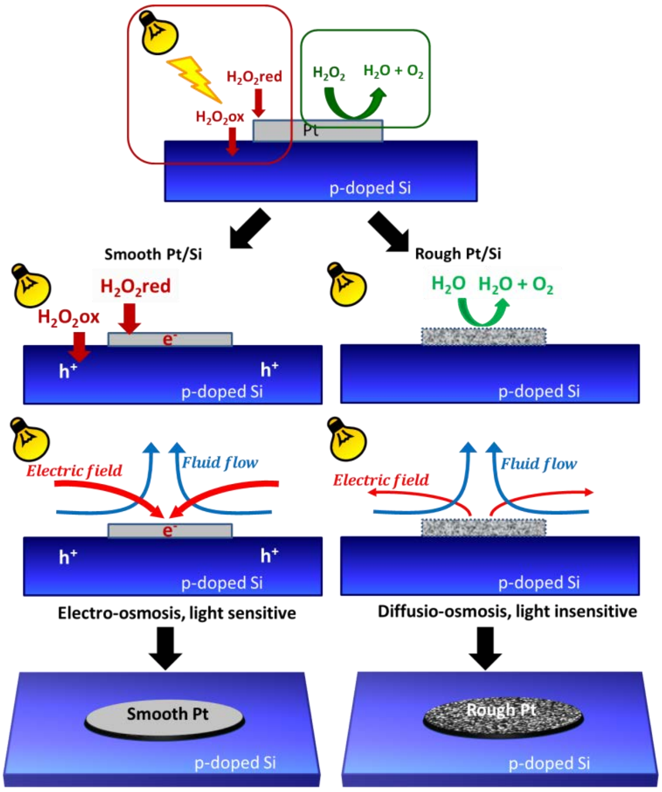

Figure 3.8 Schematics of two competing mechanisms: the photoactivated electro-osmosis which prevails on smooth Pt/Si pumps and the light insensitive diffusion-osmosis which dominates on rough Pt/Si.

As a consequence, to build-up light sensitive nanomotors, separated redox interfacial reactions between Si and Pt have to be maximized, for instance by increasing the perimeter of the interface to enlarge redox reaction area between Si/Pt and by decreasing the roughness factor of Pt. This outcome is crucial for the design of new photoactivated silicon based nanomotors with visible and near infrared light and to increase their level of control.

4 UNDERSTANDING THE SI/PT INTERFACE

4.1 INTRODUCTION

In the previous chapters, we studied the novel silicon based nanomotor and its immobilized micropump counterpart. We proposed that there were two competing mechanisms at Si/Pt nanomotors in the presence of H_2O_2 under visible light exposure. They were the photoactivated electro-osmosis, which prevailed over smooth Si/Pt interfaces, and the light insensitive diffusio-osmosis which dominated on rough Si/Pt interfaces, respectively.

Previous results with smooth Pt/Si micropump showed that just water could also fuel pumps mediated by light besides the reactive H_2O_2. Such result is still not well understood.[61] The light induced water decomposition on Si/Pt systems is also an important process to assess since it can provide us useful clues of the light induced process with other photochemical fuels such as H_2O_2.

Moreover, we had also found that the chemomechanical actuation was even enhanced when performing oxygen plasma treatment on the Si/Pt system. Such plasma activation effect was already observed in previous experiments of our group with Au/Pt pumps. In that case the plasma treatment enhanced the redox driving force, increasing the performance of Pt as cathode electrode. That was confirmed by electrochemical Tafel measurements[46] and was attributed to an increase of oxygen moieties at the metal surface.

Therefore, in this chapter, the surface chemical states of silicon, platinum and Si/Pt interface are studied by X-ray photoelectron spectroscopy (XPS) either in the ultra-high vacuum conventional way or using near-ambient pressure conditions in which condensed water can be formed, thus mimicking conditions similar to aqueous solution. These measurements could help to grasp a better understanding of the physicochemical mechanism of Si/Pt nanomotors, especially the chemical routes of reduction–oxidation reaction at Si/Pt interfaces and the effect of oxygen plasma treatment under condensed water. For instance, these photoemission studies could help to better assess the (photo)electrochemical reaction and its location (e.g., if the anodic reactions at the Si and cathodic reactions at the Pt are more favoured by the proximity of the Si/metal interface), based on the modification of the amount and nature of the oxygen moieties at Si or Pt surface.

The fundamental understanding of such (photo)electrochemical interfaces could give us clues to develop light activated silicon based motors with higher efficiency and improved performance for their potential and appealing applications.

As mentioned, the experiments were carried out in ultrahigh vacuum (UHV) and water vapour ambient, and also the effect from visible light illumination was investigated. We tested samples with and without oxygen plasma treatments to study the role of oxygen played in the process.

A Perkin Elmer PHI 5500 XPS system with monochromatic Al X-ray source (1486.6eV) was used to perform the measurement in ultra-high vacuum (10^{-10} mbar). In addition, the Near-Ambient Pressure Photoemission (NAPP) was employed to study the silicon/platinum interface in water ambient, which takes the advantage of mimicking the working conditions to our Si/Pt experiments and, importantly, taking into consideration that water could also behave as a fuel for the Si/Pt system. These measurements were performed at the NAPP endstation of the CIRCE beamline at the ALBA synchrotron. One of the main advantages of synchrotron radiation source is its easy selection of incident photon energy, the small size of the beam, and the possibility to change its intensity.

Patterned Si/Pt samples with dimensions 10 mm x 10 mm were tested. The Pt films were deposited on Si substrate by electron beam deposition and sputtering respectively with a mask covering half of the surface. One prepared sample is shown in Figure 4.1. The samples were activated with oxygen plasma prior to measurements. External illumination (visible LED light at 470 nm wavelength) was provided by a LED source coupled to and optical fibre, whose output light was focused with a lens in order to illuminate only the sample surface, and not the whole sample holder to minimize heating. High resolution photoemission experiments were performed at photon energy 235 and 680 eV respectively, at the silicon and platinum areas (far away from the Si/Pt interface) and at the Si/Pt interface in order to probe the possible photo-induced redox reactions taking place at this region. The 235eV photon energy provides sufficient surface sensitivity for the Si 2p and Pt 4f lines (binding energy at 99.3 and 71.0 eV respectively), while 680 eV guarantees surface sensitivity for O1s electrons (binding energy at 530 eV) and allows exploring the subsurface contribution from silicon and platinum. Moreover, a good sensitivity of the oxygen signal is key to monitor the water condensation conditions on sample surface. Experiments were performed under LED illumination (ON) and in the dark (OFF) in order to search for potential effects induced by visible light illumination. In NAPP, the analysis chamber was filled with water vapour (3 mbar) and the sample was cooled down to 0^0C with a Peltier stage. Such conditions provided a thin liquid water layer on the surface without forming ice.[186]

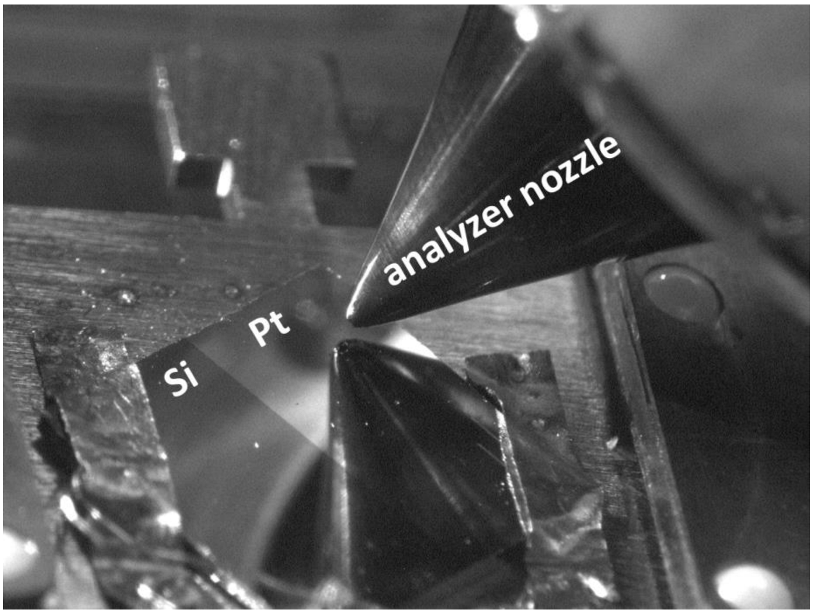

Figure 4.1 captured picture of e-beam evaporated sample mounted on the Peltier sample holder.

4.2 XPS MEASUREMENTS AT HIGH VACUUM AND ROOM TEMPERATURE

At first, the photoemission measurements of Pt/Si were performed in a vacuum of 10^{-6}mbar at 680 eV. Under these conditions, although a water monolayer can be formed at a rate of 1 monolayer/second, the water undergoes dynamical adsorption/desorption transitions. Figure 4.2a shows a typical XPS spectrum for Pt 4f without being activated by oxygen plasma with the characteristic spin–orbit splitting doublet corresponding to the metallic bonding (centred at a binding energy, E_b, of 71 eV and with a ΔE separation of 3.33 eV). Figure 4.2b shows XPS profiles when the Pt is plasma activated at the same energy, pressure and temperature. It can be observed that when Pt is treated, additional peaks appeared at higher binding energies of the metallic Pt doublet which correlate well with oxidized states of Pt. The figure 4.2b shows a least-square peak fit after a Shirley-type background subtraction of the Pt 4f line using 4 components which correspond to metallic platinum (blue, E_b= 71.0 eV), platinum with oxygen adsorbed on the surface (red, Pt-O_{ads}, E_b=72.1 eV), PtO (navy, Pt^{2+}, E_b=72.9 eV) and PtO_2 (green, Pt^{4+}, E_b= 74.1 eV) respectively.[187] In the least-square fit, a Gelius-type asymmetric line shape was used for the metallic components (blue line) while the profile shapes for the rest of components (red, navy and green) were symmetric. The FWHM (Full width at half maximum) for the 71.0 eV feature was <0.6 eV. The following constraints were used: (i) same branching ratio and spin orbit splitting for all components and (ii) identical FWHM only for the symmetric components. This same methodology of analysis was applied for the following measurements in order to have a reliable quantification and to capture subtle details of the effect of water. The experimental data and the envelope from the fit are represented by the continuous black and yellow lines respectively and show a very good fitting procedure.

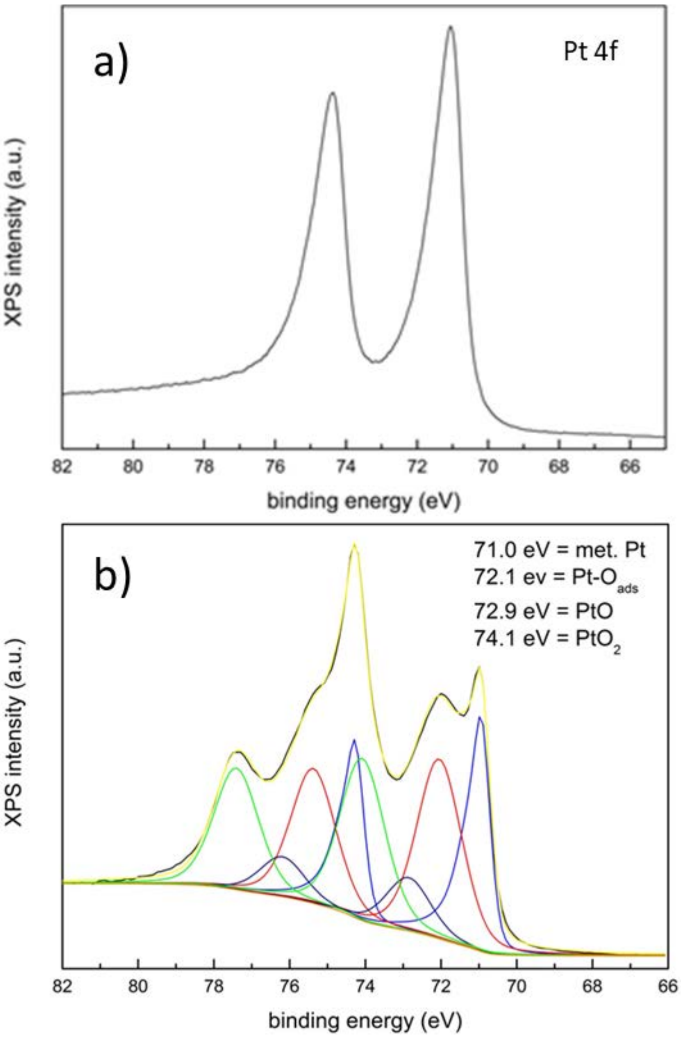

Figure 4.2 a) spectrum without oxygen plasma treatment. b) Pt 4f spectra of a plasma treated sample. The figure also shows the least-square fit after a Shirley-type background subtraction using 4 components. All experiments were carried out at 680 eV, 10^{-6} mbar and room temperature.

Given the high intensity characteristics of synchrotron radiation it is very important to assess the extent of beam effects on our systems to avoid misinterpretations of the photoemission data. In order to evaluate the effect of the x-ray beam on the Si/Pt sample, the time evolution of the Pt 4f photoemission spectra was followed at two sample spots, one of them at the middle of the Pt sample and the other at the Si/Pt edge under a vacuum of 10^{-6} mbar and room temperature. The Pt 4f spectra were continuously acquired during 44 minutes in the case of Pt spot and during 24 minutes in the case of Si/Pt spot. Only very weak changes were observed in the time evolution profiles. The most obvious effect was the slight reduction of the signal associated to PtO_2 and the slight increase of both the Pt-O_{ads} and metallic Pt features as indicated in Fig. 4.3 c and d, which show the first and last measurements during the elapsed time of 44 minutes. Such slight increase in Pt-O_{ads} and Pt signal can be attributed to a beam effect which induces a small reduction of PtO_2 to be transformed in Pt-O_{ads} and Pt. Therefore we conclude that under these conditions the beam effect is very weak.

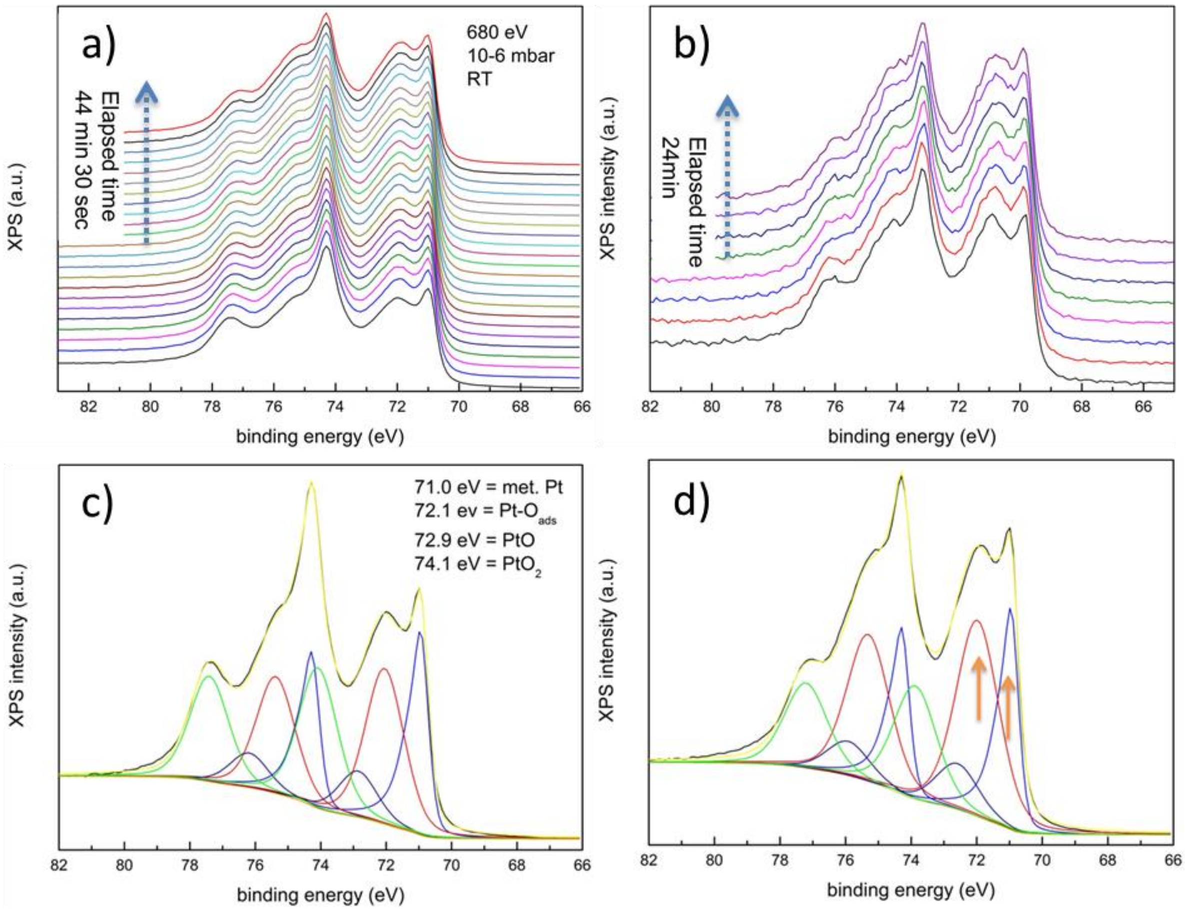

Figure 4.3 Time evolution of the photoemission spectra of the Pt 4f line taken with 680 eV photons at 10^{-6} mbar and room temperature on the Pt film (a) and at the Si/Pt edge (b). The changes in the electronic states of oxidized are due to continuous exposure to the beam at the same spot and is more representative at the Pt region. (c) and (d) represent the first and last measurements during the elapsed time of 44 minutes.

4.3 XPS MEASUREMENTS WITH CONDENSED WATER

In this section we characterize the Si/Pt system previously activated with oxygen plasma and in presence of condensed water which was achieved under a water vapour pressure of 3 mbar and temperature of 0^0C.[186] The O 1s profile at 3 mbar and 0^0C as shown in Figure 4.4 indicates condensed water on the top.

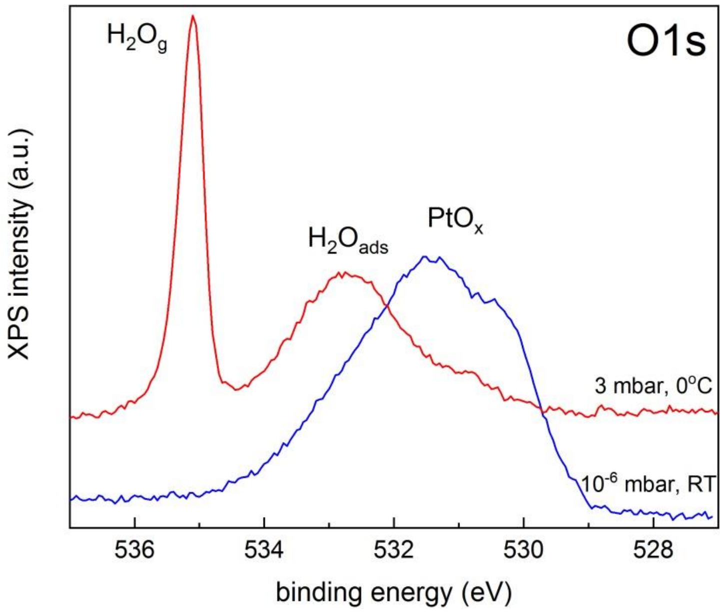

Figure 4.4 O 1s spectra at 3 mbar, 0^0C (red) and 10^{-6} mbar, room temperature (blue) indicate topmost chemical components.

In order to assess X-ray beam effects on the Si/Pt system, the measurements were acquired continuously at the same sample spot during 35 minutes. Figure 4.5 shows the photoemission evolution at the Pt side. A strong enhancement of the reduction of the different platinum oxides due to the combined effect of the beam and the presence of water is observed at both regions. Similar behaviour was observed when measuring at the Si/Pt edge.

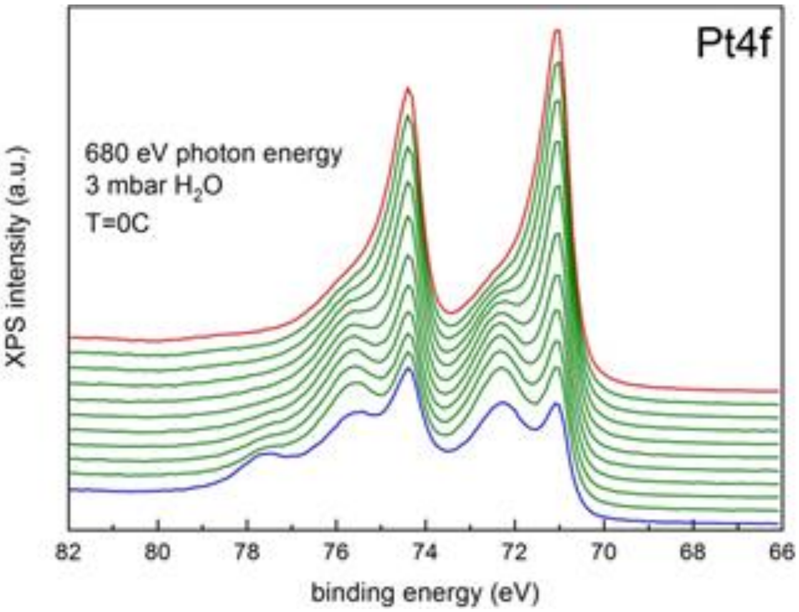

Figure 4.5 Photoemission spectra of the Pt 4f line taken with 680 eV photons at 3 mbar water vapour and at 0^0C evidencing the reduction effects due to continuous exposure to the beam at the same spot. The blue spectrum is the one measured at the beginning and the red is the last one.

An analysis of the evolution of the peak areas of the different components of Pt as a function of time (consecutive spectra) is shown in Figure 4.6. The feature corresponding to metallic Pt increases almost linearly, Pt-O_{ads} slightly increases initially and then decreases substantially, while PtO_2 slightly decreases from the very beginning. The evolution of the PtO line is less clear due to the dominating metallic Pt and Pt-O_{ads} lines.

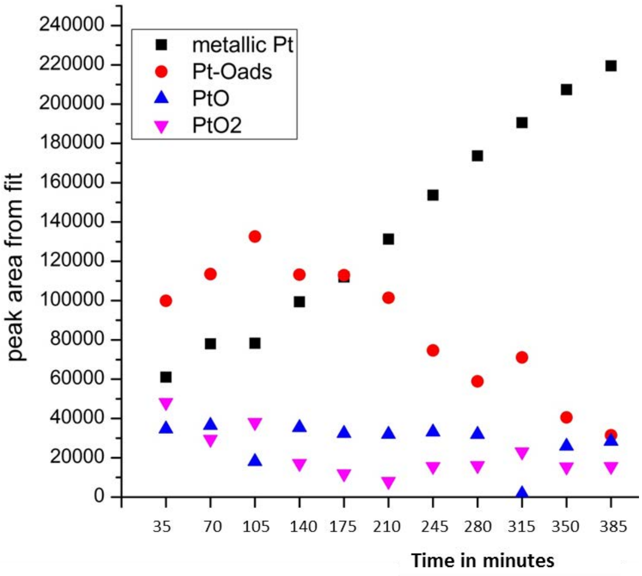

Figure 4.6 Evolution of the peak areas as a function of the consecutive spectra (or time) of the four components corresponding to the spectra from Figure 4.5.

At 680 eV, the XPS spectra has more contributions of bulk Pt which masks the subtle variations of the oxidized Pt signals allocated more at the surface. A similar study on the plasma activated Si/Pt system was performed at the same temperature and water vapour pressure, but using the energy of 220 eV which is more surface sensitive (see Figure 4.7). The features corresponding to metallic Pt signals demonstrate similar trends with respect to the results at 680eV. However, Pt-O_{ads} signal remains in a significant amount during the whole analysis exhibiting only a very slight increase at very short times and a very slight decrease at longer times. PtO slightly decrease but a significant decline in the PtO_2 signal was captured.

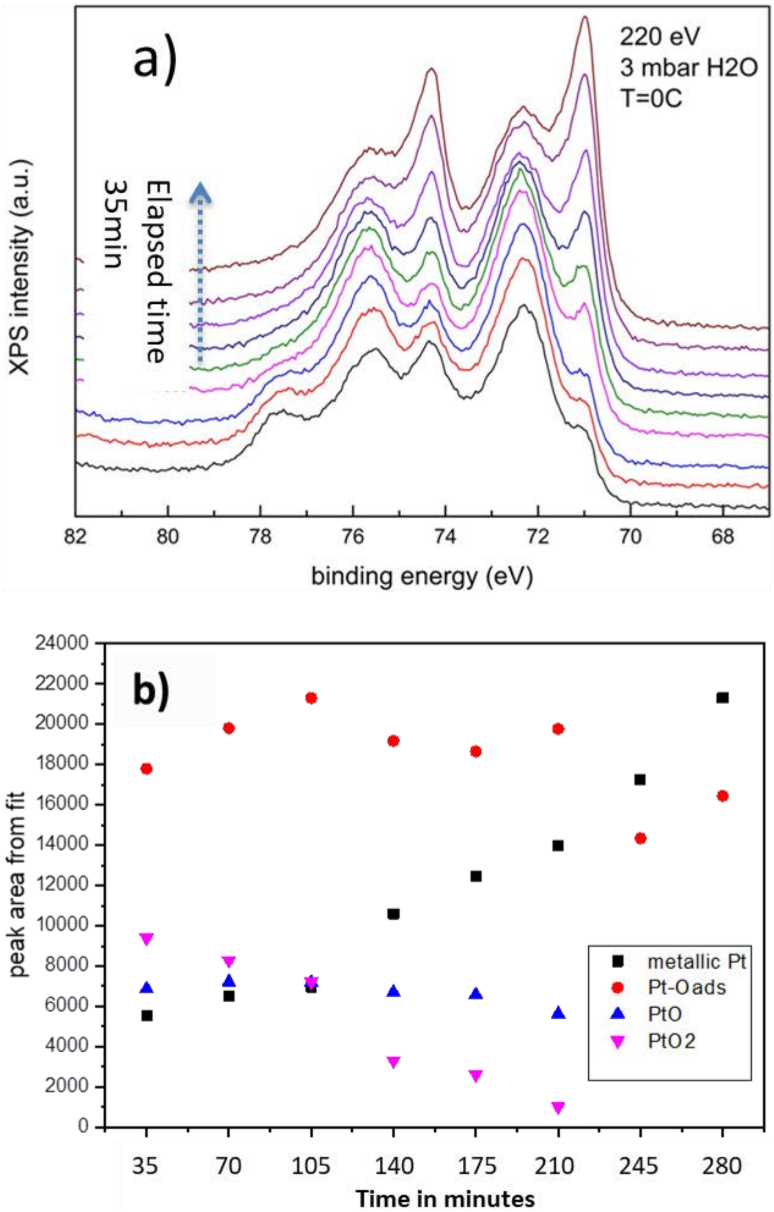

Figure 4.7 a) Photoemission spectra of the Pt 4f line taken with 220 eV photons at 3 mbar water vapour and at 0^0C evidencing the damage due to continuous exposure to the beam at the same spot. b) Evolution of the peak areas as a function of the consecutive spectra (or time) of the four components corresponding to the spectra from (a).

In contrast to the XPS results obtained at UHV in which no significant beam damage is observed, beam effects become extremely important for Si/Pt system with condensed water. We can conclude that the platinum oxide is reduced to Pt-O_{ads} and metallic compounds in the presence of water and X-ray exposure. The beam can induce radiolysis in the condensed water caused by the beam which generates radicals, ions, solvated electrons and molecular species that can interact with the surface. Thus, although we do not have direct experimental evidence of the presence of reactive water fragments, we hypothesize that the reduction observed at the platinum surfaces is mainly originated by the presence of highly reactive species. One may tentatively associate the observed reduction to the strongly reducing agents e_{aq}- and H$^{\cdot}$, although other species may play a role. Such strong beam effects enhanced by water mask the chemical pathways associated with the performance of Si/Pt pump in water under LED illumination.

4.4 PROBING EFFECTS OF LIGHT AND H_2O/H_2O_2 USING CONVENTIONAL UHV-XPS

The impact of light on the plasma activated Si/Pt could not be obtained in condensed water XPS, since it was masked by the e-beam damage effect. We then used to the conventional UHV XPS measurements in order to explore if complementary insights were still possible to achieve for our system.

In this section, we further performed XPS measurements of plasma treated Si/Pt systems but after been subjected to the chemical fuel (water and H_2O_2 solution) and light *ex-situ* to see if they could give evidences of chemical changes and thus get more clues about the chemical pathway in the Si/Pt system.

We used patterned Si/Pt samples (size: 10 mm x 10 mm) consisting of silicon substrate half coated by Pt using e-beam technique and the photoemission studies were performed at the Si side, Pt side and Si/Pt interface. Five types of sample were prepared ex-situ:

i) sample with only O_2 plasma treatment
ii) sample with O_2 plasma treatment and subsequent water immersion for 30 minutes,
iii) sample with O_2 plasma treatment and subsequent water immersion with light for 30 minutes,
iv) sample with O_2 plasma treatment and subsequent immersion in 1%wt H_2O_2 for 30 minutes,
v) sample with O_2 plasma treatment and subsequent immersion in 1%wt H_2O_2 with light for 30 minutes.

The light source was a visible LED light at 470 nm wavelength. The samples were measured by XPS in UHV as soon as they were prepared.

Figure 4.8 illustrates the Pt 4f profiles at Pt side and Si/Pt edge under different conditions. The spectra are normalised to Pt 4f metallic peak at 71 eV. It can be seen that incubation in water and H_2O_2 only increases the contribution of PtO_2 irrespective if they are measured in the middle of Pt part or at the edge of Si/Pt or if they are illuminated or not.

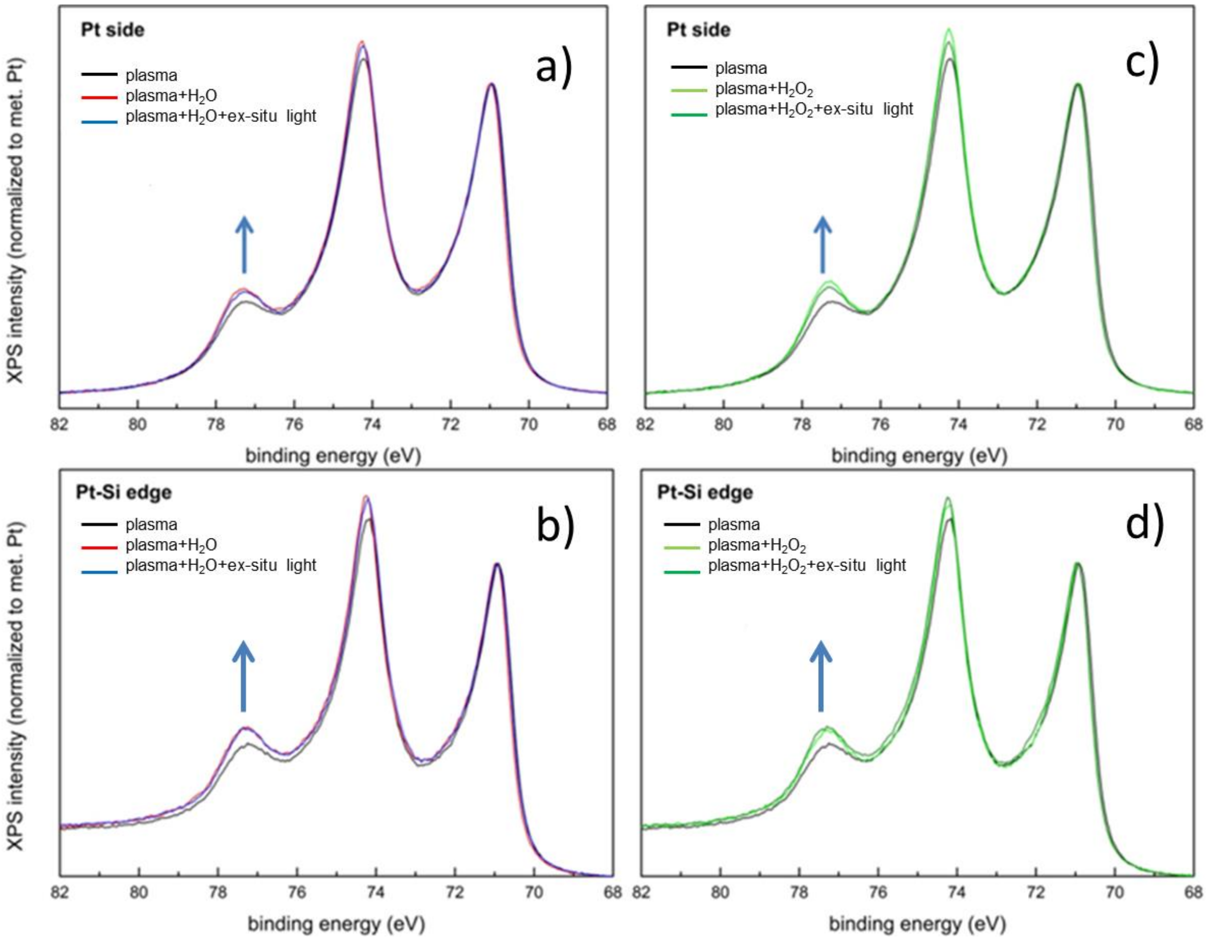

Figure 4.8 Pt 4f profiles with monochromatic Al X-ray source (1486.6eV) and in ultra-high vacuum (10^{-10} mbar). (a) and (b) are Pt 4f profiles of samples with plasma treatment, plasma treatment and water immersion with light on and off at Pt side and Si/Pt edge respectively. (c) and (d) are Pt 4f profiles of samples with plasma treatment, plasma treatment and 1%wt H_2O_2 immersion with light on and off at Pt side and Si/Pt edge respectively.

However, when comparing samples probed at the Pt side with the ones at the Si/Pt edge, we captured a slight shift in the chemical states of Pt towards more metallic ones. Such effect has been observed in the 5 samples under study. We could speculate that a more reduced state of Pt seems to be present at the Si/Pt edge as compared to the Pt side. This effect already appears with the plasma treated sample without being subjected to further treatments.

Figure 4.9 compares Pt 4f spectrum taken at Si/Pt edge and Pt side from the sample with plasma treatment only in which the slight shift in the chemical states of Pt towards more metallic ones is observed in thePt 4f profiles at the Si/Pt edge with respect to the ones at the Pt side.

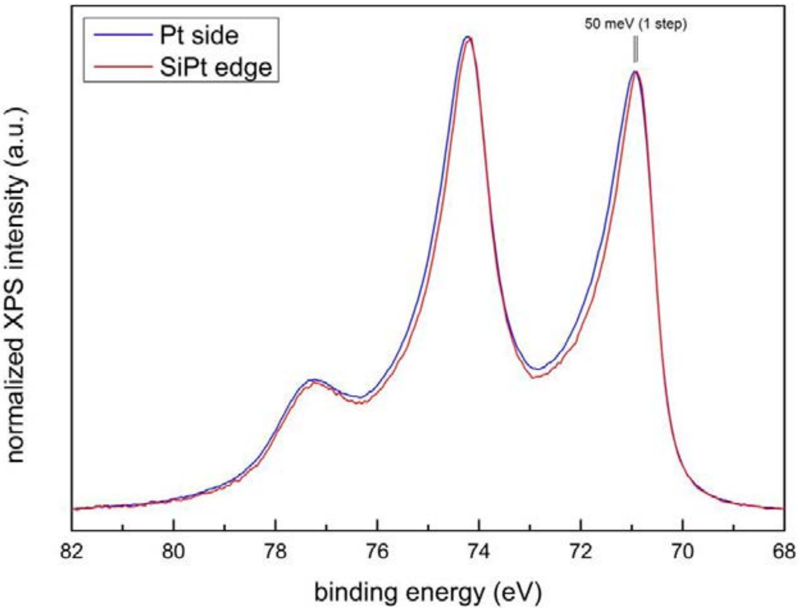

Figures 4.9 comparison of Pf 4f spectrum at Si/Pt edge and Pt side from the sample with only plasma treatment.

Therefore, we are not able to provide conclusive remarks on the chemical pathway of these Si/Pt systems under illumination, since no strong effects have been achieved with the ex-situ illumination measurements. Although in these measurements we do not have the beam effect that masks potential chemical changes at the interface, several limitations should be taken into account when carrying out conventional XPS measurements. Firstly, the high energy (1486 eV) applied for measuring makes the technique less surface sensitive, and higher response from the bulk Pt is captured as compared to synchrotron radiation. Thus, it may not able to obtain subtle changes produced at the surface. Secondly, the large incident X-ray spot (3mmx1mm) makes it difficult to record chemical changes if they are only concentrated at the Si/Pt edge.

4.5 CONCLUSION

To conclude, XPS measurements were conducted in UHV and in the presence of water vapour using different photon energies. At 10^{-6} mbar under synchrotron radiation, the beam damage is very weak, slow, and slightly translates in a reduction of the Pt^{4+} species with an increase of the Pt-O_{ads} and metallic components. However, in the presence of condensed water, the beam induced damage is very important, much faster and it evolves to a preferential reduction of Pt4+ species to Pt-O_{ads} and mainly to Pt ones. The reduced areas after X-ray exposure do not oxidize again in the presence of condensed water.

Beam damage is a critical issue for this system and it masks the pursued effect of evaluating the photoelectrochemical pathway, reaction location and plasma impact on the Si/Pt systems. Comparison with parallel studies undertaken at ICN2 using a conventional X-ray (monochromatic) source could suggest that platinum at the Si/Pt edge is more reduced as compared to the platinum film. But such result was independent of ex-situ light/fuel exposure.

Concerning the techniques we used, NAPP takes the advantage of working in more real conditions, more surface sensitive and smaller probe, but the problems with beam effects in the Pt/Si system have shown to be a strong limitation for our systems. One the other hand, UHV XPS does not have the problem of beam effects. However, it collects more information from the bulk substrate and has a bigger probe for exploring local spatial changes. With such limitations we could not achieve significant insights on the chemical states of the components and in the chemical pathways taking place during the chemomechanical actuation.

Further studies on this topic could be accomplished using more local probe microscopies which could give complementary information on the surface charge density, electric field, redox reactions, etc., by combining electrostatic force microscopy in water or H_2O_2, and scanning electrochemical microscopy.

5 TOWARDS LIGHT CONTROLLED MICRO-/NANO MOTORS FOR BIO-CONTAMINANT REMOVAL

5.1 INTRODUCTION

In this chapter, on the one hand, we present a new approach to fabricate light controlled silicon based motors by introducing silicon np junctions capped with Au. The goal is to overcome the limitations found in the case of Si/Pt motors and to build more effective photochemically controlled motors. These are preliminary results, which need a more thorough study and optimization but these first findings hold great promise.

On the other hand, we introduce new photochemical motors based on Si/Fe. Besides the capability of Fe of promoting the electron trapping from the excited hole-pair at the Si under illumination, the magnetic iron component can also promote Fenton reactions. Moreover, the motion of the Si/Fe can be increased by magnetic stirring, thus enhancing the mass transfer and the kinetics of the chemical reactions. The use of iron-silicon based structures is very attractive as a low cost but efficient strategy for organic pollutant degradation.

5.2 LIGHT CONTROLLED SILICON BASED MOTORS

In the previous chapters, many efforts have been devoted to studying the propulsion mechanisms of Si/Pt nanomotor that we originally proposed. The results indicate that direct decomposition of H_2O_2 at platinum surface dominates the overall propulsion of Si/Pt nanomotor. As schematically shown in figure 2.8 in chapter 2, the photoactive reaction between silicon and platinum part is relatively weak and significant photo response cannot be achieved in this configuration. The results from silicon micropump illustrate that separated redox interfacial reactions between Si and Pt should be maximized to develop light sensitive motor. This effect can be achieved by increasing the perimeter of the interface and decreasing the roughness factor of Pt.

As an alternative approach, platinum cap layer can be replaced by gold to enhance the photoactive reaction by minimizing the direct decomposition of H2O2. On the one hand, it is easier to obtain a smooth thin film of gold with respect to platinum. On the other hand, the direct decomposition of hydrogen peroxide is slowed down in the presence of gold catalyst.

It is also worth noting that the silicon based nanomotor diameter is much smaller compared to that of the micropumps we investigated. The size effect may play an essential role in the different behaviours of photo response, which is related to the perimeter of the interface between silicon and noble metal.

Last but not least, the photoelectron generation can be enhanced if a PN junction at the silicon part is introduced. As shown in figure 5.1, an electric field is built-up in the interface in a Si PN junction because of charge diffusion at the interface from n-Si and p-Si. As a consequence of doping, there is a large amount of mobile electrons on the n-type side, but very few mobile electrons on the p-type side. Because of the random thermal motion of the free electrons, electrons from the n-type side start to diffuse into the p-type side. The same happens on the p-doped region. There is a large amount of mobile holes on the p-type side, but very few mobile holes on the n-type side and holes in the p-type side, start diffusing across into the n-type side. As the electrons in the n-region diffuse across towards the p-type side, they leave behind positively charged n-dopant ions, near the interface between the n and p regions. Similarly, the positive holes in the p-type region diffuse towards the n-type side and leave behind negatively charged p-dopant ions. This process sets up an electric field right at the junction between the n-type and p-type material pointing from the positively charged ions in the n-type region to the negatively charged ions in the p-type part. Under light illumination the excited hole-electron pair can be more efficiently separated due to such built-in electric field. The electrons will be more attracted towards the positive charge on the n-type material side. Similarly, the holes will be more attracted to the negative charge on the p-type material side. Such process will promote a current of the excited electrons towards the metal cap in contact with the n-type segment, thus favouring the reduction of the chemical fuel at the n-doped Si/metal side and the fuel oxidation at the p-doped Si.

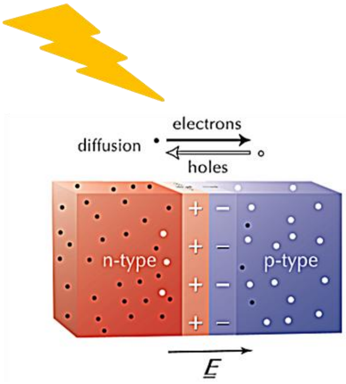

Figure 5.1 electron/hole pair generation at PN junction under light illumation.

Therefore, we proposed silicon microdiodes (3 μm × 3 μm × 3 μm in dimension) with a 50nm gold layer on the top. The microdiode was fabricated by a vertical deep reactive ion etching (DRIE) of PN silicon wafer using the Bosch process.[188] The gold layer was deposited by e-beam evaporation with the same recipe as for the silicon micropump fabrication, which gave smooth gold surface. During gold evaporation, the PN junction was protected by a 50nm thick silicon dioxide layer on side walls to avoid short circuit between the top gold layer and the PN junction. Such silicon dioxide layer was initially introduced to protect the microdiode during reactive ion etching process to obtain a thin anchor underneath for releasing microdiodes from substrate. The SiO_2 protective layer was removed by a subsequent selective chemical etching in HF solution before the microdiodes were released in water under sonication.

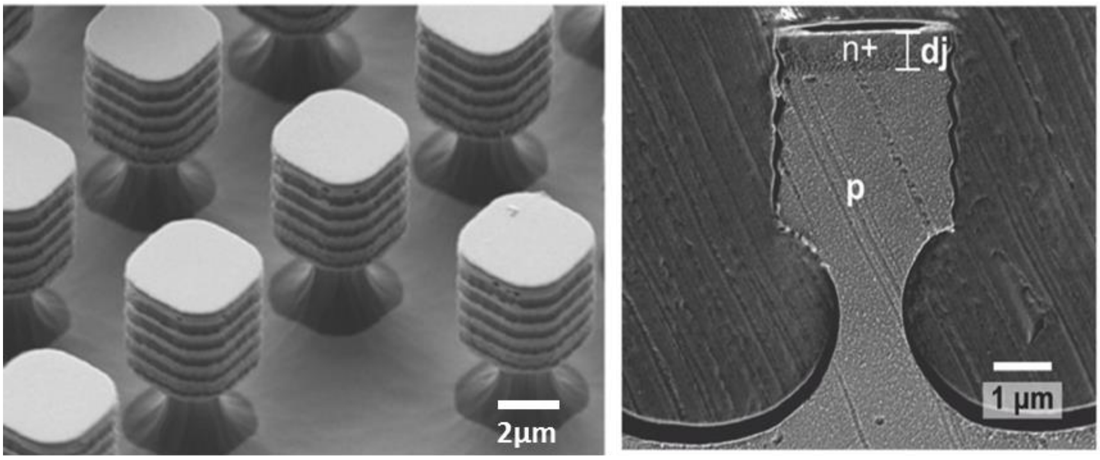

Figure 5.2 SEM image of microdiodes with gold layer on the top (Left), SEM image of cross section of the PN junction with junction depth of 560nm (Right).[188]

As a preliminary test, we investigated the suspended Au/silicon microdiodes in water under microscope. Notable directional motion was observed in the presence of 1% H_2O_2 with a recorded maximum speed of 1.54um/s under white illumination through the microscope objective. The velocity of the microdiode significantly drops to zero as the light intensity was attenuated from 100% to 40%. The trajectory of a Si microdiode in 1% H_2O_2 aqueous solution was shown in Figure 5.3. These findings were consistent with the results from micropumps.

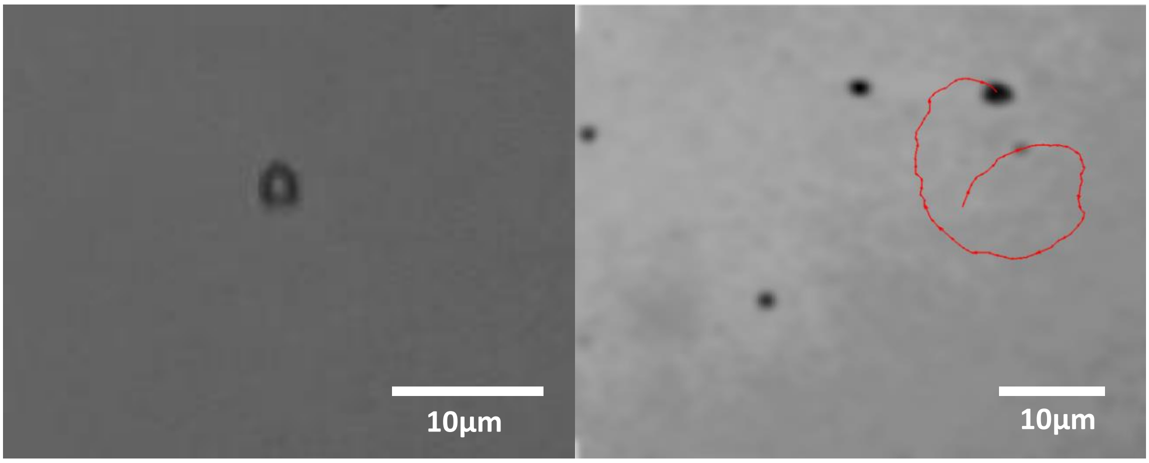

Figure 5.3. A silicon microdiode under microscope (Left), trajectory of the silicon microdiode in the presence of 1% H_2O_2 solution achieving maximum speed at 1.54um/s (Right).

Therefore, it has been demonstrated that visible light sensitive silicon motor could be established by introducing a PN junction and increasing the size of the motor from nanoscale to microscale. Under light illumination the electric field at the pn junction favors the charge separation and avoids recombination, thereby inducing more efficient redox processes at the p-Si and n-Si/gold interfaces. Possible chemical pathways of the redox process are the ones below in which protons are produced at the anode and consumed at the cathode. Such redox reactions would induce a net proton current from anode to cathode and hence an electric field in such direction (Figure 5.4). The electric field would drag fluid in the same direction and the propulsion of the motor in the opposite direction. The process can be expressed in the following equations:

Anode (p-type Si): $H_2O_2 \rightarrow O_2 + 2H^+ + 2e^-$

or/and

Anode Si: $Si + H_2O_2 \rightarrow 2H^+ + SiO_2 + 2e^-$

Cathode (n-type Si/Au): $H_2O_2 + 2H^+ + 2e^- \rightarrow 2H_2O$

or/and

Cathode (n-type Si/Au): $H_2O_2 + 2H^+ + 2e^- \rightarrow 2{\cdot}OH + H_2$

Moreover, a higher redox process would reinforce the electric field generated in the solution interface due to chemical gradients generated.

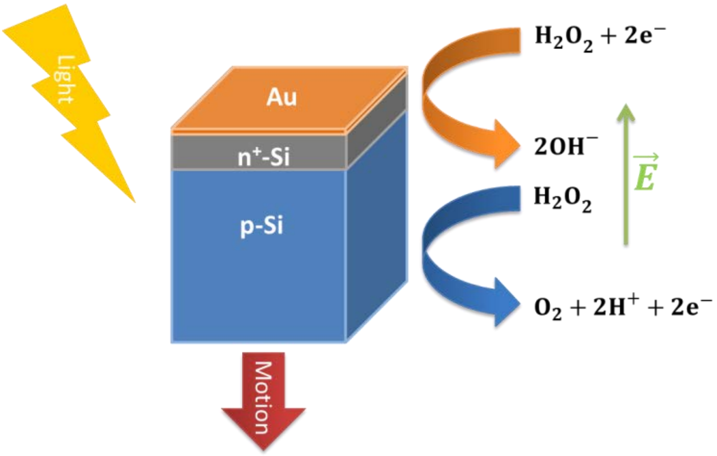

Figure 5.4 Schematic of silicon microdiode propulsion showing the generation of an electric field in the side of the electrolyte.

In microscale motors, the perimeter of the Si/Au interface is increased. This enables enhancing the redox process and the generated electric field at the Si/Au interface. In addition, Brownian's motion is remarkably decreased in the microscale, which helps in obtaining more directional propulsion.

As mentioned before, these are preliminary results and still further studies are needed to optimize the PN junction, by evaluating the dopant concentration and thickness of the dopant region, as well as comparisons with p-Si/Au and n-Si/Au. It would be useful to characterize the electric field at the junction as well as the one at the solution interface and compare with simulations. Studies with immobilized n-p Si/Au motors in a pump configuration could also be addressed to gain more insights of the photoelectrochemical actuation.

5.3 CONTAMINANT REMOVAL

To improve the efficiency of organic contaminant removal in water, we developed a Si/Fe nanomotor. As mentioned in the introduction, the iron segment provides the added value that magnetic stirring can be induced in these nanostructures through an external rotating magnetic field to favour the kinetics of contaminant degradation. Moreover, it can take advantage of both reactive oxygen species (ROS) generation from silicon photocatalytic process and from advanced oxidation processes triggered by reactive iron (Fenton reaction outlined below), and the extreme low cost compared to noble metals. The elemental iron (Fe^0) or zero-valent iron (ZVI) is a reactive metal and an effective reducing agent.[189]

The Si/Fe nanomotor consists of a silicon nanowire with 200nm in diameter and 1.5um in length and a 100nm thick Fe cap layer. In order to evaluate the performance of these Si/Fe nanowires in water contaminant degradation, we used the same BTX solution (5ppm of Benzene, Toluene and Xylene in water) as the one used in chapter 2. These photocatalytic Si/Fe nanowires were compared with polystyrene/Fe nanoparticles in which only the Fenton reaction takes place. Such comparison will allow us to decouple the photocatalytic effects mediated by Si from the Fenton reaction and have a better assessment of the Si/Fe performance. These particles were fabricated by depositing 100nm Fe cap layer on top of polystyrene nanoparticles with a diameter of 200nm. The concentrations of Si/Fe nanowires and polystyrene/Fe nanoparticles were estimated to be in the same order of magnitude (20 mg/L).

Different samples were prepared: 1) BTX solution with Si/Fe nanowires and 0.1 M NaCl with magnetic bar stirring; 2) BTX solution with Si/Fe nanowires and 0.1 M NaCl under light illumination; 3) BTX solution with Si/Fe nanowires under light illumination; 4) BTX solution with polystyrene/Fe nanoparticles and 0.1 M NaCl with magnetic bar stirring and 5) BTX solution with polystyrene/Fe nanoparticles and 0.1 M NaCl in an external rotating magnetic field (2mT). These samples were compared to a reference based on 5 ppm of BTX solution. NaCl was included in these cases in order to evaluate the salt effect on the Fenton reaction since would favour the release of Fe^{2+}.

The overnight removal rates of BTX in water under various conditions are shown in Figure 5.5. A very relevant decrease in BTX removal was observed for the samples based on Fe nanoparticles in which the Fenton reaction could be taking place. ZVI can degrade and oxidize organic compounds with the help of dissolved oxygen in water by producing hydroxyl radical (˙OH) through a group of cyclic reactions as shown below.[190]

$$Fe^0 + O_2 + 2H^+ \rightarrow Fe^{2+} + H_2O_2$$

$$Fe^0 + H_2O_2 + 2H^+ \rightarrow Fe^{2+} + 2H_2O$$

$$Fe^{2+} + H_2O_2 \rightarrow Fe^{3+} + \ \dot{\boldsymbol{O}}\boldsymbol{H} + OH^-$$

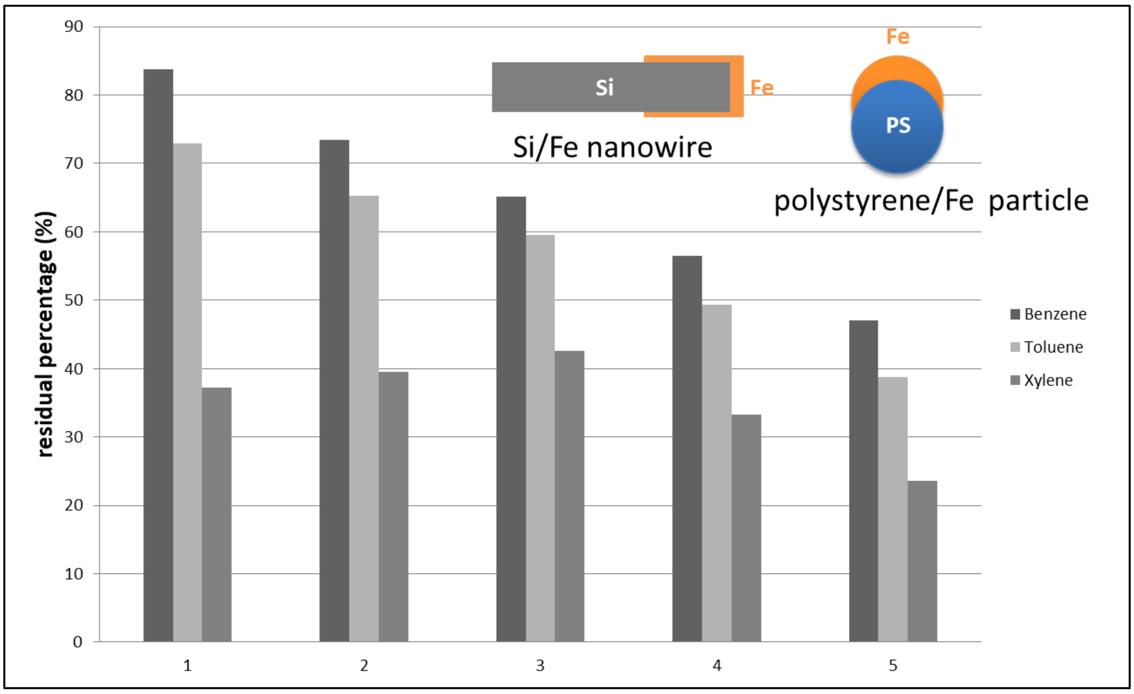

Figure 4.5 The residual percentage of benzene, toluene, and xylene after different treatments overnight. Series of treatment:

1. BTX solution with Si/Fe nanowires and 0.1 M NaCl under stirring with a magnetic bar.

2. BTX solution with Si/Fe nanowires and 0.1 M NaCl under light illumination.

3. BTX solution with Si/Fe nanowires under light illumination.

4. BTX solution with polystyrene/Fe nanoparticles and 0.1 M NaCl under stirring with a magnetic bar.

5. BTX solution with polystyrene/Fe nanoparticles and 0.1M NaCl in an external rotating magnetic field (2mT).

More than 50% of the BTX in the solution was decomposed overnight when using polystyrene/Fe nanoparticles in 0.1 M NaCl under an external magnetic field showing also the high performance of magnetic stirring in the degradation kinetics. This result with ultra-low iron concentration (20 mg/L) was quite promising compare with the ones reported in which the Fe concentration is in the range of g/L[191,192].

On the other hand, an important BTX degradation can be observed when the Si/Fe is overnight illuminated and without being subjected to external stirring but just only with the movement induced by the photochemical reaction. This finding shows that light induced reactive oxygen species (ROS) generation from silicon photocatalytic process makes a relevant contribution to the BTX destruction. It is also worth noting that adding sodium chloride is detrimental for the photochemically activated Si/Fe nanowires probably due to an increase of the photocorrosion of the Si component enhanced by the salt with the consequent degradation of their integrity and hence in their performance for the contaminant removal.

5.4 CONCLUSION

To conclude, we successfully demonstrated a light-controlled silicon microdiode micromotors, which was consistent with the results obtained with the smooth Pt/Si micropumps. The criteria to build up the light sensitive silicon based motor were established. In order to maximize separated redox interfacial reactions between Si and noble metal, an NP junction can greatly contribute by the built-in electric field to favour the hole/electron separation. Moreover, the perimeter of the interface should be large enough and the surface of noble metal smooth.

For the application of organic contaminant removal in water, we demonstrated that the elemental iron (Fe^0) or zero-valent iron (ZVI) in nanoscale is a powerful tool to destruct organic contaminants in wastewater through a Fenton reaction pathway. In the case of Si/Fe nanowires, corresponding contaminant degradation was observed under visible illumination showing an important contribution of the photocatalytic effect in the overall generation of ROS. It is also worth noting to highlight the low concentration of iron (20mg/L) that was used in our experiment to achieve more than 50% of BTX removal overnight with respect to the reported ones, which suggested a rather high efficiency of contaminant removal in our case.

6 CONCLUSIONS AND FUTURE PERSPECTIVES

6.1 CONCLUSIONS

The goal of the work was to develop photo-chemically powered silicon/metal nanomotors, to study the key physicochemical parameters controlling their performance and to analyse their potential application in organic contamination cleaning in water. Very promising organic removal nanosystems have been achieved by the end of the work. The main conclusions are summarized as follows:

- We successfully fabricated silicon nanowires as core of the nanomotors with different dimensions, different surface morphologies, and different porosities.
- Significant directional motion was observed at the sputtered Pt/Si nanomotors with recorded maximum speed at 31 µm/s in the presence of 1%wt H_2O_2. However, scarce directional motion was captured for nanomotors with Pt evaporated by e-beam deposition. Moreover, negligible dependence of light wavelength and intensity on swimmer motion was observed.
- We demonstrated that there are two competing propulsion mechanisms under visible light irradiation at the Pt/Si pump configuration. One is driven by an electro-osmotic process stemmed from a photoactivation reaction of H_2O_2 decomposition mediated by Si as anode and Pt as cathode. The other one is not light responsive and is triggered by the redox decomposition of H_2O_2 exclusively at the Pt surface. Indications of such competitive mechanism were obtained when performing contaminant degradation experiments with Si/Pt nanomotors. However such output was thoroughly proved by comparing Si/Pt pumps with rough Pt (evaporated by sputtering) and smooth Pt (evaporated by electron-beam). We showed that the actuation mechanism of the Pt/Si pump can be switched from light-controlled electrokinetics to light-insensitive diffusio-osmosis by only increasing the metal surface roughness.
- We could not reach conclusive results on the nature and location of the photochemical reaction at the Si/Pt pumps in contact with condensed water by probing the chemical states of Si/Pt through Near-Ambient Pressure Photoemission (NAPP) with synchrotron radiation. Strong beam effects masked the photochemical reactions mediated by water with visible light and hence their corresponding chemical changes in the photoemission characteristics of the Si/Pt system. Conventional XPS measurements only provided very weak indications of reduced Pt species at Si/Pt edge as compared to other Pt regions. The role of external illumination was not conclusive.

- We successfully demonstrated a light-controlled silicon microdiode motor with a smooth gold cap layer, which helped to establish guidelines for optimizing photoelectrochemically driven Si/metal swimmers. These preliminary results suggested that a PN junction with the generated built-in electric field can favor the hole/electron separation and hence the photoelectrochemical redox reactions at the anode and cathode of the microdiode, and strengthening the electric field at the solution interface. Moreover, the larger perimeter of the Si/metal edge provided by the microscale range together with the smooth surface characteristics of the Au cap could enhance the photochemical separated redox interfacial reactions between Si and noble metal.
- Silicon/zero-valent iron (ZVI) nanosystems have demonstrated relevant organic degradation performance under visible light illumination showing an important contribution of the photocatalytic effect in the overall generation of ROS apart from the contribution provided by the Fenton reaction. Furthermore zero-valent iron/polystyrene nanoparticles have shown a very significant decontamination performance via Fenton reactions enhanced by the presence of salts and external magnetic fields.

6.2 FUTURE PERSPECTIVES

Silicon based photocatalytic micro-/nanomotors hold great potential for future practical applications, however there is still plenty of room for further improvement and optimization.

Within the thesis, we have demonstrated that various parameters (metal layer roughness, aspect ratio of the motor, silicon heterojunction) influenced the propulsion mechanisms of the silicon swimmers. Further optimizations are needed to achieve the most efficient photocatalytic motion under visible and/or NIR light illumination. There are many fundamental issues still unsettled on the Si/metal devices that need to be addressed such as the photochemical reaction pathway and location. To probe the chemical pathways within Pt/Si motor configuration in aqueous solution, further studies could be accomplished using local probe microscopies. Furthermore, better understanding of the oxygen plasma activation is still needed to study the impact of oxygen components on Si and Pt under light illumination. In addition, salt or ionic effects on Si/Pt motion when triggered by diffusiophoretic mechanisms should be elucidated in future study.

We have achieved encouraging results with the silicon based microdiode capped with gold as light driven motors. The introduction of np junctions seems to be a very promising strategy to enhance the photochemically driven motion, but a lot of work is still needed to optimize their performance by a thorough assessment of the dopant concentration and thickness of the dopant region, the built-in electric field at the n-p junction and the electric field at the liquid stemming from the photochemical reactions. Studies with immobilized n-p Si/Au motors in a pump configuration together with numerical simulations could also be addressed to gain more insights of the photoelectrochemical actuation.

In the last section of this thesis we have seen that zero valent iron based nanomotors are promising low cost candidates with capabilities for a powerful organic decomposition even at very low concentration of nanowires/nanoparticles. More work is still needed to understand electrochemical reactions between iron and silicon and to explore photo-activated Fenton reactions for degradation of organic pollutants. In addition, the introduction of magnetic segments to induce magnetic stirring for increasing degradation kinetics still needs to be widely exploited. Moreover, other low-cost catalyst materials with photochemical or Fenton capabilities for ROS production can be also pursued such as ferrites, copper oxides or MnO_2. From the point of view of realistic applications low-cost chemical routes, as well as the concepts of scalability, recovery and reusability could be approached in the future for this kind of devices. In addition, fuel is also a key aspect to consider for practical environmental applications. Chemicals or fuels for silicon based micro-/nanomotors are still rather limited. Fuels with high propulsion efficiency and compatibility should be developed in the future work. The ideal fuel could be just water or the pollutant in water itself for practical application.

Accordingly, many efforts are still needed to explore some unsettled issues in the physicochemical fundamentals of this topic as well as in the development of real applications. We have provided some promising nanosystems that need to be optimized and exploited, thus guaranteeing the continuity of this research topic.

7 APPENDIX: MATERIALS AND METHODS

7.1 SILICON NANOMOTOR FABRICATION

Our novel motor consists of silicon nanowire and noble metal cap layer. The silicon nanowire (Si NW) is fabricated using colloidal lithography followed by metal-assisted chemical etching (MACE). The noble metal (platinum or gold in this work) is coated by electron beam evaporation or sputtering. Figure 7.1 shows the process flow of the silicon nanomotor fabrication.

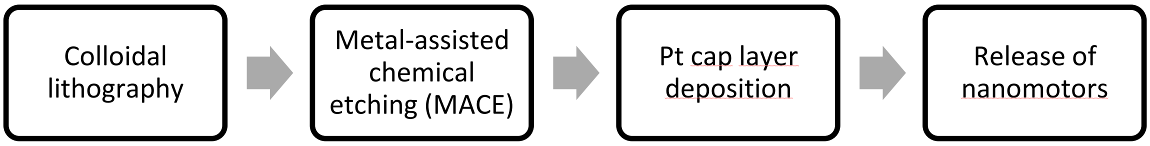

Figure 7.1. The process flow of the silicon nanomotor fabrication

7.1.1 COLLOIDAL LITHOGRAPHY

The fabrication starts with colloidal lithography, which means patterning surface with monolayers of colloidal particles. The non-close packed colloidal pattern is prepared as the template for the subsequent metal assisted chemical etching of silicon substrate to obtain vertically aligned silicon nanowire array.

Two approaches of colloidal lithography are developed within this work. The first one starts with the formation of hexagonal close-packed polystyrene sphere monolayers at air/water interface as shown in figure 7.2. The as-received polystyrene sphere of 400nm in diameter from Sigma-Aldrich is diluted by ethanol at a ratio of 1:1. This mixture is sonicated for several minutes and continuously injected onto the Milli-Q water surface through the precisely controlled syringe pump system at a rate of 5 µL/min. The tip of the needle is strictly positioned to be exact in contact with the water surface. The driving force for the spreading of polystyrene nanospheres is associated with the Marangoni effect, a mass transfer along the interface between two fluids as a result of surface tension gradient.[193] Once the hexagonal close packed pattern is formed on the entire water surface, the water is drained from the bottom of the Teflon bath slowly and ultimately the polystyrene monolayer is transferred to 4 inch silicon substrate underneath. It is worth noting that the silicon wafer is place on a slightly tilted holder (5 degree) at the bottom of the Teflon bath, which facilitates water draining and polystyrene monolayer transfer.

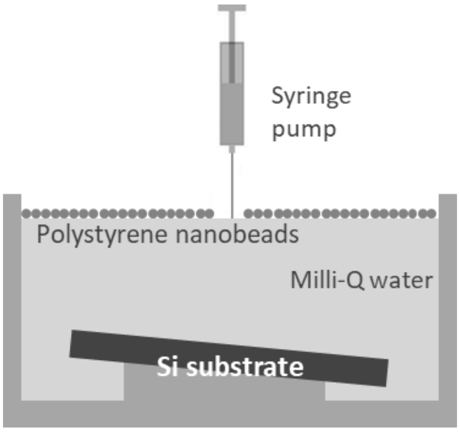

Figure 7.2 Schematic of the process to achieve close packed polystyrene nanobeads self-assembly on a silicon wafer

The 400nm self-assembly polystyrene nanospheres are reduced by size isotropically using oxygen gas Reactive Ion Etching (RIE, 2000 CE from South Bay Technology Inc.). The reduced diameter ranging from 100 to 300 nm is controlled by etching time. One SEM image after RIE is shown in Figure 7.3.

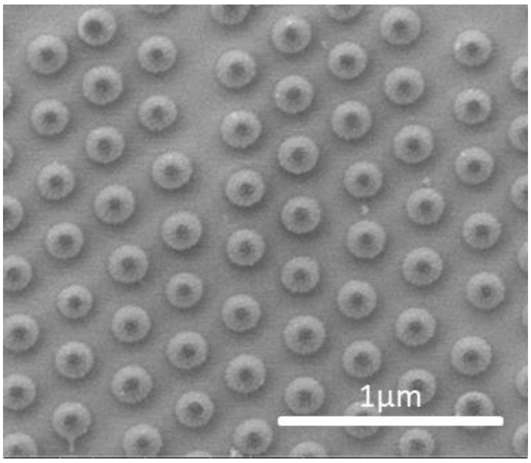

Figure 7.3 SEM image of etched polystyrene nanospheres

Another method we developed to achieve non-close packed pattern is based on electrostatic deposition of silica nanospheres on silicon substrate. The process flow is illustrated in figure 7.4 below. At first the silicon substrate is treated by oxygen plasma using PVA Tepla PS-210 microwave plasma etcher for 5 min at power of 400W to remove surface contaminants and activate surface by introducing negative surface charges. The negative charged silicon surface is coated by poly(diallyldimethylammonium chloride) solution (PDDA, 0.1 wt% from Sigma Aldrich), which is a positive polyelectrolyte, for 1 minute. The wafer is then rinsed in Milli-Q water and blown dry by N2 gas. The 1% negative charged silica colloidal solution with 100nm in diameter is dropped on the surface afterwards. Due to the attractive electrostatic forces between positive charged PDDA layer and negative charged silica colloids, the silica nanobeads are attached to the surface. In the meantime, the repulsive forces among the silica particles promote a short range order monolayer on the silicon substrate. Finally the wafer is rinsed in Milli-Q water to remove extra silica particles and it is dried by critical point drying to preserve non-close silica pattern on the surface.

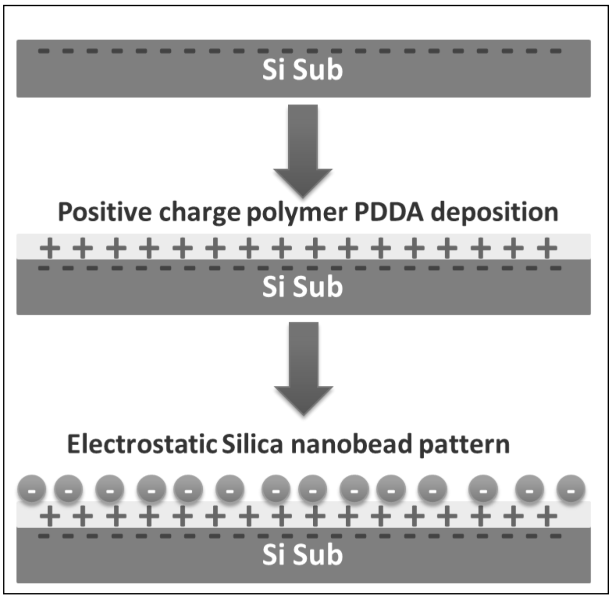

Figure 7.4 Schematic of the process to achieve non-close packed silica nanobeads self-assembly on a silicon wafer

Figure 7.5 shows an example of a non-closed packed pattern of silica nanobeads with 100nm in diameter using the electrostatic deposition approach described above.

The PDDA layer between silicon substrate and silica nanobeads needs to be removed by PVA Tepla PS-210 microwave plasma etcher for 5 min at power of 400W. This step is required for the following MACE process to achieve direct contact between silicon substrate and deposited metal thin film.

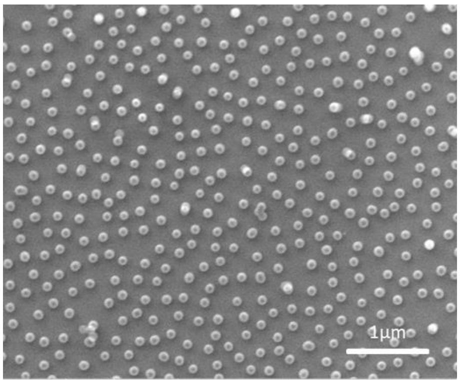

Figure 7.5 SEM image of a non-closed packed pattern of silica nanobeads with 100nm in diameter

7.1.2 METAL-ASSISTED CHEMICAL ETCHING (MACE)

The first report of metal-assisted chemical etching of Si was reported by Malinovska et al. in 1997.[194] In the MACE procedure, a Si substrate partly covered by a noble metal (gold in this work) is immersed in an etchant composed of HF acid and an oxidative agent (H_2O_2 in this work). The Si under the noble metal is etched much faster than the Si where is not covered by the noble metal. As a result, the geometry of metal template is transferred to the silicon substrate underneath while the etching process is going vertically. The process flow of fabrication of silicon nanowire array by MACE is indicated in figure 7.6.

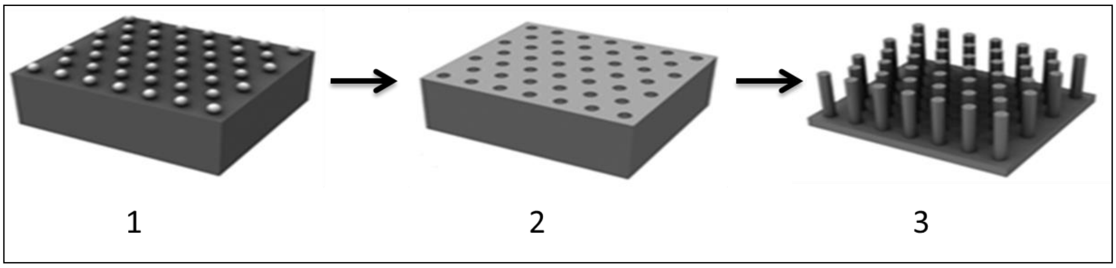

Figure 7.6 The process flow of fabrication of silicon nanowire array by MACE. 1. Non-close packed colloidal pattern. It is employed as the mask for gold mesh deposition. 2. Gold layer deposition and

colloidal lift-off to form gold mesh on silicon substrate. 3. Fabrication of vertically aligned silicon nanowire array by MACE in HF/H_2O_2 solution.

In this work, a gold (Au) thin layer ranging from 20 to 50 nm, which depends on the diameter of nanobeads, is evaporated on the patterned surface by electron beam evaporation (AJA UHV model ATC ORION). A 1nm titanium (Ti) thin film is coated as an adhesive layer between silicon substrate and gold layer. The nanobeads are peeled off from the substrate by adhesive tape afterwards. The remaining gold mesh on Si substrate is then cleaned by oxygen plasma, which can be used as the template for fabrication of silicon nanowire array. The sample is immersed in the mixture of HF/H_2O_2 aqueous solution. The length of Silicon nanowire is controlled by the immersion time and the diameter is determined by the size of nanobeads in the previous colloidal lithography step. The sample is rinsed in Milli-Q water to terminate the wet chemical etching when the desired length is achieved. In order to preserve the high aspect ratio of the nanowire array during drying process, the rinsed samples are transferred to isopropyl alcohol (IPA) bath before blown dry by nitrogen. Figure 7.7 shows SEM images of Si nanowire array with different diameters.

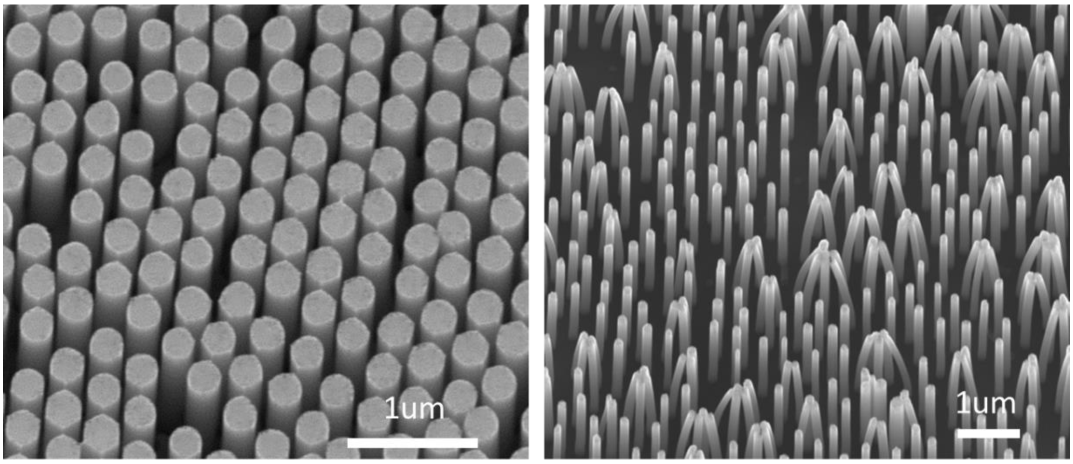

Figure 7.7 SEM images of Si nanowire array with different diameters. Left: 300nm in diameter. Right: 100nm in diameter.

Silicon nanowire arrays with higher porosity can be developed by adding an extra thin film of silver on the top of the gold layer during the electron beam evaporation. When the sample is dipped in the MACE etchant, part of the brittle silver layer will peel off and turn into nanoparticles in the solution. As long as these silver nanoparticles attach to the sidewalls of the nanowires, the chemical etching of silicon starts locally. Thus, the porosity of silicon nanowire can be modulated by introducing a silver layer. Figure 7.8 shows one example of porous silicon nanowire array with 200 nm in diameter.

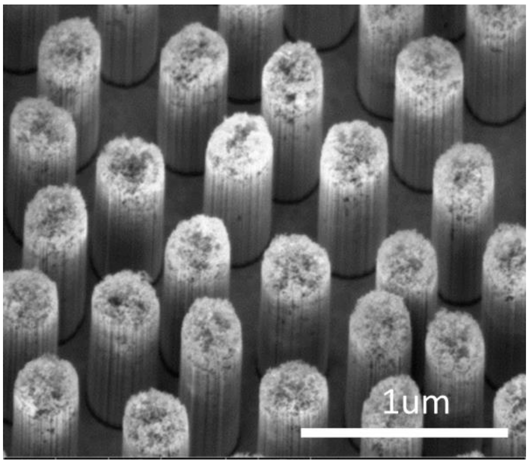

Figure 7.8 SEM image of porous silicon nanowire array with 200 nm in diameter.

We also further modify silicon nanowire top morphology by site-selective deposition of silver nanoclusters on the top of nanowire tuning etching anisotropy.[195] Figure 7.9 illustrates SEM images of the modified top morphologies by modulating the relative concentration in the [$AgNO_3$ + HF + HNO_3/H_2O_2] etching system.

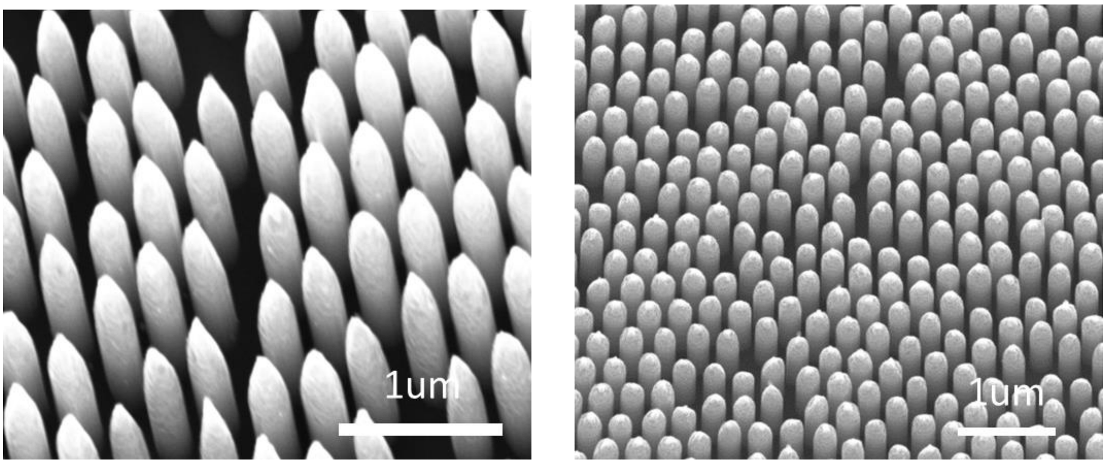

Figure 7.9 SEM images of the modified top morphologies.

7.1.3 PLATINUM CAP LAYER DEPOSITION AND RELEASE OF NANOMOTORS

A platinum cap layer is deposited on the vertically aligned silicon nanowire array by electron beam evaporation with sample perpendicular to platinum source (AJA UHV model ATC ORION, directional source beam) and by sputtering with a tilted angle (Leica EM ACE200, non-directional source beam). The schematic of tilted Pt coating is shown in figure 7.10. In this case, the closest neighbour nanowires can play as the mask for the central one during the deposition process and thus the coating on the side wall of the nanowire is minimized.

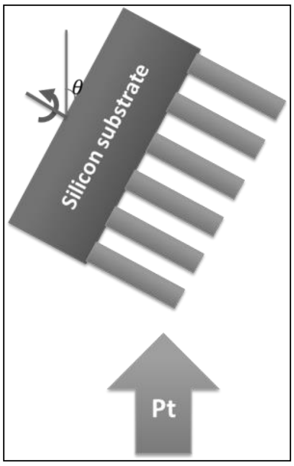

Figure 7.10 Schematics of the tilted Pt sputtering. Multiple depositions are carried out and the sample is rotated manually after each run to achieve a homogeneous thin film on the top of nanowire array.

The final step of silicon nanomotor fabrication is to suspend it in water from the substrate by ultra-sonication. A bath of several minutes in the ultrasonic cleaner (Elmasonic S30, 37kHz) is usually sufficient to release silicon nanomotors. However, in the case of some dense silicon nanowire arrays, the probe sonicator (Qsonica Q55) is required to generate concentrated sonic waves on the sample surface to release nanomotors. The evaporated and sputtered samples after sonication suspension are shown in figure 7.11 below.

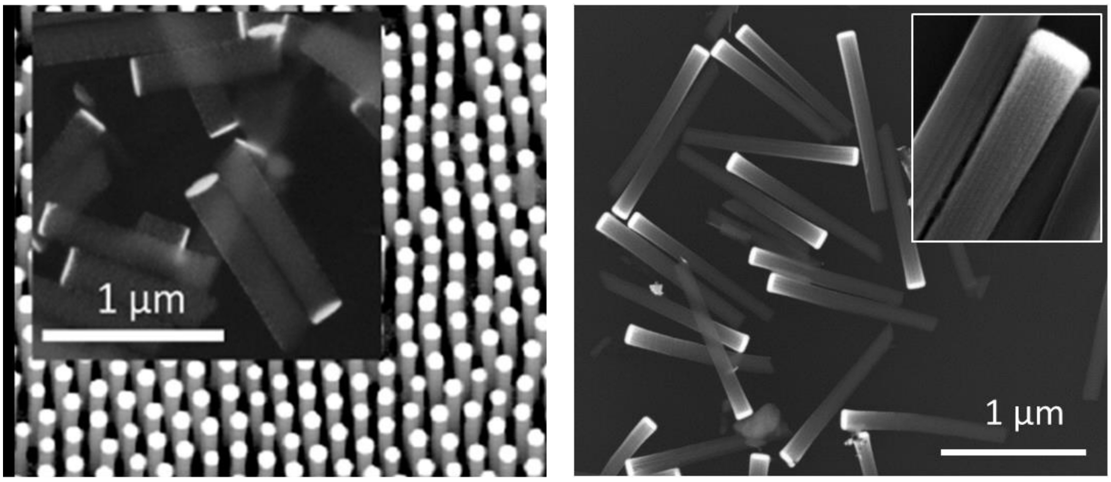

Figure 7.11 SEM images of the evaporated and sputtered samples after sonication suspension. Left: evaporated platinum sample array with inset of suspended silicon nanomotors (1µm in length and 200 nm in diameter). Right: sputtered platinum silicon nanomotors with 1µm in length and 200nm in diameter after suspension with inset of the zoom-in view of top platinum layer.

7.1.4 NANOMOTOR TRACKING

The suspended silicon nanomotor propulsion behaviour is tracked under optical microscopes in a 1%wt H_2O_2 solution. Zeiss Axio Observer Z1m optical microscope, with a polychromatic light source and long working distance objectives (5X, 10X, 20X, 50X and 100X), is used to perform the experiment at different light intensities. TSC SP5 Leica confocal microscope, with an AOBS (Acousto-optical Beam splitter) and monochromatic laser sources in scanning mode, is employed to investigate Si nanomotor motions at different wavelengths and intensities.

The captured video is analysed by software Imaris[196], and the motion trajectories are plotted using the autoregressive motion algorithm designed for continuous movement in Imaris. Normal directional trajectories with more than 5um length are selected for mean velocity calculations.

7.2 PUMP FABRICATION AND TRACKING

The silicon/platinum pump consists of a platinum disk on a silicon substrate. It can be considered an immobilized silicon motor and a counterpart to study the propulsion mechanism of the photocatalytic nanoswimmers.

In this work, pumps are fabricated by patterning Pt discs with a diameter of 50 µm and a thickness of 50 nm on p-doped silicon surfaces (10-20 ohm cm) by electron beam lithography, followed by platinum deposition either by electron beam evaporation (AJA UHV model ATC ORION) or sputtering (Leica EM ACE200). In the case of the electron beam evaporation, a very thin adhesion layer of chromium is deposited between the metal disc and the silicon substrate.

The detailed fabrication process of Si/Pt micropump is described below. At first a 2cm by 2cm silicon substrate is cleaned with acetone and IPA in a sonication bath respectively. After the surface is blown dry by nitrogen, a double PMMA layer with different molecular weights (950K and 495K from Microchem) is deposited on top by spin coating as shown in step 1 of figure 7.12. After electron beam exposure using Inspect F50 from FEI and PMMA development in a 1:3 mixture of methyl isobutyl ketone (MIBK) and IPA, an undercut profile of the PMMA resists is formed as shown in step 2. In such a structure, coating the sidewall of the resist can be avoided when Pt is evaporated in step 3. Thus, the well-defined micropump with smooth edge can be achieved after the lift-off process in acetone sonication bath.

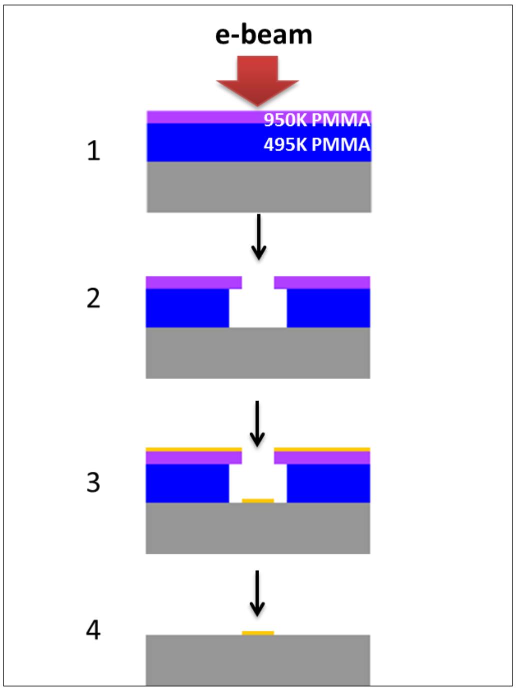

Figure 7.12 Process flow of silicon micropump fabrication. 1. e-beam exposure on PMMA resist. 2. PMMA development in a mixture of MIBK and IPA. 3. Pt deposition by e-beam evaporation or sputtering. 4. Lift-off process in acetone sonication bath.

The fabricated pump is investigated under Nikon Eclipse LV100 optical microscope. The fluid motion is followed by tracking the motion of colloidal particles with different surface charges in 1%wt H_2O_2 solution, the same concentration as in the case of nanomotor tracking.

The recorded tracer motion video is converted into image series with the help of software iWisoft. The object tracking software Diatrack[197] is used to analyse the images and calculate the mean velocity of the colloidal particles.

7.3 CHEMICAL ANALYSIS TECHNIQUES FOR CONTAMINANT REMOVAL

The mixture of benzene, toluene, and xylene (BTX) is applied as reference to evaluate the capability of our silicon nanomotors to decompose organic contaminants in water. Gas chromatography with flame ionization detector (GC-FID) is employed to measure the concentration of BTX solution after adding the silicon nanomotors into the solution.

Gas chromatography (GC) is a widely used technique for qualitative and quantitative chemical compound analysis. The basic components of a typical equipment to perform GC are shown in Figure 7.13. It mainly consists of carrier gas system, sample injection system, column, and chromatographic detector.

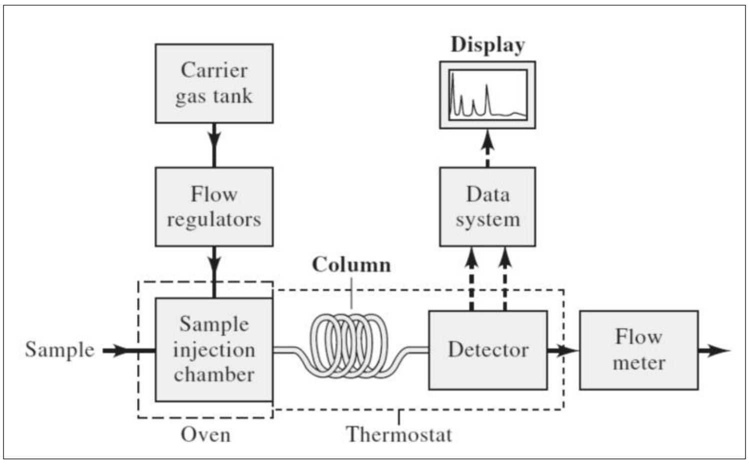

Figure 7.13 Block diagram of a typical gas chromatograph.[186]

The flame ionization detector (FID) is the most widely used and generally applicable detector for GC. With a FID, as shown in Figure 7.14, effluent from the column is directed into a small air/hydrogen flame. Most organic compounds produce ions and electrons when pyrolyzed at the temperature of an air/hydrogen flame. These compounds are detected by monitoring the current produced by collecting the ions and electrons. A voltage applied between the burner tip and the collector electrode located above the flame is used to collect the ions and electrons. The resulting current is then measured with a sensitive picoammeter. The number of ions produced is approximately proportional to the number of reduced carbon atoms in the flame. As the FID takes responses to the number of carbon atoms entering the detector per unit of time, it is a mass sensitive chromatographic detector with a high sensitivity (10^{-13} g/s), which is independent from the effect of flow rate changes of the carrier gas.[198]

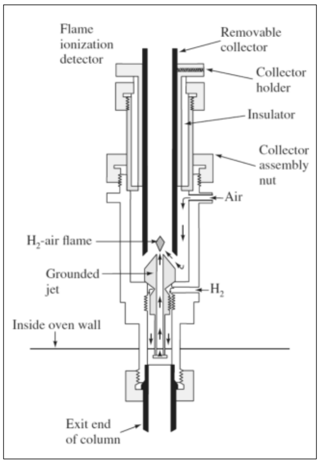

Figure 7.14 A typical flame ionization detector from Agilent Technologies. [186]

7.4 SURFACE ANALYSIS TECHNIQUES

7.4.1 X-RAY PHOTOELECTRON SPECTROSCOPY (XPS)

X-ray photoelectron spectroscopy (XPS) is employed as the quantitative method to analyse surface chemical composition. The schematic of XPS measurement is shown in figure 7.15. When the sample is irradiated with a beam of x-ray, the kinetic energy and number of electrons that escape from the surface of the material are collected in ultrahigh vacuum (UHV). The electron binding energy $E_B^F(k)$ as illustrated in figure 7.15 is measured in the experiment. It is defined as:

$$E_B^F(k) = h\nu - E_{kin} - \phi_{spec}$$

where $E_B^F(k)$ is the binding energy referred to the Fermi level, $h\nu$ is photon energy, E_{kin} is kinetic energy and ϕ_{spec} is spectrometer work function.

The binding energy is influenced by the chemical surroundings, which makes XPS suitable for determining chemical states. In addition, XPS is surface sensitive because the emitted photoelectrons originate from the upper 0.5–5 nm of the sample, despite the deeper penetration of the primary X-rays compared to a primary electron beam.[199]

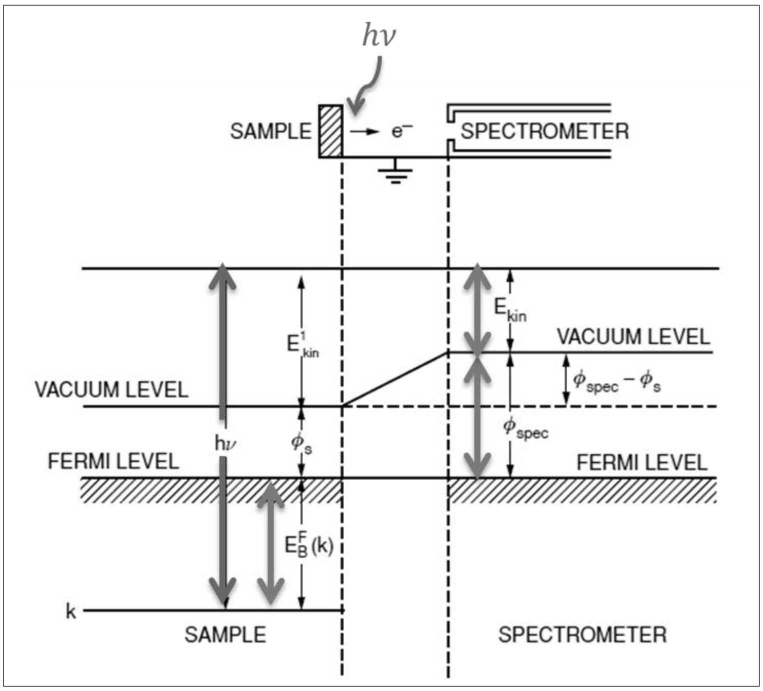

Fiugue 7.15 The schematic of XPS measurement

Within this work, a Perkin Elmer PHI 5500 XPS system with monochromatic Al X-ray source (1486.6eV) is applied to perform the measurement in ultra-high vacuum (10^{-10} mbar). Analysed depth is 10 nm. XPS data is analysed with CasaXPS.

7.4.2 NEAR-AMBIENT PRESSURE PHOTOEMISSION (NAPP)

Compared to conventional XPS in UHV, a differential pumping system equipped with electrostatic lenses (see in figure 7.16) is employed in near-ambient pressure XPS to collect a substantially larger fraction of escaped electrons that would otherwise be lost due to the scattering with gas molecules in near-ambient pressure.[200]

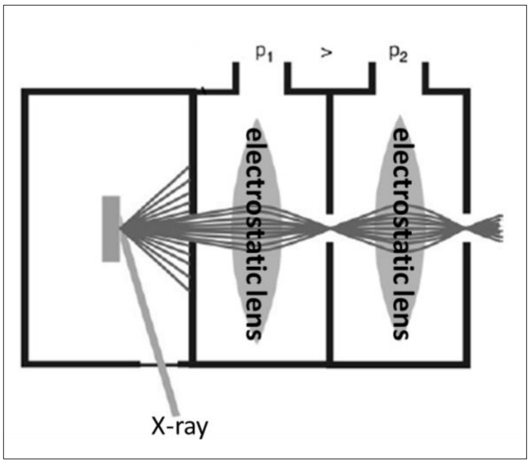

Figure 7.16 schematic of a typical near-ambient pressure XPS system

In this work, Near-Ambient Pressure Photoemission (NAPP) is employed to study the silicon/platinum interface in water ambient. It was performed at the NAPP endstation of the CIRCE beamline at the ALBA synchrotron.

The NAPP endstation consists of a load lock chamber, a sample preparation chamber and an analysis chamber for the XPS measurements in UHV or in the presence of different gases with pressures up to 20 mbar. The XPS analyser is a PHOIBOS 150 NAP.[201]

BIBLIOGRAPHY

[1] https://en.wikipedia.org/wiki/Biomimetics

[2] https://en.wikipedia.org/wiki/There%27s_Plenty_of_Room_at_the_Bottom#cite_note-1

[3] Ozin, G. a.; Manners, I.; Fournier-Bidoz, S.; Arsenault, A. Dream Nanomachines. *Adv. Mater.* **2005**, *17* (24), 3011–3018.

[4] Eskandarloo, H.; Kierulf, A.; Abbaspourrad, A. Nano- and Micromotors for Cleaning Polluted Waters: Focused Review on Pollutant Removal Mechanisms. *Nanoscale* **2017**, *9* (37), 13850–13863.

[5] Purcell, E. M. Life at Low Reynolds Number. *Am. J. Phys.* **1977**, *45* (1), 3–11.

[6] Falkovich, G. Fluid Mechanics. Cambridge University Press. **2011**.

[7] Lauga, E. Enhanced Diffusion by Reciprocal Swimming. *Phys. Rev. Lett.* **2011**, *106* (17), 178101.

[8] Santiago, I. Nanoscale Active Matter Matters: Challenges and Opportunities for Self-Propelled Nanomotors. *Nano Today* **2018**, *19*, 11–15.

[9] Wang, J.; Manesh, K. M. Motion Control at the Nanoscale. *Small* **2010**, *6* (3), 338–345.

[10] Wong, F.; Sen, A. Progress toward Light-Harvesting Self-Electrophoretic Motors: Highly Efficient Bimetallic Nanomotors and Micropumps in Halogen Media. *ACS Nano* **2016**, *10* (7), 7172–7179.

[11] Dey, K. K.; Wong, F.; Altemose, A.; Sen, A. Catalytic Motors-Quo Vadimus? *Curr. Opin. Colloid Interface Sci.* **2015**, *21*, 4–13.

[12] Paxton, W. F.; Kistler, K. C.; Olmeda, C. C.; Sen, A.; St. Angelo, S. K.; Cao, Y.; Mallouk, T. E.; Lammert, P. E.; Crespi, V. H. Catalytic Nanomotors: Autonomous Movement of Striped Nanorods. *J. Am. Chem. Soc.* **2004**, *126* (41), 13424–13431.

[13] Fournier-Bidoz, S.; Arsenault, A. C.; Manners, I.; Ozin, G. a. Synthetic Self-Propelled Nanorotors. *Chem. Commun.* **2005**, No. 4, 441–443.

[14] Anderson, J. L. Colloid Transport by Interfacial Forces. *Annu. Rev. Fluid Mech.* **1989**, *21* (1), 61–99.

[15] Solomentsev, Y.; Anderson, J. L. Electrophoresis of Slender Particles. *J. Fluid Mech.* **1994**, *279* (-1), 197.

[16] Hong, Y.; Velegol, D.; Chaturvedi, N.; Sen, A. Biomimetic Behavior of Synthetic Particles: From Microscopic Randomness to Macroscopic Control. *Phys. Chem. Chem. Phys.* **2010**, *12* (7), 1423–1435.

[17] Paxton, W. F.; Kistler, K. C.; Olmeda, C. C.; Sen, A.; St. Angelo, S. K.; Cao, Y.; Mallouk, T. E.; Lammert, P. E.; Crespi, V. H. Catalytic Nanomotors: Autonomous Movement of Striped Nanorods. *J. Am. Chem. Soc.* **2004**, *126* (41), 13424–13431.

[18] Laocharoensuk, R.; Burdick, J.; Wang, J. Carbon-Nanotube-Induced Acceleration of Catalytic Nanomotors. *ACS Nano* **2008**, *2* (5), 1069–1075.

[19] Liu, R.; Sen, A. Autonomous Nanomotor Based on Copper–Platinum Segmented Nanobattery. *J. Am. Chem. Soc.* **2011**, *133* (50), 20064–20067.

[20] Wang, Y.; Hernandez, R. M.; Bartlett, D. J.; Bingham, J. M.; Kline, T. R.; Sen, A.; Mallouk, T. E. Bipolar Electrochemical Mechanism for the Propulsion of Catalytic Nanomotors in Hydrogen Peroxide Solutions †. *Langmuir* **2006**, *22* (25), 10451–10456.

[21] Wheat, P. M.; Marine, N. A.; Moran, J. L.; Posner, J. D. Rapid Fabrication of Bimetallic Spherical Motors. *Langmuir* **2010**, *26* (16), 13052–13055.

[22] Lee, T.-C.; Alarcón-Correa, M.; Miksch, C.; Hahn, K.; Gibbs, J. G.; Fischer, P. Self-Propelling Nanomotors in the Presence of Strong Brownian Forces. *Nano Lett.* **2014**, *14* (5), 2407–2412.

[23] Ibele, M. E.; Lammert, P. E.; Crespi, V. H.; Sen, A. Emergent, Collective Oscillations of Self-Mobile Particles and Patterned Surfaces under Redox Conditions. *ACS Nano* **2010**, *4* (8), 4845–4851.

[24] Wang, W.; Duan, W.; Ahmed, S.; Mallouk, T. E.; Sen, A. Small Power: Autonomous Nano- and Micromotors Propelled by Self-Generated Gradients. *Nano Today* **2013**, *8* (5), 531–554.

[25] Howse, J. R.; Jones, R. A. L.; Ryan, A. J.; Gough, T.; Vafabakhsh, R.; Golestanian, R. Self-Motile Colloidal Particles: From Directed Propulsion to Random Walk. *Phys. Rev. Lett.* **2007**, *99* (4), 048102.

[26] Ke, H.; Ye, S.; Carroll, R. L.; Showalter, K. Motion Analysis of Self-Propelled Pt–Silica Particles in Hydrogen Peroxide Solutions. *J. Phys. Chem. A* **2010**, *114* (17), 5462–5467.

[27] Baraban, L.; Tasinkevych, M.; Popescu, M. N.; Sanchez, S.; Dietrich, S.; Schmidt, O. G. Transport of Cargo by Catalytic Janus Micro-Motors. *Soft Matter* **2012**, *8* (1), 48–52.

[28] Zhang, H.; Duan, W.; Liu, L.; Sen, A. Depolymerization-Powered Autonomous Motors Using Biocompatible Fuel. *J. Am. Chem. Soc.* **2013**, *135* (42), 15734–15737.

[29] Gao, W.; Pei, A.; Dong, R.; Wang, J. Catalytic Iridium-Based Janus Micromotors Powered by Ultralow Levels of Chemical Fuels. *J. Am. Chem. Soc.* **2014**, *136* (6), 2276–2279..

[30] Brown, A.; Poon, W. Ionic Effects in Self-Propelled Pt-Coated Janus Swimmers. *Soft Matter* **2014**, *10* (22), 4016–4027.

[31] Sengupta, S.; Ibele, M. E.; Sen, A. Fantastic Voyage: Designing Self-Powered Nanorobots. *Angew. Chem. Int. Ed. Engl.* **2012**, *51* (34), 8434–8445.

[32] Yadav, V.; Duan, W.; Butler, P. J.; Sen, A. Anatomy of Nanoscale Propulsion. *Annu. Rev. Biophys.* **2015**, *44* (1), 77–100.

[33] Sanchez, S.; Ananth, A. N.; Fomin, V. M.; Viehrig, M.; Schmidt, O. G. Superfast Motion of Catalytic Microjet Engines at Physiological Temperature. *J. Am. Chem. Soc.* **2011**, *133* (38), 14860–14863.

[34] Gao, W.; Sattayasamitsathit, S.; Orozco, J.; Wang, J. Highly Efficient Catalytic Microengines: Template Electrosynthesis of Polyaniline/Platinum Microtubes. *J. Am. Chem. Soc.* **2011**, *133* (31), 11862–11864.

[35] Solovev, A. A.; Mei, Y.; Bermúdez Ureña, E.; Huang, G.; Schmidt, O. G. Catalytic Microtubular Jet Engines Self-Propelled by Accumulated Gas Bubbles. *Small* **2009**, *5* (14), 1688–1692.

[36] Mei, Y.; Huang, G.; Solovev, A. A.; Ureña, E. B.; Mönch, I.; Ding, F.; Reindl, T.; Fu, R. K. Y.; Chu, P. K.; Schmidt, O. G. Versatile Approach for Integrative and Functionalized Tubes by Strain Engineering of Nanomembranes on Polymers. *Adv. Mater.* **2008**, *20* (21), 4085–4090.

[37] Harazim, S. M.; Xi, W.; Schmidt, C. K.; Sanchez, S.; Schmidt, O. G. Fabrication and Applications of Large Arrays of Multifunctional Rolled-up SiO/SiO2 Microtubes. *J. Mater. Chem.* **2012**, *22* (7), 2878–2884.

[38] Soler, L.; Martínez-Cisneros, C.; Swiersy, A.; Sánchez, S.; Schmidt, O. G. Thermal Activation of Catalytic Microjets in Blood Samples Using Microfluidic Chips. *Lab Chip* **2013**, *13* (22), 4299.

[39] Solovev, A. A.; Xi, W.; Gracias, D. H.; Harazim, S. M.; Deneke, C.; Sanchez, S.; Schmidt, O. G. Self-Propelled Nanotools. *ACS Nano* **2012**, *6* (2), 1751–1756.

[40] Agrawal, A.; Dey, K. K.; Paul, A.; Basu, S.; Chattopadhyay, A. Chemical Locomotives Based on Polymer Supported Catalytic Nanoparticles. *J. Phys. Chem. C* **2008**, *112* (8), 2797–2801.

[41] Gao, W.; Pei, A.; Wang, J. Water-Driven Micromotors. *ACS Nano* **2012**, *6* (9), 8432–8438.

[42] Manjare, M.; Yang, B.; Zhao, Y.-P. Bubble Driven Quasioscillatory Translational Motion of Catalytic Micromotors. *Phys. Rev. Lett.* **2012**, *109* (12), 128305.

[43] Mou, F.; Chen, C.; Ma, H.; Yin, Y.; Wu, Q.; Guan, J. Self-Propelled Micromotors Driven by the Magnesium-Water Reaction and Their Hemolytic Properties. *Angew. Chemie Int. Ed.* **2013**, *52* (28), 7208–7212.

[44] Gao, W.; D'Agostino, M.; Garcia-Gradilla, V.; Orozco, J.; Wang, J. Multi-Fuel Driven Janus Micromotors. *Small* **2013**, *9* (3), 467–471.

[45] Esplandiu, M. J.; Zhang, K.; Fraxedas, J.; Sepulveda, B.; Reguera, D. Unraveling the Operational Mechanisms of Chemically Propelled Motors with Micropumps. *Acc. Chem. Res.* **2018**, *51* (9), 1921–1930.

[46] Farniya, A. A.; Esplandiu, M. J.; Reguera, D.; Bachtold, A. Imaging the Proton Concentration and Mapping the Spatial Distribution of the Electric Field of Catalytic Micropumps. *Phys. Rev. Lett.* **2013**, *111* (16), 168301.

[47] Esplandiu, M. J.; Afshar Farniya, A.; Reguera, D. Key Parameters Controlling the Performance of Catalytic Motors. *J. Chem. Phys.* **2016**, *144* (12), 124702.

[48] Paxton, W. F.; Baker, P. T.; Kline, T. R.; Wang, Y.; Mallouk, T. E.; Sen, A. Catalytically Induced Electrokinetics for Motors and Micropumps. *J. Am. Chem. Soc.* **2006**, *128* (46), 14881–14888.

[49] Dong, R.; Cai, Y.; Yang, Y.; Gao, W.; Ren, B. Photocatalytic Micro/Nanomotors: From Construction to Applications. *Acc. Chem. Res.* **2018**, *51* (9), 1940–1947.

[50] Zhang, Q.; Dong, R.; Wu, Y.; Gao, W.; He, Z.; Ren, B. Light-Driven Au-WO3@C Janus Micromotors for Rapid Photodegradation of Dye Pollutants. *ACS Appl. Mater. Interfaces* **2017**, *9* (5), 4674–4683.

[51] Li, Y.; Mou, F.; Chen, C.; You, M.; Yin, Y.; Xu, L.; Guan, J. Light-Controlled Bubble Propulsion of Amorphous TiO_2 /Au Janus Micromotors. *RSC Adv.* **2016**, *6* (13), 10697–10703.

[52] Li, Y.; Mou, F.; Chen, C.; You, M.; Yin, Y.; Xu, L.; Guan, J. Light-Controlled Bubble Propulsion of Amorphous TiO2/Au Janus Micromotors. *RSC Adv.* **2016**, *6* (13), 10697–10703.

[53] Dong, R.; Zhang, Q.; Gao, W.; Pei, A.; Ren, B. Highly Efficient Light-Driven TiO2-Au Janus Micromotors. *ACS Nano* **2016**, *10* (1), 839–844.

[54] Ni, M.; Leung, M. K. H.; Leung, D. Y. C.; Sumathy, K. A Review and Recent Developments in Photocatalytic Water-Splitting Using TiO2 for Hydrogen Production. *Renew. Sustain. Energy Rev.* **2007**, *11* (3), 401–425.

[55] Mou, F.; Kong, L.; Chen, C.; Chen, Z.; Xu, L.; Guan, J. Light-Controlled Propulsion, Aggregation and Separation of Water-Fuelled TiO 2 /Pt Janus Submicromotors and Their “on-the-Fly” Photocatalytic Activities. *Nanoscale* **2016**, *8* (9), 4976–4983.

[56] Dong, R.; Hu, Y.; Wu, Y.; Gao, W.; Ren, B.; Wang, Q.; Cai, Y. Visible-Light-Driven BiOI-Based Janus Micromotor in Pure Water. *J. Am. Chem. Soc.* **2017**, *139* (5), 1722–1725.

[57] Lin, Z.; Si, T.; Wu, Z.; Gao, C.; Lin, X.; He, Q. Light-Activated Active Colloid Ribbons. *Angew. Chemie Int. Ed.* **2017**, *56* (43), 13517–13520.

[58] Dong, R.; Wang, C.; Wang, Q.; Pei, A.; She, X.; Zhang, Y.; Cai, Y. ZnO-Based Microrockets with Light-Enhanced Propulsion. *Nanoscale* **2017**, *9* (39), 15027–15032.

[59] Ibele, M.; Mallouk, T. E.; Sen, A. Schooling Behavior of Light-Powered Autonomous Micromotors in Water. *Angew. Chemie Int. Ed.* **2009**, *48* (18), 3308–3312.

[60] Li, J.; Singh, V. V.; Sattayasamitsathit, S.; Orozco, J.; Kaufmann, K.; Dong, R.; Gao, W.; Jurado-Sanchez, B.; Fedorak, Y.; Wang, J. Water-Driven Micromotors for Rapid Photocatalytic Degradation of Biological and Chemical Warfare Agents. ACS Nano 2014, 8 (11), 11118–11125.

[61] Esplandiu, M. J.; Afshar Farniya, A.; Bachtold, A. Silicon-Based Chemical Motors: An Efficient Pump for Triggering and Guiding Fluid Motion Using Visible Light. *ACS Nano* **2015**, *9* (11), 11234–11240.

[62] Wang, W.; Duan, W.; Ahmed, S.; Sen, A.; Mallouk, T. E. From One to Many: Dynamic Assembly and Collective Behavior of Self-Propelled Colloidal Motors. *Acc. Chem. Res.* **2015**, *48* (7), 1938–1946.

[63] Chen, H.; Zhao, Q.; Du, X. Light-Powered Micro/Nanomotors. *Micromachines* **2018**, *9* (2), 41.

[64] Elgeti, J.; Winkler, R. G.; Gompper, G. Physics of Microswimmers—single Particle Motion and Collective Behavior: A Review. *Reports Prog. Phys.* **2015**, *78* (5), 056601.

[65] Roussos, E. T.; Condeelis, J. S.; Patsialou, A. Chemotaxis in Cancer. *Nat. Rev. Cancer* **2011**, *11* (8), 573–587.

[66] Gao, W.; Pei, A.; Dong, R.; Wang, J. Catalytic Iridium-Based Janus Micromotors Powered by Ultralow Levels of Chemical Fuels. *J. Am. Chem. Soc.* **2014**, *136* (6), 2276–2279.

[67] Duan, W.; Liu, R.; Sen, A. Transition between Collective Behaviors of Micromotors in Response to Different Stimuli. *J. Am. Chem. Soc.* **2013**, *135* (4), 1280–1283.

[68] Palacci, J.; Sacanna, S.; Steinberg, A. P.; Pine, D. J.; Chaikin, P. M. Living Crystals of Light-Activated Colloidal Surfers. *Science (80-.).* **2013**, *339* (6122), 936–940.

[69] Hong, Y.; Diaz, M.; Córdova-Figueroa, U. M.; Sen, A. Light-Driven Titanium-Dioxide-Based Reversible Microfireworks and Micromotor/Micropump Systems. *Adv. Funct. Mater.* **2010**, *20* (10), 1568–1576.

[70] Ibele, M.; Mallouk, T. E.; Sen, A. Schooling Behavior of Light-Powered Autonomous Micromotors in Water. *Angew. Chemie Int. Ed.* **2009**, *48* (18), 3308–3312.

[71] Xu, T.; Gao, W.; Xu, L. P.; Zhang, X.; Wang, S. Fuel-Free Synthetic Micro-/Nanomachines. *Adv. Mater.* **2017**, *29* (9).

[72] Guix, M.; Mayorga-Martinez, C. C.; Merkoçi, A. Nano/Micromotors in (Bio)chemical Science Applications. *Chem. Rev.* **2014**, *114* (12), 6285–6322.

[73] Kim, K.; Guo, J.; Liang, Z. X.; Zhu, F. Q.; Fan, D. L. Man-Made Rotary Nanomotors: A Review of Recent Developments. *Nanoscale* **2016**, *8* (20), 10471–10490.

[74] Fan, D.; Yin, Z.; Cheong, R.; Zhu, F. Q.; Cammarata, R. C.; Chien, C. L.; Levchenko, A. Subcellular-Resolution Delivery of a Cytokine through Precisely Manipulated Nanowires. *Nat. Nanotechnol.* **2010**, *5* (7), 545–551.

[75] Kim, K.; Guo, J.; Xu, X.; Fan, D. L. Recent Progress on Man-Made Inorganic Nanomachines. *Small* **2015**, *11* (33), 4037–4057.

[76] Xu, X.; Kim, K.; Li, H.; Fan, D. L. Ordered Arrays of Raman Nanosensors for Ultrasensitive and Location Predictable Biochemical Detection. *Adv. Mater.* **2012**, *24* (40), 5457–5463.

[77] Fan, D. L.; Zhu, F. Q.; Cammarata, R. C.; Chien, C. L. Electric Tweezers. *Nano Today* **2011**, *6* (4), 339–354.

[78] Fennimore, a M.; Yuzvinsky, T. D.; Han, W.; Zettl, a. Rotational Actuators Based on Carbon Nanotubes. *Nature* **2003**, *424* (6947), 408–410.

[79] Chang, S. T.; Paunov, V. N.; Petsev, D. N.; Velev, O. D. Remotely Powered Self-Propelling Particles and Micropumps Based on Miniature Diodes. *Nat. Mater.* **2007**, *6* (3), 235–240.

[80] Sharma, R.; Velev, O. D. Remote Steering of Self-Propelling Microcircuits by Modulated Electric Field. *Adv. Funct. Mater.* **2015**, *25* (34), 5512–5519.

[81] https://en.wikipedia.org/wiki/Ultrasound

[82] Wang, J.; Gao, W. Nano/microscale Motors: Biomedical Opportunities and Challenges. *ACS Nano* **2012**, No. 7, 5745–5751.

[83] Nelson, B. J.; Kaliakatsos, I. K.; Abbott, J. J. Microrobots for Minimally Invasive Medicine. *Annu. Rev. Biomed. Eng.* **2010**, *12* (1), 55–85.

[84] Rao, K. J.; Li, F.; Meng, L.; Zheng, H.; Cai, F.; Wang, W. A Force to Be Reckoned With: A Review of Synthetic Microswimmers Powered by Ultrasound. *Small* **2015**, *11* (24), 2836–2846.

[85] Miller, D. L.; Smith, N. B.; Bailey, M. R.; Czarnota, G. J.; Hynynen, K.; Makin, I. R. S. Overview of Therapeutic Ultrasound Applications and Safety Considerations. *J. Ultrasound Med.* **2012**, *31* (4), 623–634.

[86] Lenshof, A.; Magnusson, C.; Laurell, T. Acoustofluidics 8: Applications of Acoustophoresis in Continuous Flow Microsystems. *Lab Chip* **2012**, *12* (7), 1210.

[87] Wang, W.; Castro, L. A.; Hoyos, M.; Mallouk, T. E. Autonomous Motion of Metallic Microrods Propelled by Ultrasound. *ACS Nano* **2012**, *6* (7), 6122–6132.

[88] Wang, W.; Duan, W.; Ahmed, S.; Mallouk, T. E.; Sen, A. Small Power: Autonomous Nano- and Micromotors Propelled by Self-Generated Gradients. *Nano Today* **2013**, *8* (5), 531–554.

[89] Zhang, L.; Abbott, J. J.; Dong, L.; Peyer, K. E.; Kratochvil, B. E.; Zhang, H.; Bergeles, C.; Nelson, B. J. Characterizing the Swimming Properties of Artificial Bacterial Flagella. *Nano Lett.* **2009**, *9* (10), 3663–3667.

[90] Gao, W.; Sattayasamitsathit, S.; Manesh, K. M.; Weihs, D.; Wang, J. Magnetically Powered Flexible Metal Nanowire Motors. *J. Am. Chem. Soc.* **2010**, *132* (41), 14403–14405.

[91] Burdick, J.; Laocharoensuk, R.; Wheat, P. M.; Posner, J. D.; Wang, J. Synthetic Nanomotors in Microchannel Networks: Directional Microchip Motion and Controlled Manipulation of Cargo. *J. Am. Chem. Soc.* **2008**, *130* (26), 8164–8165.

[92] Li, T.; Li, J.; Zhang, H.; Chang, X.; Song, W.; Hu, Y.; Shao, G.; Sandraz, E.; Zhang, G.; Li, L.; et al. Magnetically Propelled Fish-Like Nanoswimmers. *Small* **2016**, *12* (44), 6098–6105.

[93] Pak, O. S.; Gao, W.; Wang, J.; Lauga, E. High-Speed Propulsion of Flexible Nanowire Motors: Theory and Experiments. *Soft Matter* **2011**, *7* (18), 8169–8181.

[94] Erb, R. M.; Martin, J. J.; Soheilian, R.; Pan, C.; Barber, J. R. Actuating Soft Matter with Magnetic Torque. *Adv. Funct. Mater.* **2016**, *26* (22), 3859–3880.

[95] Tierno, P.; Golestanian, R.; Pagonabarraga, I.; Sagués, F. Controlled Swimming in Confined Fluids of Magnetically Actuated Colloidal Rotors. *Phys. Rev. Lett.* **2008**, *101* (21), 1–4.

[96] Sing, C. E.; Schmid, L.; Schneider, M. F.; Franke, T.; Alexander-Katz, a. Controlled Surface-Induced Flows from the Motion of Self-Assembled Colloidal Walkers. *Proc. Natl. Acad. Sci.* **2010**, *107* (2), 535–540.

[97] Zhang, L.; Petit, T.; Lu, Y.; Kratochvil, B. E.; Peyer, K. E.; Pei, R.; Lou, J.; Nelson, B. J. Controlled Propulsion and Cargo Transport of Rotating Nickel Nanowires near a Patterned Solid Surface. *ACS Nano* **2010**, *4* (10), 6228–6234.

[98] Gibbons, I. R. Cilia and Flagella of Eukaryotes. *J. Cell Biol.* **1981**, *91* (3), 107s – 124s.

[99] Dreyfus, R.; Baudry, J.; Roper, M. L.; Fermigier, M.; Stone, H. a; Bibette, J. Microscopic Artificial Swimmers. *Nature* **2005**, *437* (7060), 862–865.

[100] Mirkovic, T.; Foo, M. L.; Arsenault, A. C.; Fournier-Bidoz, S.; Zacharia, N. S.; Ozin, G. A. Hinged Nanorods Made Using a Chemical Approach to Flexible Nanostructures. *Nat. Nanotechnol.* **2007**, *2* (9), 565–569.

[101] Gao, W.; Sattayasamitsathit, S.; Manesh, K. M.; Weihs, D.; Wang, J. Magnetically Powered Flexible Metal Nanowire Motors. *J. Am. Chem. Soc.* **2010**, *132* (41), 14403–14405.

[102] Gao, W.; Kagan, D.; Pak, O. S.; Clawson, C.; Campuzano, S.; Chuluun-Erdene, E.; Shipton, E.; Fullerton, E. E.; Zhang, L.; Lauga, E.; et al. Cargo-Towing Fuel-Free Magnetic Nanoswimmers for Targeted Drug Delivery. *Small* **2012**, *8* (3), 460–467.

[103] BERG, H. C.; ANDERSON, R. A. Bacteria Swim by Rotating Their Flagellar Filaments. *Nature* **1973**, *245* (5425), 380–382.

[104] Qiu, F.; Nelson, B. J. Magnetic Helical Micro- and Nanorobots: Toward Their Biomedical Applications. *Engineering* **2015**, *1* (1), 021–026.

[105] Tottori, S.; Zhang, L.; Qiu, F.; Krawczyk, K. K.; Franco-Obregón, A.; Nelson, B. J. Magnetic Helical Micromachines: Fabrication, Controlled Swimming, and Cargo Transport. *Adv. Mater.* **2012**, *24* (6), 811–816.

[106] Peyer, K. E.; Tottori, S.; Qiu, F.; Zhang, L.; Nelson, B. J. Magnetic Helical Micromachines. *Chem. - A Eur. J.* **2013**, *19* (1), 28–38.

[107] Mhanna, R.; Qiu, F.; Zhang, L.; Ding, Y.; Sugihara, K.; Zenobi-Wong, M.; Nelson, B. J. Artificial Bacterial Flagella for Remote-Controlled Targeted Single-Cell Drug Delivery. *Small* **2014**, *10* (10), 1953–1957.

[108] Qiu, F.; Fujita, S.; Mhanna, R.; Zhang, L.; Simona, B. R.; Nelson, B. J. Magnetic Helical Microswimmers Functionalized with Lipoplexes for Targeted Gene Delivery. *Adv. Funct. Mater.* **2015**, *25* (11), 1666–1671.

[109] Medina-Sánchez, M.; Schwarz, L.; Meyer, A. K.; Hebenstreit, F.; Schmidt, O. G. Cellular Cargo Delivery: Toward Assisted Fertilization by Sperm-Carrying Micromotors. *Nano Lett.* **2016**, *16* (1), 555–561.

[110] Zhang, L.; Petit, T.; Peyer, K. E.; Nelson, B. J. Targeted Cargo Delivery Using a Rotating Nickel Nanowire. *Nanomedicine Nanotechnology, Biol. Med.* **2012**, *8* (7), 1074–1080.

[111] Venugopalan, P. L.; Sai, R.; Chandorkar, Y.; Basu, B.; Shivashankar, S.; Ghosh, A. Conformal Cytocompatible Ferrite Coatings Facilitate the Realization of a Nanovoyager in Human Blood. *Nano Lett.* **2014**, *14* (4), 1968–1975.

[112] Xi, W.; Solovev, A. A.; Ananth, A. N.; Gracias, D. H.; Sanchez, S.; Schmidt, O. G. Rolled-up Magnetic Microdrillers: Towards Remotely Controlled Minimally Invasive Surgery. *Nanoscale* **2013**, *5* (4), 1294–1297.

[113] Di Leonardo, R.; Ianni, F.; Ruocco, G. Colloidal Attraction Induced by a Temperature Gradient. *Langmuir* **2009**, *25* (8), 4247–4250.

[114] Wang, H.; Brandl, D. W.; Le, F.; Nordlander, P.; Halas, N. J. Nanorice: A Hybrid Plasmonic Nanostructure. *Nano Lett.* **2006**, *6* (4), 827–832.

[115] Jiang, H.-R.; Yoshinaga, N.; Sano, M. Active Motion of a Janus Particle by Self-Thermophoresis in a Defocused Laser Beam. *Phys. Rev. Lett.* **2010**, *105* (26), 268302.

[116] Xuan, M.; Wu, Z.; Shao, J.; Dai, L.; Si, T.; He, Q. Near Infrared Light-Powered Janus Mesoporous Silica Nanoparticle Motors. *J. Am. Chem. Soc.* **2016**, *138* (20), 6492–6497.

[117] Baraban, L.; Streubel, R.; Makarov, D.; Han, L.; Karnaushenko, D.; Schmidt, O. G.; Cuniberti, G. Fuel-Free Locomotion of Janus Motors: Magnetically Induced Thermophoresis. *ACS Nano* **2013**, *7* (2), 1360–1367.

[118] Martin, C. R. Membrane-Based Synthesis of Nanomaterials. *Chem. Mater.* **1996**, *8* (8), 1739–1746.

[119] Al-Mawlawi, D.; Liu, C. Z.; Moskovits, M. Nanowires Formed in Anodic Oxide Nanotemplates. *J. Mater. Res.* **1994**, *9* (04), 1014–1018.

[120] Wang, H.; Pumera, M. Fabrication of Micro/Nanoscale Motors. *Chem. Rev.* **2015**, *115* (16), 8704–8735.

[121] Mirkovic, T.; Foo, M. L.; Arsenault, A. C.; Fournier-Bidoz, S.; Zacharia, N. S.; Ozin, G. A. Hinged Nanorods Made Using a Chemical Approach to Flexible Nanostructures. *Nat. Nanotechnol.* **2007**, *2* (9), 565–569.

[122] Gao, W.; Sattayasamitsathit, S.; Orozco, J.; Wang, J. Highly Efficient Catalytic Microengines: Template Electrosynthesis of Polyaniline/Platinum Microtubes. *J. Am. Chem. Soc.* **2011**, *133* (31), 11862–11864.

[123] Sánchez, S.; Soler, L.; Katuri, J. Chemically Powered Micro- and Nanomotors. *Angew. Chemie Int. Ed.* **2015**, *54* (5), 1414–1444.

[124] Li, J.; Sattayasamitsathit, S.; Dong, R.; Gao, W.; Tam, R.; Feng, X.; Ai, S.; Wang, J. Template Electrosynthesis of Tailored-Made Helical Nanoswimmers. *Nanoscale* **2014**, *6* (16), 9415–9420.

[125] Baraban, L.; Makarov, D.; Streubel, R.; Mönch, I.; Grimm, D.; Sanchez, S.; Schmidt, O. G. Catalytic Janus Motors on Microfluidic Chip: Deterministic Motion for Targeted Cargo Delivery. *ACS Nano* **2012**, *6* (4), 3383–3389.

[126] Ghosh, A.; Fischer, P. Controlled Propulsion of Artificial Magnetic Nanostructured Propellers. *Nano Lett.* **2009**, *9* (6), 2243–2245.

[127] Walker, D.; Kübler, M.; Morozov, K. I.; Fischer, P.; Leshansky, A. M. Optimal Length of Low Reynolds Number Nanopropellers. *Nano Lett.* **2015**, *15* (7), 4412–4416.

[128] Schamel, D.; Mark, A. G.; Gibbs, J. G.; Miksch, C.; Morozov, K. I.; Leshansky, A. M.; Fischer, P. Nanopropellers and Their Actuation in Complex Viscoelastic Media. *ACS Nano* **2014**, *8* (9), 8794–8801.

[129] Mei, Y.; Solovev, A. A.; Sanchez, S.; Schmidt, O. G. Rolled-up Nanotech on Polymers: From Basic Perception to Self-Propelled Catalytic Microengines. *Chem. Soc. Rev.* **2011**, *40* (5), 2109.

[130] Mei, Y.; Huang, G.; Solovev, A. A.; Ureña, E. B.; Mönch, I.; Ding, F.; Reindl, T.; Fu, R. K. Y.; Chu, P. K.; Schmidt, O. G. Versatile Approach for Integrative and Functionalized Tubes by Strain Engineering of Nanomembranes on Polymers. *Adv. Mater.* **2008**, *20* (21), 4085–4090.

[131] Harazim, S. M.; Xi, W.; Schmidt, C. K.; Sanchez, S.; Schmidt, O. G. Fabrication and Applications of Large Arrays of Multifunctional Rolled-up SiO/SiO 2 Microtubes. *J. Mater. Chem.* **2012**, *22* (7), 2878–2884.

[132] Harazim, S. M.; Feng, P.; Sanchez, S.; Deneke, C.; Mei, Y.; Schmidt, O. G. Integrated Sensitive on-Chip Ion Field Effect Transistors Based on Wrinkled InGaAs Nanomembranes. *Nanoscale Res. Lett.* **2011**, *6* (1), 215.

[133] Solovev, A. A.; Mei, Y.; Bermúdez Ureña, E.; Huang, G.; Schmidt, O. G. Catalytic Microtubular Jet Engines Self-Propelled by Accumulated Gas Bubbles. *Small* **2009**, *5* (14), 1688–1692.

[134] Zhang, L.; Abbott, J. J.; Dong, L.; Kratochvil, B. E.; Bell, D.; Nelson, B. J. Artificial Bacterial Flagella: Fabrication and Magnetic Control. *Appl. Phys. Lett.* **2009**, *94* (6), 064107.

[135] Thiel, M.; Hermatschweiler, M. Three-Dimensional Laser Lithography. *Opt. Photonik* **2011**, *6* (4), 36–39.

[136] Tottori, S.; Zhang, L.; Qiu, F.; Krawczyk, K. K.; Franco-Obregón, A.; Nelson, B. J. Magnetic Helical Micromachines: Fabrication, Controlled Swimming, and Cargo Transport. *Adv. Mater.* **2012**, *24* (6), 811–816.

[137] Kim, S.; Qiu, F.; Kim, S.; Ghanbari, A.; Moon, C.; Zhang, L.; Nelson, B. J.; Choi, H. Fabrication and Characterization of Magnetic Microrobots for Three-Dimensional Cell Culture and Targeted Transportation. *Adv. Mater.* **2013**, *25* (41), 5863–5868.

[138] Whicker, F. W.; Hinton, T. G.; MacDonell, M. M.; Pinder, J. E., III; Habegger, L. J. Avoiding Destructive Remediation at DOE Sites. *Science* **2004***,* 303, 1615–1616.

[139]Qu, X.; Brame, J.; Li, Q.; Alvarez, P. J. J. Nanotechnology for a Safe and Sustainable Water Supply: Enabling Integrated Water Treatment and Reuse. *Acc. Chem. Res.* **2013**, *46* (3), 834–843

[140] Eskandarloo, H.; Kierulf, A.; Abbaspourrad, A. Nano- and Micromotors for Cleaning Polluted Waters: Focused Review on Pollutant Removal Mechanisms. *Nanoscale* **2017**, 13850–13863.

[141] Lundin, J. I.; Ylitalo, G. M.; Booth, R. K.; Anulacion, B.; Hempelmann, J. a.; Parsons, K. M.; Giles, D. a.; Seely, E. a.; Hanson, M. B.; Emmons, C. K.; et al. Modulation in Persistent Organic Pollutant Concentration and Profile by Prey Availability and Reproductive Status in Southern Resident Killer Whale Scat Samples. *Environ. Sci. Technol.* **2016**, *50* (12), 6506–6516.

[142] Chen, J. an; Liu, H.; Qiu, Z.; Shu, W. Analysis of Di-N-Butyl Phthalate and Other Organic Pollutants in Chongqing Women Undergoing Parturition. *Environ. Pollut.* **2008**, *156* (3), 849–853.

[143] Orozco, J.; Mercante, L. a.; Pol, R.; Merkoçi, A. Graphene-Based Janus Micromotors for the Dynamic Removal of Pollutants. *J. Mater. Chem. A* **2016**, *4* (9), 3371–3378.

[144] Vilela, D.; Parmar, J.; Zeng, Y.; Zhao, Y.; Sánchez, S. Graphene-Based Microbots for Toxic Heavy Metal Removal and Recovery from Water. *Nano Lett.* **2016**, *16* (4), 2860–2866.

[145] Neyens, E.; Baeyens, J. A Review of Classic Fenton's Peroxidation as an Advanced Oxidation Technique. *J. Hazard. Mater.* **2003**, *98* (1-3), 33–50.

[146] Orozco, J.; Cheng, G.; Vilela, D.; Sattayasamitsathit, S.; Vazquez-Duhalt, R.; Valdés-Ramírez, G.; Pak, O. S.; Escarpa, A.; Kan, C.; Wang, J. Micromotor-Based High-Yielding Fast Oxidative Detoxification of Chemical Threats. *Angew. Chemie - Int. Ed.* **2013**, *52* (50), 13276–13279.

[147] Andreozzi, R. Advanced Oxidation Processes (AOP) for Water Purification and Recovery. *Catal. Today* **1999**, *53* (1), 51–59.

[148] Brillas, E.; Sire, I.; Oturan, M. a; Sirés, I.; Oturan, M. a. Electro-Fenton Process and Related Electrochemical Technologies Based on Fenton ’s Reaction Chemistry. *Chem. Rev.* **2009**, *109* (12), 6570–6631.

[149] Soler, L.; Magdanz, V.; Fomin, V. M.; Sanchez, S.; Schmidt, O. G. Self-Propelled Micromotors for Cleaning Polluted Water. *ACS Nano* **2013**, *7* (11), 9611–9620.

[150] Parmar, J.; Vilela, D.; Pellicer, E.; Esqué-de los Ojos, D.; Sort, J.; Sánchez, S. Reusable and Long-Lasting Active Microcleaners for Heterogeneous Water Remediation. *Adv. Funct. Mater.* **2016**, *26* (23), 4152–4161.

[151] Parmar, J.; Villa, K.; Vilela, D.; Sánchez, S. Platinum-Free Cobalt Ferrite Based Micromotors for Antibiotic Removal. *Appl. Mater. Today* **2017**, *9* (23), 605–611.

[152] Qu, Y.; Duan, X. Progress, Challenge and Perspective of Heterogeneous Photocatalysts. *Chem. Soc. Rev.* **2013**, *42* (7), 2568–2580.

[153] Zhang, Z.; Zhao, A.; Wang, F.; Ren, J.; Qu, X. Design of a Plasmonic Micromotor for Enhanced Photo-Remediation of Polluted Anaerobic Stagnant Waters. *Chem. Commun.* **2016**, *52* (32), 5550–5553.

[154] Li, J.; Singh, V. V.; Sattayasamitsathit, S.; Orozco, J.; Kaufmann, K.; Dong, R.; Gao, W.; Jurado-Sanchez, B.; Fedorak, Y.; Wang, J. Water-Driven Micromotors for Rapid Photocatalytic Degradation of Biological and Chemical Warfare Agents. *ACS Nano* **2014**, *8* (11), 11118–11125.

[155] Mushtaq, F.; Guerrero, M.; Sakar, M. S.; Hoop, M.; Lindo, A. M.; Sort, J.; Chen, X.; Nelson, B. J.; Pellicer, E.; Pané, S. Magnetically Driven Bi 2 O 3 /BiOCl-Based Hybrid Microrobots for Photocatalytic Water Remediation. *J. Mater. Chem. A* **2015**, *3* (47), 23670–23676.

[156] Villa, K.; Parmar, J.; Vilela, D.; Sánchez, S. Metal-Oxide-Based Microjets for the Simultaneous Removal of Organic Pollutants and Heavy Metals. *ACS Appl. Mater. Interfaces* **2018**, *10* (24), 20478–20486.

[157] Abdelmohsen, L. K. E. A.; Peng, F.; Tu, Y.; Wilson, D. A. Micro- and Nano-Motors for Biomedical Applications. *J. Mater. Chem. B* **2014**, *2* (17), 2395–2408.

[158] Li, J.; Esteban-Fernández de Ávila, B.; Gao, W.; Zhang, L.; Wang, J. Micro/nanorobots for Biomedicine: Delivery, Surgery, Sensing, and Detoxification. *Sci. Robot.* **2017**, *2* (4), eaam6431.

[159] Campuzano, S.; Orozco, J.; Kagan, D.; Guix, M.; Gao, W.; Sattayasamitsathit, S.; Claussen, J. C.; Merkoçi, A.; Wang, J. Bacterial Isolation by Lectin-Modified Microengines. *Nano Lett.* **2012**, *12* (1), 396–401.

[160] Patra, D.; Sengupta, S.; Duan, W.; Zhang, H.; Pavlick, R.; Sen, A. Intelligent, Self-Powered, Drug Delivery Systems. *Nanoscale* **2013**, *5* (4), 1273–1283.

[161] Kagan, D.; Laocharoensuk, R.; Zimmerman, M.; Clawson, C.; Balasubramanian, S.; Kang, D.; Bishop, D.; Sattayasamitsathit, S.; Zhang, L.; Wang, J. Rapid Delivery of Drug Carriers Propelled and Navigated by Catalytic Nanoshuttles. *Small* **2010**, *6* (23), 2741–2747.

[162] Sundararajan, S.; Lammert, P. E.; Zudans, A. W.; Crespi, V. H.; Sen, A. Catalytic Motors for Transport of Colloidal Cargo. *Nano Lett.* **2008**, *8* (5), 1271–1276.

[163] Kagan, D.; Laocharoensuk, R.; Zimmerman, M.; Clawson, C.; Balasubramanian, S.; Kang, D.; Bishop, D.; Sattayasamitsathit, S.; Zhang, L.; Wang, J. Rapid Delivery of Drug Carriers Propelled and Navigated by Catalytic Nanoshuttles. *Small* **2010**, *6* (23), 2741–2747.

[164] Solovev, A. A.; Sanchez, S.; Pumera, M.; Mei, Y. F.; Schmidt, O. G. Magnetic Control of Tubular Catalytic Microbots for the Transport, Assembly, and Delivery of Micro-Objects. *Adv. Funct. Mater.* **2010**, *20* (15), 2430–2435.

[165] Baylis, J. R.; Chan, K. Y. T.; Kastrup, C. J. Halting Hemorrhage with Self-Propelling Particles and Local Drug Delivery. *Thromb. Res.* **2016**, *141* (15), S36–S39.

[166] Hortelão, A. C.; Patiño, T.; Perez-Jiménez, A.; Blanco, À.; Sánchez, S. Enzyme-Powered Nanobots Enhance Anticancer Drug Delivery. *Adv. Funct. Mater.* **2018**, *28* (25), 1705086.

[167] Esteban-Fernández de Ávila, B.; Angell, C.; Soto, F.; Lopez-Ramirez, M. A.; Báez, D. F.; Xie, S.; Wang, J.; Chen, Y. Acoustically Propelled Nanomotors for Intracellular siRNA Delivery. *ACS Nano* **2016**, *10* (5), 4997–5005.

[168] Wu, Y.; Lin, X.; Wu, Z.; Möhwald, H.; He, Q. Self-Propelled Polymer Multilayer Janus Capsules for Effective Drug Delivery and Light-Triggered Release. *ACS Appl. Mater. Interfaces* **2014**, *6* (13), 10476–10481.

[169] Maria-Hormigos, R.; Jurado-Sánchez, B.; Escarpa, A. Labs-on-a-Chip Meet Self-Propelled Micromotors. *Lab Chip* **2016**, *16* (13), 2397–2407.

[170] García, M.; Orozco, J.; Guix, M.; Gao, W.; Sattayasamitsathit, S.; Escarpa, A.; Merkoçi, A.; Wang, J. Micromotor-Based Lab-on-Chip Immunoassays. *Nanoscale* **2013**, *5* (4), 1325–1331.

[171] Solovev, A. A.; Xi, W.; Gracias, D. H.; Harazim, S. M.; Deneke, C.; Sanchez, S.; Schmidt, O. G. Self-Propelled Nanotools. *ACS Nano* **2012**, *6* (2), 1751–1756.

[172] Xi, W.; Solovev, A. A.; Ananth, A. N.; Gracias, D. H.; Sanchez, S.; Schmidt, O. G. Rolled-up Magnetic Microdrillers: Towards Remotely Controlled Minimally Invasive Surgery. *Nanoscale* **2013**, *5* (4), 1294–1297.

[173] Kagan, D.; Benchimol, M. J.; Claussen, J. C.; Chuluun-Erdene, E.; Esener, S.; Wang, J. Acoustic Droplet Vaporization and Propulsion of Perfluorocarbon-Loaded Microbullets for Targeted Tissue Penetration and Deformation. *Angew. Chemie Int. Ed.* **2012**, *51* (30), 7519–7522.

[174] Martel, S.; Mohammadi, M.; Felfoul, O.; Zhao Lu; Pouponneau, P. Flagellated Magnetotactic Bacteria as Controlled MRI-Trackable Propulsion and Steering Systems for Medical Nanorobots Operating in the Human Microvasculature. *Int. J. Rob. Res.* **2009**, *28* (4), 571–582.

[175] Olson, E. S.; Orozco, J.; Wu, Z.; Malone, C. D.; Yi, B.; Gao, W.; Eghtedari, M.; Wang, J.; Mattrey, R. F. Toward in Vivo Detection of Hydrogen Peroxide with Ultrasound Molecular Imaging. *Biomaterials* **2013**, *34* (35), 8918–8924.

[176] de Ávila, B. E.-F.; Angsantikul, P.; Li, J.; Angel Lopez-Ramirez, M.; Ramírez-Herrera, D. E.; Thamphiwatana, S.; Chen, C.; Delezuk, J.; Samakapiruk, R.; Ramez, V.; et al. Micromotor-Enabled Active Drug Delivery for in Vivo Treatment of Stomach Infection. *Nat. Commun.* **2017**, *8* (1), 272.

[177] Esplandiu, M. J.; Afshar Farniya, A.; Bachtold, A. Silicon-Based Chemical Motors: An Efficient Pump for Triggering and Guiding Fluid Motion Using Visible Light. *ACS Nano* **2015**, *9* (11), 11234–11240.

[178] Brönstrup, G.; Jahr, N.; Leiterer, C.; Csáki, A.; Fritzsche, W.; Christiansen, S. Optical Properties of Individual Silicon Nanowires for Photonic Devices. *ACS Nano* **2010**, *4* (12), 7113–7122.

[179] Xu, T.; Lambert, Y.; Krzeminski, C.; Grandidier, B.; Stiévenard, D.; Lévêque, G.; Akjouj, A.; Pennec, Y.; Djafari-Rouhani, B. Optical Absorption of Silicon Nanowires. *J. Appl. Phys.* **2012**, *112* (3), 033506.

[180] Neyens, E.; Baeyens, J. A Review of Classic Fenton's Peroxidation as an Advanced Oxidation Technique. *J. Hazard. Mater.* **2003**, *98* (1-3), 33–50.

[181] Esplandiu, M.J.; Afshar Farniya, A.; Bachtold, A. Silicon-based chemical motors: an efficient pump for triggering and guiding fluid motion using visible light. *ACS Nano* **2015**, 9, 11234–11240.

[182] Afshar-Farniya, A.; Esplandiu, M.J.; Reguera, D.; Bachtold, A. Imaging proton concentration and mapping the spatial distribution of the electric field of catalytic micropumps. *Phys. Rev. Lett*. **2013**, 111, 168301.

[183] Brown, A.; Poon, W. Ionic Effects in Self-Propelled Pt-Coated Janus Swimmers, *Soft Matter*. **2014**, 10, 4016-4027.

[184] Ebbens, S.; Gregory, D.A.; Dunderdale, G.; Howse, J.R.; Ibrahim Y.; Liverpool, T.B.; Golestanian, R. Electrokinetic Effects in Catalytic Pt-Insulator Janus Swimmers, *Europhys. Lett*. **2014**, 106, 58003.

[185] Brown, A.T.; Poon, W.C.K.; Holm, C.; de Graaf, J. Ionic screening and dissociation are crucial for understanding chemical self-propulsion in polar solvents. *Soft Matter* **2017**, 13, 1200-1222.

[186] Macias-Montero, M.; Lopez-Santos, C.; Filippin, a. N.; Rico, V. J.; Espinos, J. P.; Fraxedas, J.; Perez-Dieste, V.; Escudero, C.; Gonzalez-Elipe, A. R.; Borras, A. In Situ Determination of the Water Condensation Mechanisms on Superhydrophobic and Superhydrophilic Titanium Dioxide Nanotubes. *Langmuir* **2017**, *33* (26), 6449–6456.

[187] Kim, K. S.; Winograd, N.; Davis, R. E. Electron Spectroscopy of Platinum-Oxygen Surfaces and Application to Electrochemical Studies. *J. Am. Chem. Soc.* **1971**, *93* (23), 6296–6297.

[188] Vargas-Estevez, C.; Duch, M.; Duque, M.; del Campo, F. J.; Enriquez-Barreto, L.; Murillo, G.; Torras, N.; Plaza, J. A.; Saura, C. A.; Esteve, J. Microphotodiodes: Suspended Silicon Microphotodiodes for Electrochemical and Biological Applications. *Small* **2017**, *13* (41).

[189] Petrucci, Harwood, Herring, and Madura. General Chemistry: Principles and Modern Applications. 9th ed. *Pearson Education* **2007**.

[190] Fu, F.; Dionysiou, D. D.; Liu, H. The Use of Zero-Valent Iron for Groundwater Remediation and Wastewater Treatment: A Review. *J. Hazard. Mater.* **2014**, *267* (7), 194–205.

[191] Jang, M.-H.; Lim, M.; Hwang, Y. S. Potential Environmental Implications of Nanoscale Zero-Valent Iron Particles for Environmental Remediation. *Environ. Health Toxicol.* **2014**, *29* (12), e2014022.

[192] Pourrezaei, P.; Alpatova, A.; Khosravi, K.; Drzewicz, P.; Chen, Y.; Chelme-Ayala, P.; Gamal El-Din, M. Removal of Organic Compounds and Trace Metals from Oil Sands Process-Affected Water Using Zero Valent Iron Enhanced by Petroleum Coke. *J. Environ. Manage.* **2014**, *139* (12), 50–58.

[193] SCRIVEN, L. E.; STERNLING, C. V. The Marangoni Effects. *Nature* **1960**, *187* (4733), 186–188.

[194] Dimova-Malinovska, D.; Sendova-Vassileva, M.; Tzenov, N.; Kamenova, M. Preparation of Thin Porous Silicon Layers by Stain Etching. *Thin Solid Films* **1997**, *297* (1-2), 9–12.

[195] Lin, H.; Cheung, H.-Y.; Xiu, F.; Wang, F.; Yip, S.; Han, N.; Hung, T.; Zhou, J.; Ho, J. C.; Wong, C.-Y. Developing Controllable Anisotropic Wet Etching to Achieve Silicon Nanorods, Nanopencils and Nanocones for Efficient Photon Trapping. *J. Mater. Chem. A* **2013**, *1* (34), 9942.

[196] http://www.bitplane.com/imaris/imaris

[197] http://www.diatrack.org/index.html

[198] Douglas A. Skoog, Donald M. West, F. James Holler, Stanley R. Crouch, Fundamentals of Analytical Chemistry 9th Edition, Jan 2013, Cengage Learning

[199] Dieter K. Schroder, Semiconductor Material and Device Characterization, 3rd Edition, Jun 2015, Wiley-IEEE Press

[200] Salmeron, M.; Schlögl, R. Ambient Pressure Photoelectron Spectroscopy: A New Tool for Surface Science and Nanotechnology. *Surf. Sci. Rep.* **2008**, 63 (4), 169–199.

[201] Pérez-Dieste, V.; Aballe, L.; Ferrer, S.; Nicolàs, J.; Escudero, C.; Milán, a.; Pellegrin, E. Near Ambient Pressure XPS at ALBA. *J. Phys. Conf. Ser.* **2013**, *425*.